DETERMINING THE EFFECTS OF TRANSFORMATION INDUCED PLASTICITY AND CREEP PLASTICITY ON THE FUNCTIONAL FATIGUE LIFE OF NiTiHf HIGH TEMPERATURE SHAPE MEMORY ALLOYS

NiTiHf YÜKSEK SICAKLIK ŞEKIL HAFIZALI ALAŞIMLARINDA FAZ DÖNÜŞÜMÜ ILE TETIKLENEN PLASTIK DEFORMASYON VE SÜRÜNME PLASTIK DEFORMASYONUN FONKSIYONEL YORULMA ÖMRÜNE ETKISININ BELIRLENMESI

HALİL ONAT TUĞRUL

PROF. DR. BENAT KOÇKAR
Supervisor

Submitted to
Graduate School of Science and Engineering of Hacettepe University
as a Partial Fulfillment to the Requirements
for the Award of the Degree of Doctor of Philosophy
in Mechanical Engineering

2023

To My Family

Especially to my sister Selen

ABSTRACT

DETERMINING THE EFFECTS OF TRANSFORMATION INDUCED PLASTICITY AND CREEP PLASTICITY ON THE FUNCTIONAL FATIGUE LIFE OF NiTiHf HIGH TEMPERATURE SHAPE MEMORY ALLOYS

Halil Onat TUĞRUL

Doctor of Philosophy, Department of Mechanical Engineering

Supervisor: Prof. Dr. Benat KOÇKAR

January 2023, 104 pages

With their high work output during thermal cycling under load, NiTiHf high temperature shape memory alloys became promising candidates for smart actuator design for aerospace industry. However, high temperature applications under loading are susceptible to creep deformation. It has been already shown that functional properties of high temperature shape memory alloys degrade faster since they work at high temperatures. For instance, their actuation abilities decrease and transformation temperatures shift due to the dislocation formation via plastic deformation with martensite-austenite phase transformation. In this work creep deformation behavior of 50at%Ni – 25 at% Ti – 25 at% Hf high temperature shape memory alloy was studied at 450°C, 500°C, 550°C and 600°C temperatures under 200 MPa, 300 MPa, 400 MPa and 500 MPa loading conditions. Creep model parameters were found and creep behavior was discussed in comparison with creep results in the literature on NiTi alloys. Creep deformation rates were also compared with the deformation rates that were acquired from functional fatigue experimental results. Functional fatigue experiments yielded 40 times higher deformation rate than that was obtained from creep experiments for the same loading condition. It is important to mention that upper cycle temperature which the samples were heated during functional fatigue experiment and creep test temperature was same. Additionally, functional fatigue cycles with subsequent creep experiments were run consecutively in order to determine the effect of the deformation of one on the other. Creep deformation was found to have little to no effect on functional fatigue cycles, on the other hand functional fatigue cycles led to an increase in dislocation density that changes creep behavior of the material.

Keywords: NiTiHf, HIGH TEMPERATURE SHAPE MEMORY ALLOYS, TRIP, CREEP, PLASTIC DEFORMATION, FUNCTIONAL FATIGUE TESTS

ÖZET

NiTiHf YÜKSEK SICAKLIK ŞEKIL HAFIZALI ALAŞIMLARINDA FAZ DÖNÜŞÜMÜ ILE TETIKLENEN PLASTIK DEFORMASYON VE SÜRÜNME PLASTIK DEFORMASYONUN FONKSIYONEL YORULMA ÖMRÜNE ETKISININ BELIRLENMESI

Halil Onat TUĞRUL

Doktora, Makine Mühendisliği Bölümü

Tez Danışmanı: Prof. Dr. Benat KOÇKAR

Ocak 2023, 104 sayfa

Isıl çevrim sırasında yüksek iş üretebilme kabiliyetleri ile NiTiHf yüksek sıcaklık şekil hafızalı alaşımları, uçak ve uzay endüstrisinde geliştirilecek akıllı eyleyiciler için umut vaad eden alaşımlar olarak görülmektedir. Ancak yüksek sıcaklıkta yük altında yapılan uygulamalarda sürünme hasarı oluşması mümkündür. Şimdiye kadar yüksek sıcaklık şekil hafızalı alaşımlarında yapılan çalışmalar daha yüksek ısıl çevrim sıcaklıklarına çıkılması durumunda fonksiyonel yorulma sırasında oluşan hasarın arttığı göstermiştir. Hasara örnek olarak martenzit östenit dönüşümü sonucu dislokasyon oluşumu ve plastik deformasyon ile eyleme gerinmeleri azalması ve dönüşüm sıcaklıklarının kayması verilebilir. Bu tezde 50at%Ni – 25 at% Ti – 25 at% Hf alaşımının sürünme davranışı 450°C, 500°C, 550°C ve 600°C sıcaklıklarında 200 MPa, 300 MPa, 400 MPa ve 500 MPa gerilme değerleri için çalışılmıştır. Sürünme modeli parametreleri belirlenmiş ve literatürdeki NiTi ikili alaşımlarında yapılan çalışmalarla kıyaslanmıştır. Fonksiyonel yorulma deneyleri yapılarak, sürünme sırasında görülen gerinme hızları ile fonksiyonel yorulma deneyleri sırasında oluşan gerinme hızı kıyaslanmıştır. Fonksiyonel yorulma deneylerinde çıkılan en yüksek sıcaklık yani üst çevrim sıcaklığı sürünme deneylerinin de gerçekleştirildiği sıcaklıktır. Fonksiyonel yorulma deneylerinde aynı yük altındaki sürünme deneylerine göre 40 kat daha hızlı hasar oluştuğu gözlemlenmiştir. Bunlara ek olarak, sürünme deneyleri ile fonksiyonel yorulma deneyleri birleştirilmiş ve hasar yapılarının deney sonuçlarına etkisi araştırılmıştır. Sürünme hasarının fonksiyonel yorulma davranışına etkisi saptanamamıştır ancak fonksiyonel yorulma sırasında oluşan dislokasyon yoğunluğundaki artışın sürünme deneyi sırasında oluşan gerinme yapısını değiştirdiği görülmüştür.

Anahtar Kelimeler: NiTiHf, YÜKSEK SICAKLIK ŞEKIL HAFIZALI ALAŞIMLAR, TRIP, SÜRÜNME, PLASTİK DEFORMASYON, FONKSİYONEL YORULMA TESTLERİ

ACKNOWLEDGMENTS

I want to thank my thesis supervisor Prof. Dr. Benat KOÇKAR for her support and guidance in this seven and a half years journey. We have accomplished several scientific and industrial projects and attended conferences around the world thanks to her leadership and vision.

This study was funded by Air Force Office of Scientific Research (AFOSR) Grant No: FA9550-20-1-0261. I also want to thank Prof. Dr. Ali SAYIR, our program manager in AFOSR, for his valuable comments on the article we have published from this study.

I am grateful that Prof. Dr. Ziya ESEN and Assist. Prof. Dr. Okan GÖRTAN have accepted to join my thesis monitoring committee. This work have matured with their comments and questions along the way.

I want to thank Prof. Dr. Bora MAVİŞ and Prof. Dr. Y. Eren KALAY for their comments and questions in the thesis defense. Their participation gave insight on the further investigations.

Assoc. Prof. Z. Göknur BÜKE and her Ph.D. student Ömer CAYLAN helped us a lot especially with TEM and SEM studies especially during the Covid restrictions. They have my gratitude for their support.

I have started Ph.D. studies with Dr. Erhan AKIN and a year later Dr. Meriç EKİCİLER joined us. We have learned and discussed the results together. I am grateful for their presence and support. Also I want to thank Hasan H. SAYGILI and Oğulcan AKGÜL who both were working with me full time and witnessing every part of the struggle.

I want to thank my friends; Bünyamin ÇÖMLEKÇİ, Elif ÇAKICI, Mert ERDOĞAN, Eda KOÇAK, Doğan GENÇ, Ü. Ufuk AYDIN, Şerife BÜRÜNGÜZ, Bayram KARAKULLUKÇU and Çiğdem AVCI. They were the anchor to me, keeping my life in balance in every step of the way.

My dearest sister Selen TUĞRUL was the constant in my life in this ever changing world. With her support, I was able to overcome my wrongful perceptions. This was a team work that cannot be done otherwise.

TABLE OF CONTENT

LIST OF FIGURES

LIST OF TABLES

SYMBOLS AND ABBREVIATIONS

Symbols

A - A0	Material Constant
ε	True Strain (mm/mm)
$\dot{\varepsilon}$	Strain Rate (s^{-1})
σ	Stress (MPa)
Na - n	Stress Exponent
k	Boltzmann Constant
Q	Activation Energy (kJ/mol)
Q_{sd}	Activation Energy of Self Diffusion (kJ/mol)
R	Ideal Gas Constant
T	Temperature (°K)

Abbreviations

A_f	Austenite Finish Temperature
A_s	Austenite Start Temperature
EDS	Energy Dispersive X-Ray Spectroscopy
HTSMA	High Temperature Shape Memory Alloy
LCT	Lower Cycle Temperature
M_f	Martensite Finish Temperature
M_s	Martensite Start Temperature
PLB	Power Law Breakdown
RMSE	Root Mean Square Error
SEM	Scanning Electron Microscopy

SMA	Shape Memory Alloy
TTs	Transformation Temperatures
TWSME	Two Way Shape Memory Effect
UCT	Upper Cycle Temperature

1. INTRODUCTION

In the last three decades, high temperature shape memory alloys (HTSMAs) have received attention with an increasing demand from aerospace industry. Light-weight actuators that can operate above 100°C was the main driving force for developing new HTSMAs [1,2]. In order to produce new HTSMAs, adding tertiary element to NiTi binary shape memory alloy (SMA) has been one of the primary approaches. It has been revealed that gold (Au), palladium (Pd), platinum (Pt), Zirconium (Zr) and Hafnium (Hf) elements have been increasing the Transformation Temperatures (TTs) when added to NiTi as tertiary alloying elements [2]. However, due to cost concerns researchers have focused to zirconium (Zr) and hafnium (Hf) in order to increase the TTs [3]. Recently, it has been presented that Ni-rich NiTiHf alloys attain higher work-output with strengthening through precipitation hardening [3]. It has been also shown that NiTiHf alloys are much easier to train for two-way shape memory effect (TWSME) than that of NiTiZr alloys since NiTiHf alloys required relatively lower stresses for reorientation of the martensite variants [4].

Ni rich NiTiHf alloys have been focused due to their ability of hardening via precipitation heat treatment which also enables tailorable transformation temperatures [2,5,6]. 50.3at% Ni-29.7at% Ti - 20at.% Hf alloys have showed high thermal and dimensional stability, in addition to their increased strength and functional fatigue life up to 20000 cycles with precipitation hardening [7–10]. In the literature, functional fatigue is defined as the loss of actuation properties of SMAs during heating-cooling thermal cycles especially under stress. It has been reported by Karakoc et. al., when upper limit temperature of the heating cycle is increased, functional fatigue life of the alloys decreases. In the literature, the temperature, which is determined to attain complete martensite to austenite transformation, has been named as Upper Cycle Temperature (UCT) in functional fatigue experimentation [9]. It was reported that with lower UCT values, actuation strain tends to decrease with thermal cycling and higher UCT values lead to observe increased actuation strains [8,9]. It was claimed that annihilation of dislocations were the primary cause for increased actuation strain and irrecoverable strain together that cause a decrease in fatigue life at temperatures above 300°C [9]. Increase in irrecoverable strain throughout functional fatigue experimentation with higher UCT values could be due to plastic deformation via dislocation formation and/or creep viscoplasticity. However, it is difficult to differentiate plastic deformation due to dislocation formation and creep viscoplasticity since both conditions present itself as irrecoverable strain during functional fatigue experiments.

Kumar et al. presented that slower heating cooling rate increases irrecoverable strain in TiPdNi HTSMA alloys [11]. Later same group in collaboration with NASA researchers, conducted experiments on 50.5at%Ti 30at%Pd 19.5at% Ni alloy in order to reveal both creep model parameters and irrecoverable strain formation during thermal cycling for the loading conditions that were used in creep experiments [12]. 50.5at%Ti 30at%Pd 19.5at% Ni alloy showed diffusional creep when the sample was tested under 100 MPa to 300 MPa loading conditions and dislocation climb creep between 300 to 500 MPa loading conditions. Thermal cycling results also revealed increasing irrecoverable strain formation in correlation with creep behavior and proved that creep deformation has substantial effect on functional fatigue properties of the alloy [12]. Thus, it has become imperative to study the creep behavior of HTSMAs and to differentiate creep plasticity from transformation induced plasticity and then to overcome creep viscoplasticity for sustaining a long fatigue life.

For the desired outcome, in this thesis functional fatigue experiments were performed in order to determine damage accumulation with the irrecoverable strain formation. For comparison, creep behavior of 50at%Ni 25at%Ti 25 at%Hf alloy was displayed using constant load experiments at near UCT temperatures where creep deformation was expected. Creep behavior of the alloy was resolved using Power Law Equation [12,13]:

$$\dot{\varepsilon} = A\,\sigma^{Na}\,e^{-Q/RT}$$

Both creep experiments and functional fatigue experiments were performed on annealed and grain growth heat treated samples for investigating the effect of grain size.

In addition, functional fatigue cycles with subsequent creep experiment was performed consecutively to reveal the effect of functional fatigue cycles on the creep behavior and the effect of creep experiments on the functional fatigue cycling behavior.

2. LITERATURE

2.1. Martensitic Transformation and Shape Memory Alloys

2.1.1. Martensitic Transformation

Martensitic transformation is a diffusionless phase transformation with the displacement of atoms via shear mechanism, which occurs when austenite (parent) phase is cooled down to a specific martensite start temperature (M_s) [14]. Martensitic transformation is reversible, when martensite structure is thermoelastic and the internal friction is small between the martensite phase and the parent phase boundary. Thermoelastic term explains that martensite phase can store high amounts of elastic energy so that slip does not occur during transformation and this energy is spent to overcome the friction for the transformation of the martensite phase to parent phase. On the other hand, martensitic transformation takes place with slip formation in non-thermoelastic martesite and reverse transformation can not be activated without nucleation of parent phase, which requires large over heating [15,16].

Free energy for martensite formation formulated as follows:

$\Delta G_{\beta\alpha} = \Delta G_c + \Delta G_{nc} = \Delta G_c + \Delta G_e + \Delta G_f$

In this equation free energy difference for austenite to martensite phase transformation $\Delta G_{\beta\alpha}$ (β indicates austenite phase and α indicates martensite phase) equals to summation of the chemical free energy term (ΔG_c) and the non-chemical free energy term (ΔG_{nc}). The chemical free energy term (ΔG_c) is the free energy of nucleation of martensite (ΔG_n). The non-chemical free energy terms (ΔG_{nc}) are the free energy of elastic deformation (ΔG_e) and the free energy due to the friction (ΔG_f) between martensite and austenite. Above equation explains that in order to start the nucleation of martensite, a certain overcooling which is generally represented by ΔT, is required due to the presence of non-chemical free energy terms. For reverse transformation, non-thermoelastic martensites require overheating in order to overcome free energy of nucleation (ΔG_n), free energy of elastic deformation (ΔG_e) and free energy of friction (ΔG_f). However, if the martensite is thermoelastic, elastic energy is stored by martensite and austenite does not require nucleation. Martensite to austenite reverse transformation begins with the retreat of martensite. As a result, only ΔG_f must be overcome by overheating for reverse transformation [15]. Thermodynamic equation for reverse transformation of thermoelastic martensite can be written as following:

$\Delta G_{\alpha\beta} = -\Delta G_e^r + \Delta G_f^r$

Martensitic transformation is plotted by representing the terms of free energy vs temperature in Figure 2.1, where T_o is the equilibrium temperature at which two phases have the same free energy to form. When martensitic transformation is reversible with the $-\Delta G_e^r$ term, T_o for reverse transformation changes to T_o^r position.

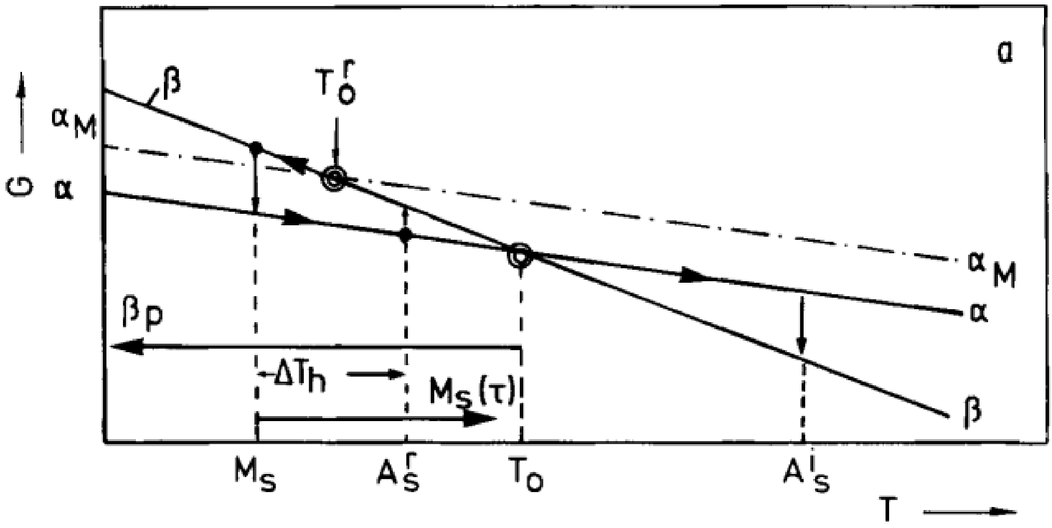

Figure 2.1. Forward and reverse martensitic transformation free energy vs temperature plot [15].

In the Figure 2.1, M_s, A_s^i and A_s^r are the martensite start temperature, the irreversible austenite start temperature and the reversible austenite start temperature, respectively. $M_s(\tau)$ term shows the increase in martensite start temperature under shear stress which will be explained in next section in Figure 2.5. It can be deduced from the change in equilibrium temperature that temperature difference between M_s and A_s^r is smaller than the difference between M_s and A_s^i. Hence the difference between overheating and overcooling (ΔT_h) which is the thermal hysteresis, become smaller for reversible martensitic transformations. Hysteresis values for complete forward and reverse martensite transformations of thermoelastic and non-thermoelastic martensites are presented in Figure 2.2.

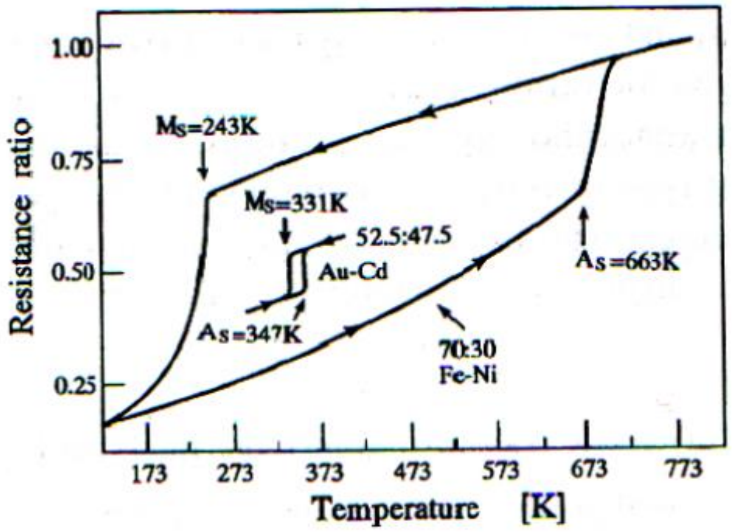

Figure 2.2. Hysteresis of thermoelastic (Au-Cd) and non-thermoelastic martensite (Fe-Ni) in electrical resistivity vs temperature plot [17,18].

Additionally, bulk shape change of the material under shear stresses during martensitic transformation must be accommodated. Accommodation of the shape change can be achieved with slip or twining of martensite structure. In Figure 2.3 it was schematically explained how material can compensate the shape change below martensite finish (M_f) temperatures.

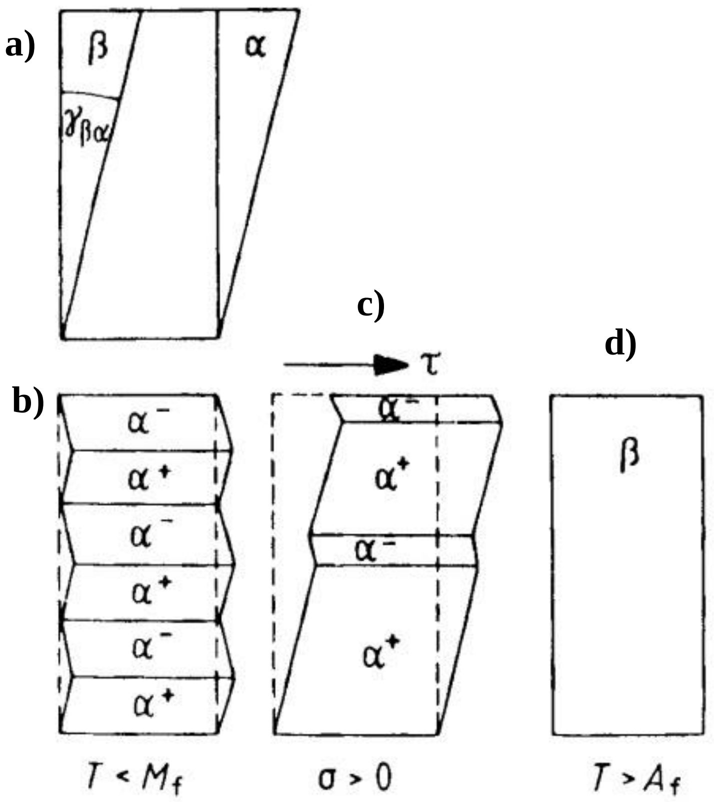

Figure 2.3. Schematics on accommodation of shape change [15] ; a) accommodation with slip, b) accommodation with twinning, c) detwinning in the presence of stress d) austenite formation via heating above austenite finish temperature (A_f)

The unique abilities of shape memory alloys' arose from thermoelastic nature of martesitic transformation and twinning deformation mode which enables reversibility to the austenite phase.

2.1.2. Shape Memory Alloys

Shape memory alloys are known as smart materials due to their capacity to recover their original shape upon austenitic phase transformation, if the material is deformed and subjected to shape change while it is in martensitic phase [19]. Recovering the former shape with martensite to austenite phase transformation via heating is called Shape Memory Effect (SME) and it is demonstrated in Figure 2.4 along with electrical resistivity change due to change in crystal structure. It was also discovered that loading to certain stress level causes stress induced martensite (SIM) formation in austenite if the temperature is kept above martensite finish temperature (M_f). Martensite phase transform back to austenite phase upon unloading. This phenomenon is called Pseudoelasticity or Superelasticity as it will be used in this thesis [20].

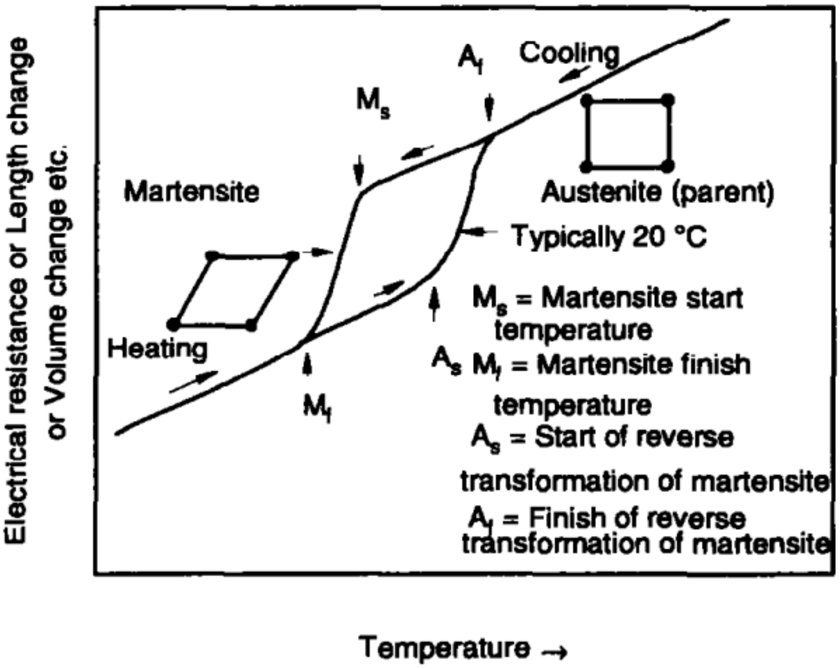

Figure 2.4. Phase transformation schematic of shape memory alloys [19].

In order to achieve superelasticity, martensite should not be stable and austenite phase should exist. However, there is a stress limitation to superelastic behavior. Thermomechanical limits to observe both shape memory effect and superelasticity can be drawn by considering the applied stress with respect to temperature at which the alloy is kept as shown in Figure 2.5. It should be noticed from Figure 2.5, the critical stress to induce martensite line have a positive slope. It means that critical stress to induce martensite increases as the temperature increases [21]. This phenomenon can be explained by thermodynamical approach as presented in Figure 2.1, where $M_s(\tau)$ increases with shear stress. Stress limitation to observe both shape memory effect and superelasticity is called as critical stress for slip (A) and it decreases with increasing temperature, as can be seen in the Figure 2.5. Otsuka and Shimizu have also defined a low critical stress for slip (B) since alloys other than NiTi showed low critical stress for slip and yield before substantial stress induced martensite forms [21].

Shape memory effect region, in Figure 2.5, is limited with A_f temperature and critical stress to induce martensite. A_f temperature is creating a limit because the shape memory effect is utilized with deformation of martensite which is still possible between A_s and A_f temperatures. Above A_f temperature, martensite is fully transformed into austenite and austenite is the stable phase above this temperature. Critical stress to induce martensite also creates a boundary for shape memory effect since the material that has austenite phase between M_s and A_s temperatures (heated up to A_f then cooled down below A_s) has to transform into martensite via loading.

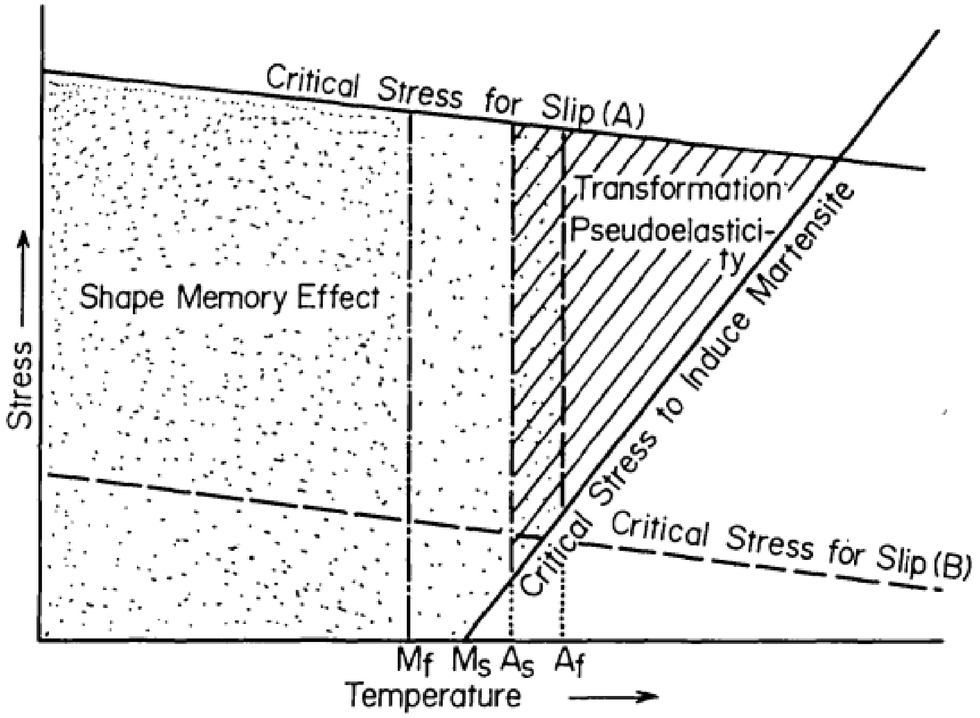

Figure 2.5. Thermomechanical conditions considering the applied stress and the temperature for shape memory effect and superelasticity [21].

However, forward and reverse martensitic transformation of shape memory alloys does not take place without damage formation. Residual dislocations and internal stress formations are already known as the substructures and features which are necessary to achieve two-way shape memory effect (TWSME). SME was explained as recovering shape change upon reverse martensitic transformation, if martensite twin structure was detwinned with external stress. SME phenomenon is defined as “one way” since recovery needs a deformation in the martensite phase after heating the SMA to obtain austenite and no shape change is observed after cooling the alloy back to martensite. However, if dislocation arrays and internal stress fields are created by applying some thermomechanical training procedures (such as deforming martensite, heating to austenite for shape recovery, cooling to martensite, redeforming the martensite and applying this procedure for many cycles) and/or deformation processes (such as rolling, extrusion, equal channel angular extrusion etc.) it is possible to observe Two-Way Shape Memory Effect (TWSME). TWSME is the effect which the original shape can be recovered via heating the alloy to austenite and deformed shape can be observed via cooling the alloy back to martensite, so both the high temperature and low temperature shapes are able to be remembered by the alloy. Retained martensite and internal stress fields due to dislocations enable the occurrence of TWSME without external deformation while the alloy is in martensite phase [22,23]. TWSME diminishes with cycling at high temperatures and annealing since high temperature leads to annihilate dislocations and relieve internal stresses [22]. In the next section damage formation during SME will be explained.

2.1.3. Damage Formation During Shape Memory Effect

Damage formation during martensitic transformation is a challenge which has to be overcome for the industrial use of shape memory actuators. It has been studied extensively with the utilization of functional fatigue experiments using different alloy systems throughout the years of shape memory alloy research [7–10,24–27]. In the last two decades, advances in information sciences and increase in computational capacity enabled researchers to focus on modeling of shape memory functional behavior [28–34].

Early studies showed that actuation strain magnitude was inversely correlated with fatigue life. NiTi alloys' functional fatigue life was found to be on the order of 10^5 cycles if the actuation strain was 0.1% [24]. Although it seems like the fatigue life is high enough the strain value can be considered as very low for many actuator applications. Microstructural evolution appears to be the dominant factor in strain formation during incomplete reverse transformation. In fact, irrecoverable strain occurs in every cycle where there is no complete transformation [25]. Martensite formation creates dislocations between martensite and austenite phase boundaries due to the incompatibility between the crystal structures of the phases. TEM studies revealed that austenite phase near martensite phase boundary contain residual martensite and localized slip formation [26]. Dislocation formation and accumulation at the phase boundaries with cycles are found to be the main deformation mode during shape memory effect.

Slip and retained martensite formation during thermomechanical cycling are identified as the main mechanisms behind the degradation of functional properties. Hence, increasing critical stress for slip (CSS) would result better functional fatigue properties. Sehitoglu et al. worked on NiTiHf alloys with the prospect of higher CSS of NiTiHf which makes it much suitable for high temperature actuator applications [27]. Figure 2.6 was taken from the same work which explains how elastic energy dissipation via dislocation formation increases hysteresis during thermomechanical cycles.

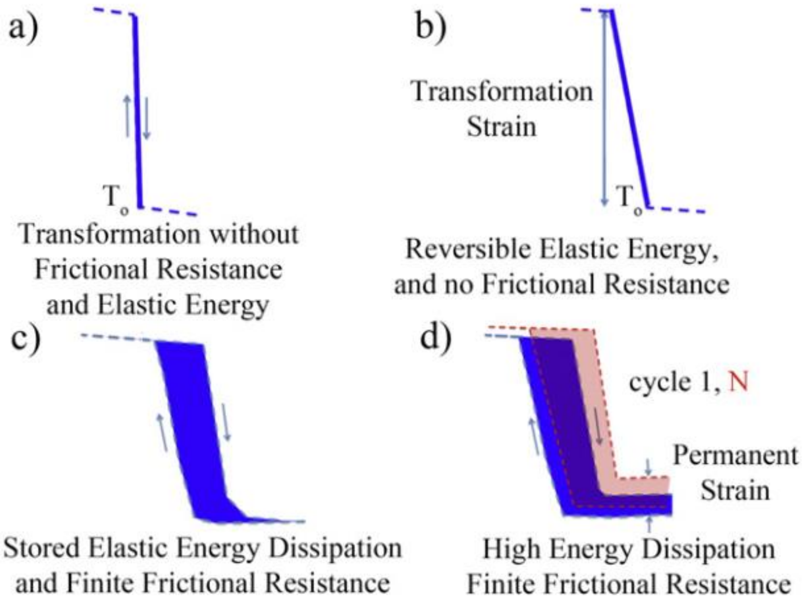

Figure 2.6. Hysteresis formation in martensitic transformation for different theoretical cases [27].

Energy dissipation with phase transformation is the relaxation of elastic energy ΔG_e which is stored during martensitic transformation and used during reverse transformation. Hence with the dissipation of elastic energy, transformation hysteresis increases and more energy should be spent for the transformation. It was also shown that chemical composition of NiTi alloy changes the evolution of hysteresis in thermomechanical cycling. NiTi alloy with coherent precipitates in the matrix yielded decreasing hysteresis with increasing stress, while NiTi alloy with lower Ni content showed increasing hysteresis [26]. As a result, chemical composition and microstructural differences between alloys also determine the damage formation, in other terms, dislocation formation and accumulation characteristics. Additionally it has been reported that initial casting structure may result different functional behavior, especially the presence of non-metallic inclusions such as oxides and carbides that are known to be detrimental to fatigue life [35]. Consequently, every batch of the same cast alloy shows different damage evolution characteristics and functional fatigue life.

2.1.4. NiTi and NiTi Based Alloys

In this section, a brief introduction to NiTi shape memory alloys will be made. Nickel Titanium shape memory alloys are mostly denoted as NiTi and were also named after their first discovery in Naval Ordnance Laboratory, as Nitinol. NiTi based alloys show higher load bearing capacity than that of the other shape memory alloys and may yield complete recovery in shape memory effect even under high loads. In addition, corrosion resistance of the alloy is superior to other shape memory alloys [19,36].

Phase diagram of binary NiTi alloys was extensively studied. B2 phase in Figure 2.7 is the austenite (or named as parent) phase and it was found that austenite phase might also present at lower temperatures depending on the chemistry of the alloy. $TiNi_3$ and Ti_2Ni phases can also present as intermetallic type precipitates in the matrix [37]. Later Nishida and his coworkers found for Ni rich NiTi alloys that with lower aging temperatures and shorter aging times Ti_3Ni_4, for intermediate temperature and times Ti_2Ni_3 and for longer aging times $TiNi_3$ precipitates can be intentionally formed [38]. On the Ti rich side, Ti_2Ni precipitates can be formed in NiTi alloys that have near equiatomic chemical composition [39].

Solutionizing heat treatment leads near-equiatomic NiTi alloys to transform fully into B2 phase and then NiTi alloys undergo martensitic transformation from B2 to B19’ phase with cooling. Thermal cycling reveals another intermediate martensitic type phase transition for NiTi alloys which is denoted as R phase and transformation became B2 to R to B19’ [40].

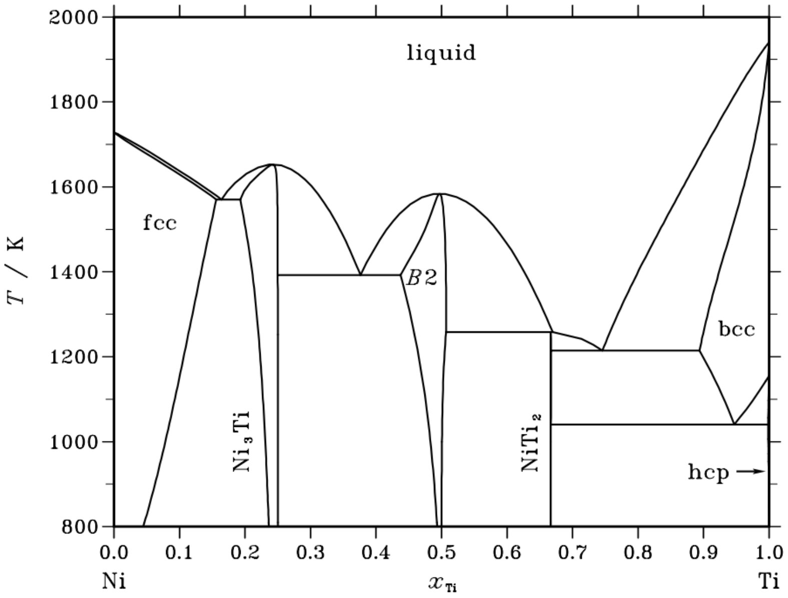

Figure 2.7. Phase diagram of NiTi binary system [41].

It was found that Ni rich NiTi alloys without precipitates has sub-zero M_s temperatures. Although, Ti rich NiTi alloys have higher M_s temperatures than that of NiTi alloys with Ni rich compositions, it was revealed that precipitate formations via aging decreases the nickel amount in the matrix. As a result, nickel rich compositions offer the advantage of tailorable transformation temperatures and strength via precipitation hardening [42]. Figure 2.8 shows how aging time affects the transformation temperatures in nickel rich alloys while titanium rich alloys are not affected by the aging time.

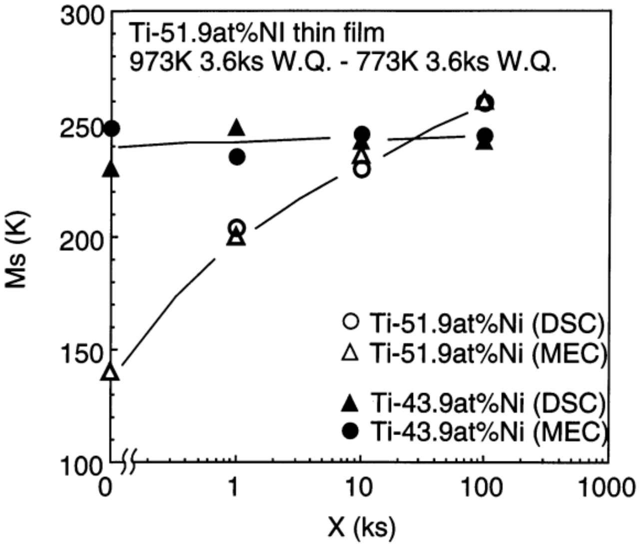

Figure 2.8. Martensite start temperatures of 51.9 at%Ni and 43.9at% Ni NiTi alloys with respect to aging time at 500°C [42].

Tertiary alloying elements are added to NiTi alloys, which have been the most promising shape memory alloy, in order to enhance shape memory properties. TiPdNi, TiPtNi alloys were produced and it was found that transformation temperatures were increased up to 600°C [43]. Cu addition as tertiary element resulted more stable transformation temperatures and lower hysteresis with respect to binary NiTi alloys. At the cost of transformation strain, $NiTiCu_{10}$ also yielded more stable transformation strains with thermomechanical cycling [44]. In the next section high temperature shape memory alloys and especially NiTiHf alloys will be covered.

2.2. High Temperature Shape Memory Alloys

High temperature shape memory alloys (HTSMAs) first reported by Donkersloot with the studies on Gold Titanium, Platinum Titanium, Palladium Titanium shape memory alloys which have phase transformation temperatures above 100°C [45]. Later it was found that gold (Au), platinum (Pt), palladium (Pd), zirconium (Zr) and hafnium (Hf) additions to NiTi as tertiary element increase transformation temperatures and still maintaining shape memory properties to a degree [46]. Since Au, Pt and Pd are precious metals and commodities, cost concerns steered researchers to Zr and Hf alloying elements. In the last decade, NiTiHf alloys have been studied extensively and compared with NiTiZr alloys. It has been showed that precipitation hardened NiTiHf alloys showed higher work-output values [3]. Also, NiTiHf alloys were found to be much easier to train for TWSME due to relatively lower stress requirements of NiTiHf for the reorientation of martensites [4].

2.2.1. NiTiHf High Temperature Shape Memory Alloys

NiTiHf alloys were first introduced in 1995 as Ni lean NiTiHf alloy. It was reported that 30at% Hf addition at the expense of titanium to 49at%Ni-51at%Ti alloy increases the M_s temperature to 525°C [47]. Since NiTiHf alloys are produced by substitution of Hf with Ti, Ti rich term was replaced with Ni lean.

Thermomechanical experimentation on NiTiHf alloys revealed that Ni lean alloys does not show superelasticity and no pletau region, hence no detwinning occurred [48]. Lack of superelastic behavior was explained with slip instead of detwinning of the martensite, TWSME studies also showed that TWSME was lost with cycling due to low CSS of martensite [49]. NiTiHf alloys showed higher thermal hysteresis than that of NiTi alloys and it was explained with lower mobility of the martensite austenite interphase due to high incompatibility between the phases [50,51]. Detwinning of martensite found to be not favorable which explains the non-existence of superelasticity. Ni lean NiTiHf alloys preferred slip and new twinning variant formation instead of detwinning [51]. Firstov and his coworkers suggested precipitation hardening in order to overcome the degradation of SME so that martensite phase would be strengthened and detwinning would be possible instead of slip [52]. Kockar et al. reported that severe plastic deformation using equal channel angular extrusion creates sub-micron grain structure and increase cyclic stability of the 49.8at%Ni-42.2at%Ti-8at%Hf alloy [53]. Meng et. al. used Ni Rich 50.6at% Ni – 30at%Ti – 20at%Hf alloys and showed that aging at 500°C for 5 hours resulted elliptical precipitates with 50nm average size [54].

Karaca et al. and Bigelow et al. were the first ones to report the effect of precipitation hardening on the thermomechanical performance of Ni Rich NiTiHf alloys [55,56]. NiTiHf alloy with the composition of 50.3 at%Ni- 30at%Ti – 20at%Hf performed full superelastic recovery up to 2% strain and near perfect SME stability up to 500 MPa loading condition [55]. It was also shown that precipitation formation increases transformation temperatures by lowering nickel content in the matrix. This behavior also allowed researchers to fine tune transformation temperatures for the application. Therefore, Ni rich NiTiHf alloys have become very promising candidates for smart actuator design [1]. Researchers focused on 50.3 at%Ni- 30at%Ti – 20at%Hf in order to enhance the cyclic abilities and investigate high temperature resistance and high load bearing capacity by forming precipitates via aging heat treatment [4,7,9,10,35,57–61]. Further investigations focused on crack initiation and crack propagation with the thermal cycling under stress [62,63]. Limiting actuation strain was also studied in order to achieve higher functional fatigue cycles [8,64]. Increase in Hf content has been already known to be increasing TTs. Figure 2.9 shows how nickel content is affecting TTs in as solutionized condition and the evolution of TTs with the increase in Hf content.

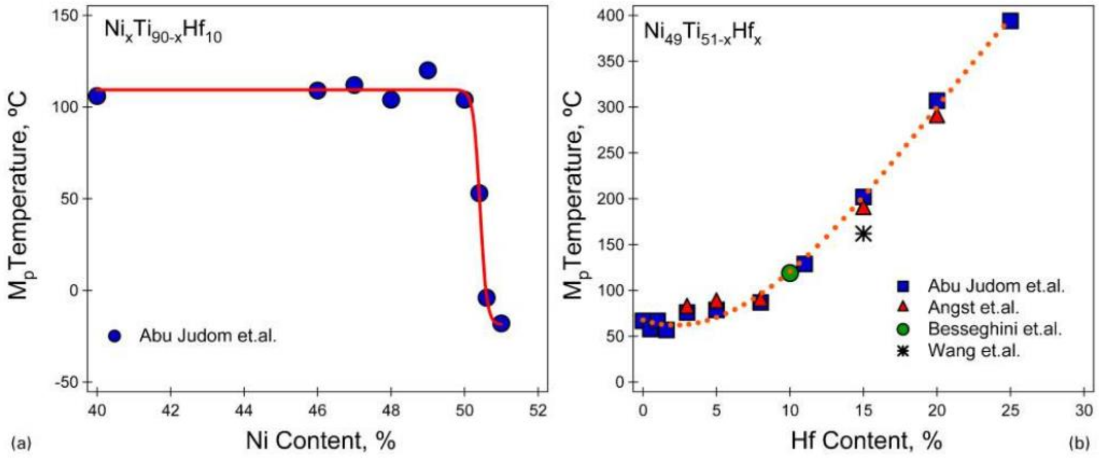

Figure 2.9. Martensite peak temperatures for a) effect of Ni content a) effect of Hf content [59].

NiTiHf alloys with higher hafnium content were investigated to acquire very high temperature shape memory alloys [65,66]. However, it was also shown that increasing UCT, which is necessary to achieve full austenite, decreases the functional properties of the NiTiHf alloys [9]. It was explained with dislocation annihilation and creep plasticity which are expected to start over 300°C. Lately the topic of creep plasticity on NiTiHf alloys was taken into consideration [67,68]. Cyclic behavior of NiTiHf alloys has not been investigated by giving attention to creep viscoplasticity since transformation temperatures of the alloys studied up to this point were 300°C and below.

2.3. Creep Theory

Creep deformation is defined as viscoplastic deformation of metallic materials under loading at high temperatures that are above more than half of melting temperature in Kelvin (T > 0.5Tm) [69]. Industrial applications that involve high stress bearing capacity at high temperatures require solutions for creep deformation. As a result, creep experiments are conducted at high temperatures via loading tensile samples to constant force or constant stress. Results of the constant stress experiments yield much better correlation with phenomenological creep model. Hence, constant load creep experiments can only be run when creep damage is low enough to minimally affect the tensile stress on the sample. A creep curve with nominal values that is drawn from a creep experiment result is shown in Figure 2.10. Stage I, stage II, stage III represent the primary creep formation, steady state creep deformation or secondary creep and tertiary creep formation, respectively.

Primary creep is named as region at which the deformation rate decreases with time due to the strain hardening during creep deformation since the rate of dislocation formation is much higher than that of dislocation annihilation. Steady state creep or secondary creep deformation zone is the stage where dislocation formation rate is equal to dislocation annihilation rate so that deformation increases linearly. Tertiary creep formation is third stage of the creep curve where dislocation annihilation rate is much faster and damage is extensive [69].

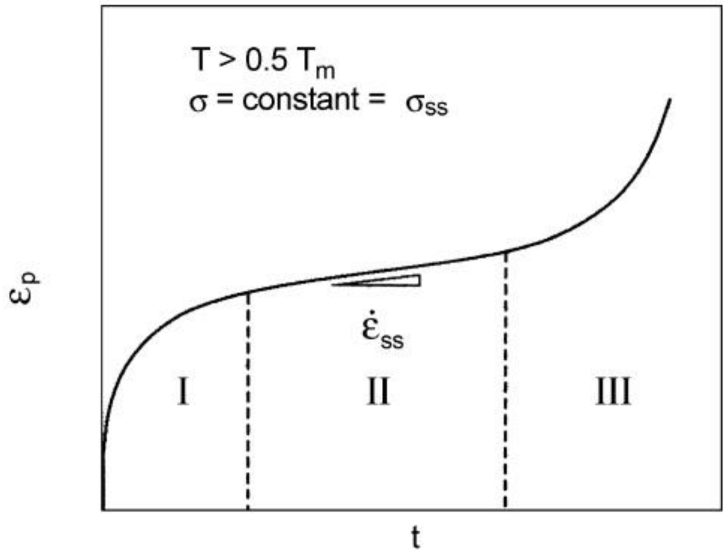

Figure 2.10. Creep deformation curve for constant stress experiments [69].

Another creep experimentation type is constant strain rate experiments. Using universal mechanical test machines, tensile experiments at high temperatures with strain rates below $10^{-5}\ s^{-1}$ would yield strain-stress plot as that is shown in Figure 2.11 [69].

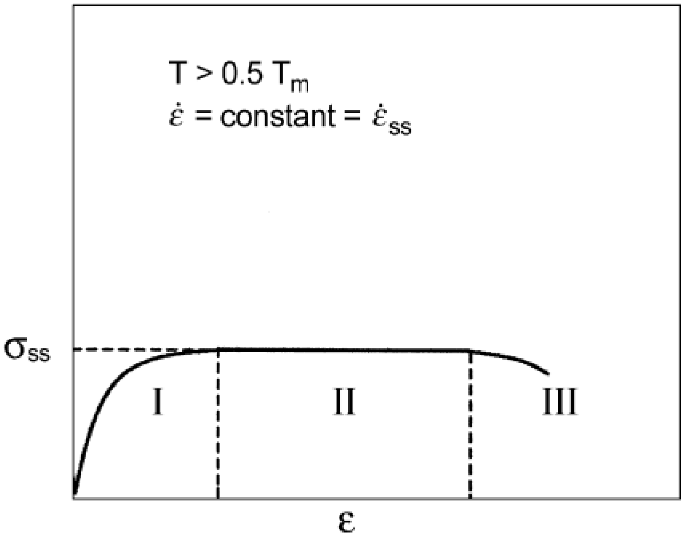

Figure 2.11. Creep deformation curve for constant strain rate experiments [69].

Constant strain rate experimental results are also used for calculating creep model parameters. In constant strain rate creep experiments, strain rate is the experiment variable and stress variation is the result of the experiment.

First model on creep deformation using phenomenological approach to explain characteristics of deformation at high temperatures was published by Norton [70]. Power Law Equation was defined as [71]:

$$\dot{\varepsilon} = A0\ (\sigma/E)^{n}\ e^{-Qc/kT} \qquad (1)$$

In this equation $\dot{\varepsilon}$ and σ corresponds to strain rate (s^{-1}) and stress (MPa), respectively and A0 is the material constant, k is the Boltzmann's constant and T is the experiment temperature in Kelvin. E is the young's modulus of the material since at higher temperatures Young's Modulus may change and has to be considered accordingly. Qc is activation energy of creep and n is the stress exponent. However, power law equation is denoted differently in this thesis. Since NiTiHf alloy was in austenite phase at the temperatures at which the creep experiments were conducted, thus, there should not be any change in the magnitude of the elastic modulus value of the alloy and k Boltzmann constant is equal to ideal gas constant R considering 1 mole of alloy. Power law equation is used in the following form [12]:

$$\dot{\varepsilon} = A\ \sigma^{Na}\ e^{-Q/RT} \qquad (2)$$

Dislocation climb creep is also called five power law creep where n in the first equation and Na in the second equation is between 4-7 [71]. Diffusional creep term is used for lower n values that are about 1-2 [72]. Viscous Glide creep is defined when a limiting factor inhibits dislocation movement and n stress exponent is generally around 3 [73].

2.3.1. Dislocation Climb Creep

Dislocation Climb term corresponds to climb of dislocations perpendicular to their glide plane in relation with the movement of vacancies to or away from dislocations [74]. Five Power Law Creep term is defining creep mode when the stress exponent in power law model is about 4-7 and generally it is related with dislocation climb movement. Dislocation climb creep is seen in pure metals and defined with the slope of the stress versus strain rate graphic. In Figure 2.12, y axis is defined as normalized strain rate with lattice diffusion rate (D_{sd}) so that experimental values at different temperatures formed as straight line.

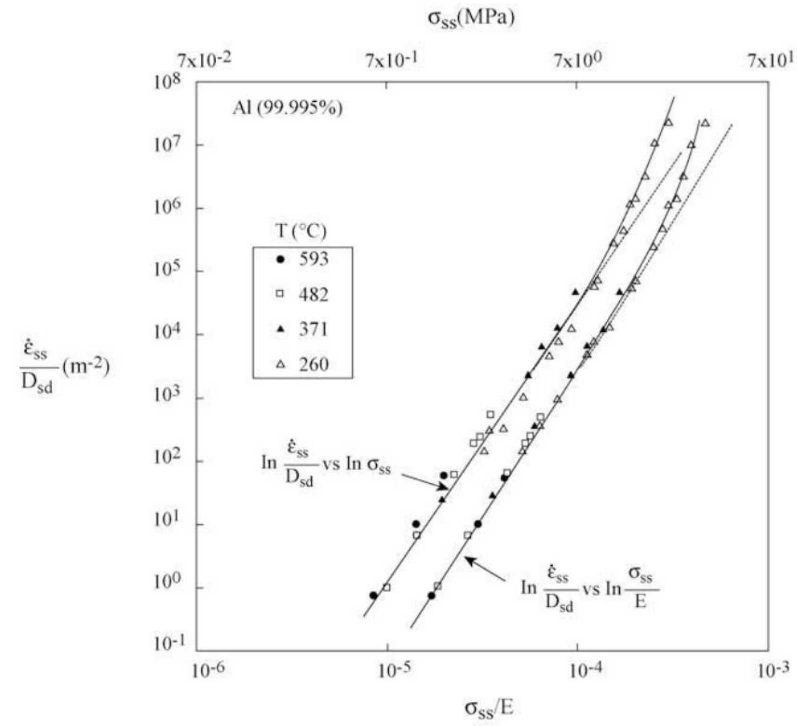

Figure 2.12. Five power law creep in pure aluminum [71].

As seen in Figure 2.12, dislocation climb creep is forming a line up to a certain stress level at which power law break down (PLB) starts to take place. This behavior is consistent for all pure metals having hcp, fcc, bcc crystal structures [71]. Relation of activation energy and stress exponents is presented in Figure 2.13.

Five power law creep is accepted as diffusion controlled creep mechanism. Activation energy of creep deformation generally equals to the activation energy of lattice self-diffusion.

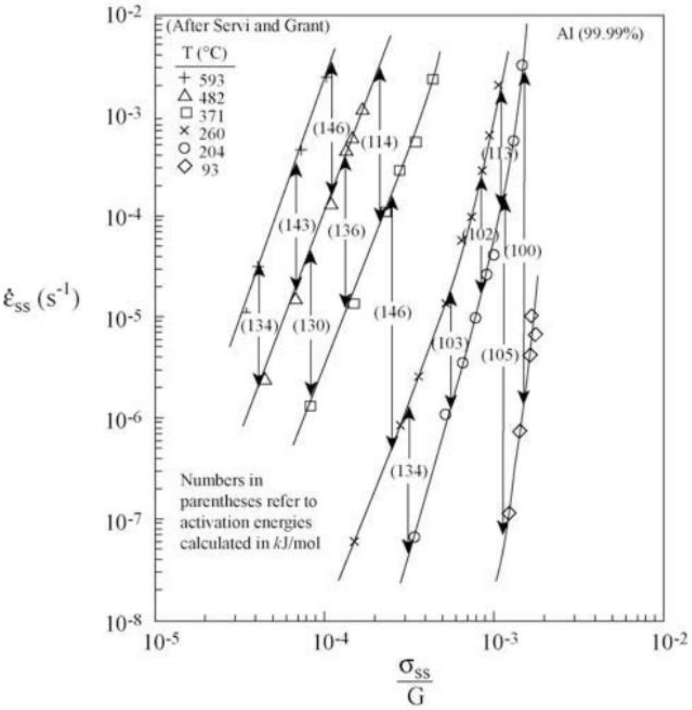

Figure 2.13. Stress exponents and activation energies for pure aluminum [71].

Stress exponents can be drawn in separate lines considering different temperature levels. Activation energy values can be calculated between the temperatures for the same stress levels. In order to calculate activation energies, exponential part of the equation is used as plotted in Figure 2.14.

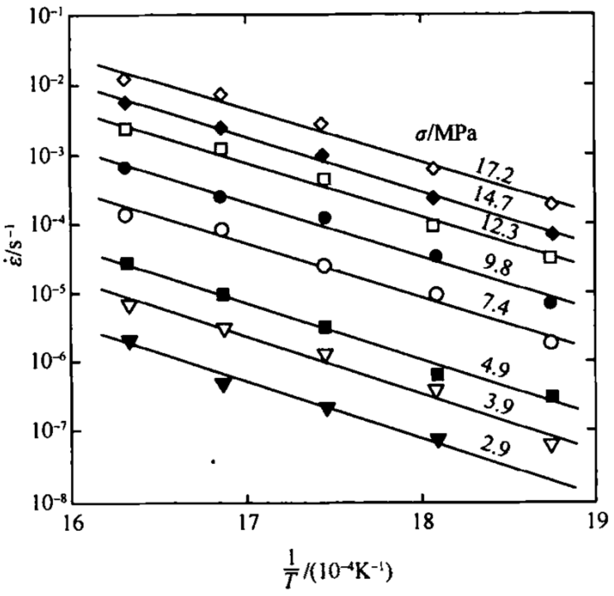

Figure 2.14. Activation energy plot for pure aluminum [74].

It should be noticed that all lines in Figure 2.14 are linear fits to experiment results at different temperatures under same stress levels.

2.3.2. Diffusional Creep

Diffusional creep term explains creep behavior at high temperatures (T ≈ Tm) under low stresses [75,76]. Mass transport is not related with dislocations but with vacancy movement to grain boundaries. Diffusional creep can be called when the stress exponent is between 1 and 2. Figure 2.15 shows diffusional creep and dislocation climb creep formations for pure aluminum.

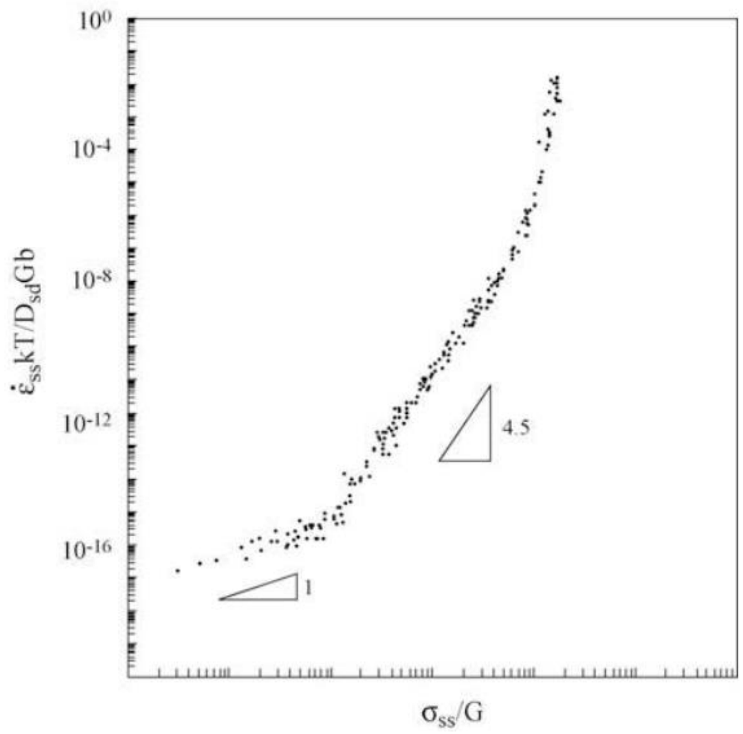

Figure 2.15. Diffusional creep and dislocation climb creep for pure aluminum [71]

It should be noticed that y axis in Figure 2.15 represents the strain rate that is normalized with boltzmann's constant k, temperature T, self-diffusion term D_{sd} and bulk modulus G_b. At lower stresses and high temperatures diffusional creep is present and at higher stress values stress exponent is measured at 4-5 until the PLB occurs.

2.3.3. Viscous Glide Creep

Viscous glide creep deformation is defined as the creep deformation under the influence of a limiting factor and only seen in solid solutions. Several explanations were made on possible rate controlling factors for dislocation motion. It was proposed that rate of migration of solute atoms are limiting the dislocation motion [77]. Another proposed hypothesis was the stress induced ordering of solute atoms which was inhibiting the dislocation motion [78]. However, rate controlling mechanisms behind viscous glide creep is still not clear. Viscous glide creep deformation behavior in Al-Mg alloy is presented in Figure 2.16, where lower and higher stresses lead to acquire the stress exponent of 5 and intermediate stresses yield the stress exponent of 3.

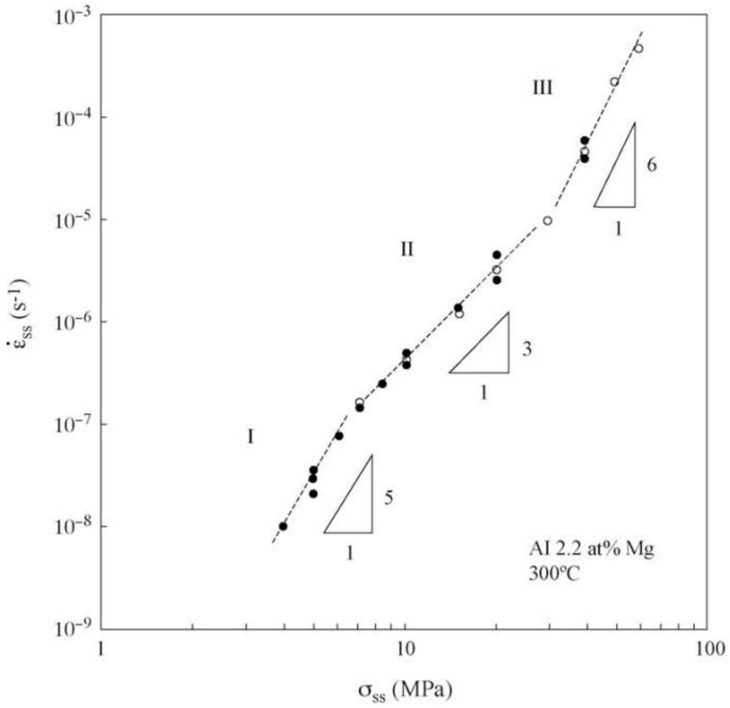

Figure 2.16. Viscous glide creep of Al-Mg alloy [73].

2.3.4. Creep of Shape Memory Alloys

A part of this section was published in Materials Today Communication December 2022 issue article number 104827.

Creep studies on NiTi binary alloys provides the basic theoretical background that was focused on in this study. Creep properties of binary NiTi SMAs were first investigated by Mukherjee et.al. using constant strain rate creep experiments between 700 °C to 1000 °C temperature range under vacuum conditions considering the creep rate dependency with the applied stress and the testing temperature [79]. The creep experiments in this study were conducted under tension; however, the stress and strain values were converted to shear stress and strain values, respectively. The stress exponent of NiTi was reported as 3 and found to be independent on temperature. Additionally, it was stated that the activation energy was calculated as 251,04 kJ/mol (60kcal/mol) and not stress related [79]. Moreover, the creep deformation mechanism was mentioned as viscous creep considering the aforementioned stress exponent [79]. This first creep study on NiTi SMA gave a lead to the studies to focus on hot deformation of these alloys [80] and shape memory effect trainings [19].

Another study provided creep results of three different NiTi alloys which contain 49.5mol% Ni, 50mol% Ni and 50.5mol%Ni [81]. Kato et al. reported the grain size of wire specimen, after annealing at 900°C for 12 hours, as 15 microns. Tensile tests were run with varying strain rates at 827^{o}C and it was determined that strain rate values lower than $10^{-5}s^{-1}$ led to observe diffusional creep stress exponent while tensile experiments that were run with higher strain rates on all samples yielded stress exponent of 5-6, which was actually the sign of the dislocation motion. In addition, constant load creep experiments were done under vacuum atmosphere at 727 ^{o}C, 777 ^{o}C, 827 ^{o}C, 877 ^{o}C temperatures under loads equivalent to 17 MPa, 25 MPa, 33 MPa. Creep experiments provided a stress exponent of 2.5 for samples which contain 50mol% Ni and higher and this value was the indication of dislocation glide type creep deformation. However, samples that contains 49.5mol%Ni were creep tested and Na was calculated as 5.78 and 3.5 for the test temperatures 727 ^{o}C and 777 ^{o}C, respectively. In addition, Na value converged to 2.5 with the increase in testing temperature as shown in Figure 2.17. For temperatures at and above 777°C, creep mechanism was found as viscous glide with the stress exponents around 3[73]. It can be claimed that the increase of Nickel content in the matrix led to an expansion of temperature range between which viscous glide is the main creep mechanism.

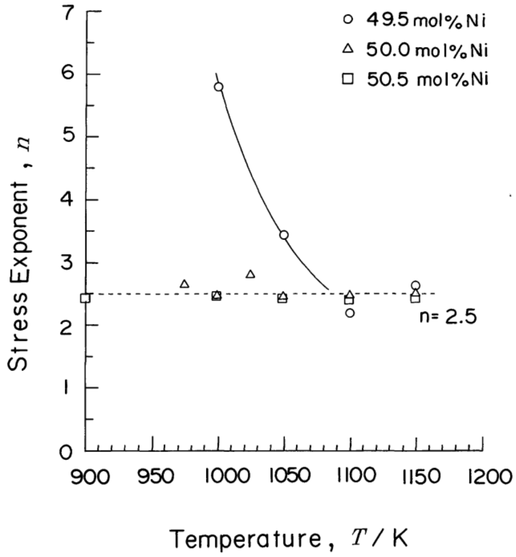

Figure 2.17. Change in stress exponent with higher experiment temperatures [81].

Furthermore, creep experiments were conducted on hot drawn equiatomic NiTi alloy under constant tensile load by Lexcellent et al. [82] and it was reported that stress exponent was also found to be 3 and activation energy was determined as 226 kJ/mol.

This activation energy for creep was different than that of the Ni tracer-diffusion that was determined as 155kJ/mol in a previous study [83]. Thus, it was claimed that creep activation energy of NiTi should be close to the activation energy of Ti self-diffusion[82].

Eggeler et al. contributed to the creep deformation studies using Ni Rich NiTi with constant load experiments that were conducted under 90-150 MPa at 470°C and 530°C [84]. Grain size for as received rod shaped specimen, after solution annealing at 850°C for 15 minutes, was reported as 35 microns. It has been reported that strain rate first decreased, then increased and stabilized so that stress exponent and activation energy values were calculated for two different strain rate values. For the minimum strain rate, stress exponent was found to be 2 and activation energy was calculated as 334 kJ/mol. On the other hand, when the stabilized strain rate was taken into account, stress exponent was increased to 4.7 and activation energy was calculated as 304kJ/mol. Considering these results, researchers concluded that interparticle spacing between precipitates increased with the time and this led to observe lowering the creep resistance of the material due to coarsening of precipitations during creep experiments [84].

Oppenheimer et al. investigated creep using Ni rich alloy (50.8at%Ni) under compression stresses (3-11 MPa) at much higher temperatures (950-1100°C) [85]. In this study, stress exponents and activation energy values were found as 2.7 and 150kJ/mol, respectively. Oppenheimer claimed that tension-compression asymmetry may be the reason for the difference in Q and Na values with respect to the previous creep studies [85]. Later, in another study, the data of Oppenheimer et. al. were used and the results were compared with Mukherjee's first study. It was again concluded that creep behavior of NiTi was controlled by the diffusion of Titanium element since the activation energy for Titanium diffusion was stated as approximately 200 kJ/mol [86].

The creep behavior of near-equiatomic NiTi with respect to stress changes and phase transformation was determined to be different at relatively lower temperatures than that of the creep behavior of NiTi at higher temperatures [87]. 5000 hours long creep experiments on martensitic NiTi at approximately room temperature demonstrated an incubation period for martensitic variant formation. The strain formation was later observed. Unloading of martensite phase resulted negative strain rate during several thousand hours of creep experiment and this observation was related with anelastic strain. On the other hand, austenitic NiTi showed primary creep deformation when the alloy was kept at 200°C through the entire experiment and the steady state creep was not observed.

Therefore, researchers claimed that both anelastic strain formation and long primary creep behavior suggest viscous glide creep mechanism for low temperature creep deformation of NiTi [87].

Creep properties of TiPdNi HTSMAs have been already studied and in these studies, heating-cooling cycles via using different rates were run under constant tension stress [11,12]. It has been stated that lower heating cooling rates increased the time spent at higher temperature hence increased the creep deformation of the samples. In one of the aforementioned studies on TiPdNi alloy, two creep experiments were run on 50 at%Ti 40at%Pd 10at%Ni alloy at 520°C and stress exponent was calculated as 4 [11]. In the other study six different creep experiments were conducted for the calculation of creep parameters [12] and stress exponents were found to be 1-2, which dictates diffusional creep mechanism, from the results of the creep experiments that were run under 100 and 300 MPa stress values at 300ºC and 400ºC. Additionally, activation energy was also found around 200 kJ/mol. Stress exponents were calculated as 4, which dictates dislocation climb mechanism, and activation energy was found to be around 260 kJ/mol from the creep experiments that were run under higher loads. Interestingly, creep experiments that were conducted at 500°C under 300 and 500MPa resulted a stress exponent of 8 and this value was explained as power law breakdown with an activation energy of 200 kJ/mol. For simplicity, the summary of the aforementioned creep studies on NiTi-based shape memory alloys and stress exponent together with activation energy values that were drawn from these studies are given in Table 2.1.

Creep deformation of NiTiHf alloys at high temperatures during functional fatigue experiments was studied for 49.8%atNi-30.6at%Ti-19.2at%Hf alloy as well. Transformation plasticity and creep were investigated using three different heating cooling rates by setting the UCT at 500°C. The result of the constant load creep experiment that was conducted for 150 hours was compared with the result of thermal cycling under constant tensional load that was run using 10°C/min heating cooling rate together with the result of an alternating thermal cycling under constant load experiment during which the sample was also held under the same load for a period of time. It was shown that viscoplasticity due to creep at 500°C was much lower than that of the strain due to the transformation induced plasticity (TRIP) during functional fatigue experiments, however, effect of creep increased as the heating-cooling rate during functional fatigue experiment was decreased [67].

Table 2.1. Summary of the creep studies that were conducted on NiTi based shape memory alloys in the literature [68].

	Material	**Method**	**Temp. (°C)**	**Load - MPa (StrainRate)**	**Na**	**Q (kJ/mol)**
Mukherjee 1968 [79]	NiTi Ni Rich 55%	Constant Strain Rate	700-1000	(4.3e-4 to 4.4e-2)	3	251
Kato et al. 1998 [81]	NiTi 3 alloys	Con. Strain Rate	777	(e-5 to e-1)	1-4	
		Con. Load	723-977	17-33	2.5	250
Eggeler et al. 2002 [84]	NiTi Ni Rich	Con. Load	470-530	90-150	2 4.7	334 304
Lexcellent et al. 2005 [82]	NiTi Equia.	Con. Load	600-900	10-35	3	226
Oppenheimer et al. 2007 [85]	NiTi Ni Rich	Con. Load (Compres.)	950-1100	3-11	2.7	150
Kumar et al. 2011 [12]	TiPdNi 19.5 at% Ni	Con. Load	300-500	100-500	1-4.5-8	200 260

3. EXPERIMENTAL PROCEDURES

3.1. Characterization of Material

3.1.1. Properties of As Received Material

50at% Ni - 25at%Ti - 25at%Hf material was bought from Sophisticated Alloys Incorporation, USA. Alloy was cast from pure elemental Nickel, Titanium and Hafnium using vacuum induction melting. After casting, as cast alloy was placed in a mild steel can and material was subjected to high temperature extrusion in order to homogenize the chemical composition of the cast billet. NiTiHf material is secured from severe oxidation by using mild steel can as a protective cover at extrusion temperature of 900°C. Extrusion operation was aimed for 4:1 area reduction so that the diameter of the as cast material that is approximately 25 mm was reduced to 10-12 mm diameter.

3.1.2. Differential Scanning Calorimetry

Differential Scanning Calorimetry (DSC) is essentially scanning a temperature range with a certain predetermined rate while measuring the changes in heat flow of the inspected material and also differentiating it from heat flow of the reference material [88]. DSC measurements reveal phase transformation of the material since the heat flow rate has to change during phase transformations due to energy spent during the rearrangement of crystal structure. In order to detect the phase transformation temperatures of the material Perkin Elmer DSC 8000 in Figure 3.2 was used to measure heat flow between 200°C and 500°C temperature range. Scanning rate for the temperature range was set to 10°C/min, throughout both heating and cooling. Samples for the DSC were cut using Metkon Micracut Precision Cutter (shown in Figure 3.1) at very low cutting speed in order to prevent plastic deformation of material during cutting process.

Figure 3.1. Metkon Micracut Precision Cutter

Figure 3.2. Perkin Elmer DSC 8000

3.2. Experiment Procedures

3.2.1. Sample Preparation for Tensile Testing

As explained in the previous section, as received material was in extruded rod shape with a diameter of 10-12 mm. It is worth to mention that diameter was not the same throughout the rod. The tensile test samples that have dog bone shapes were used in tensile experiments, functional fatigue experiments and as well as in creep experiments. Tensile samples were cut using wire electric discharge machining (WEDM) method from the extruded billet and sliced to 1 mm thickness. The dimensions of the sample are shown in Figure 3.3.

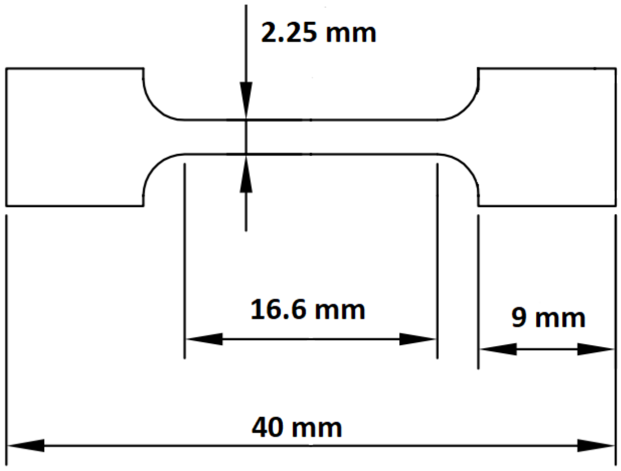

Figure 3.3. Tensile testing sample dimensions [68].

Tensile sample dimensions were scaled down with a ratio of 9/50 considering sheet metal tensile testing sample dimensions that are given in ASTM-E8M [89]. Scaling ratio was selected due to 10 mm gauge length and 5 mm ceramic rod diameter of the Epsilon® high temperature extensometer.

3.2.2. Heat Treatments

In order to successfully implement creep and functional fatigue experiments, as extruded samples were annealed at 550°C for 3 hours in order to eliminate shape memory and actuation property variations. Variations were found to be caused by internal and/or residual stress formation due to extrusion. Annealing was found to be stabilizing and making the functional fatigue behavior of the shape memory alloys consistent as it was explained in a previous publication [90]. Additionally, in the Functional Fatigue Experimental Results section of the Results and Discussion Chapter, extruded and annealed samples were discussed in order to demonstrate the necessity for annealing. Samples which were heat treated at 550°C for 3 hours will be denoted from now on as An550-3.

In order to study extensive creep characteristics of the alloy, another heat treatment procedure was implemented. Grain growth heat treatment at 800°C for 10 hours period was performed in order to investigate creep characteristics of the samples that have greater grain structure. Samples which were grain growth heat treated at 800°C for 10 hours will be denoted in the text from now on as GG800-10. All heat treatments were performed at open air conditions on bulk material, with the presence of mild steel can from the extrusion process. Tensile samples were cut afterwards from at least 5 mm away from the surface and oxide layers were further removed. Gauge sections of the tensile samples were also 14 mm away from the surface. Oxidation of the NiTiHf material were not the main focus in this thesis, however in literature it was stated that Hf rich oxide layer was formed on NiTiHf materials that would inhibit Ti ion diffusion and prevent further oxidation unlike NiTi shape memory alloys [91]. On the other hand, it was also stated that, Hf rich layers did not prevent further oxygen diffusion through inward of the material [92].

3.2.3. Sample Preparation for Optical Microscopy

Optical microscopy was utilized in order to reveal the grain structure of the alloys for investigating the evolution by heat treatment conditions. Samples were cut using Metkon® Micracut™ Precision Cutter and placed in cold mount epoxy resin for grinding operations. Grinding was performed using Metkon® Forcipol™ Grinding machine (Figure 3.4) with grinding papers starting from a grid size of 400 to grid size of 2500. Upon finishing grinding, samples were polished using diamond suspension with 6 μm, 1 μm and 0.25 μm powder size in order to eliminate surface roughness.

Figure 3.4. Metkon Forcipol Grinding Machine

Polished samples were etched using an acid solution which has 85:12:3 ratio of deionized water, nitric acid and hydrogen fluoride respectively [93]. Etchant was prepared in a chemical durable glass and dripped on to the surface of the material. Optical microscopy studies were conducted using Nikon® Eclipse LV150 Optical Microscope, shown in Figure 3.5, which has a magnification capability of 50x to 1000x. Optical micrographs were captured using Clemex® imaging system which includes a camera and image transfer interface attached to the microscope.

Figure 3.5. Nikon Eclipse LV150 Optical Microscope with Clemex Imaging Apparatus

Additionally, Scanning Electron Microscopy (SEM) was utilized to analyze the formations that appeared by etching the alloy. Energy Dispersive X-ray Spectroscopy (EDS) was also used for the identification of the oxides.

3.2.4. Tensile Experiments

Tensile experiments were utilized in order to reveal strength of the material at high temperatures. From DSC curves, transformation temperatures were found under no load condition. However, it has been known that transformation temperatures increase with loading. This may result stress induced martensite formation with loading at the beginning of the creep experiments which would eventually effect the creep behavior of the material. In order to clarify the effect of loading conditions, tensile experiments were conducted at 390°C, 450°C and 520°C temperatures for An550-3 samples and at 500°C for GG800-10 sample. Utest® Universal Mechanical Testing Machine was used for the tensile experiments with custom made heating system attached to the grips. Heaters, which are presented in Figure 3.6, are 700W plastic injection molding heaters with a capacity of heating the grips up to 600°C. Grip material were made from high temperature resistant die steel which can maintain hardness up to 450°C - 500°C for a short time period. Tensile rate was determined to be 0.5 mm per minute which corresponds to 5 x 10^{-4} s^{-1} strain rate. Since the creep strain rates for constant strain rate creep experiments were known as lower than 10^{-5}, the predetermined strain rate was suitable for tensile experiments.

Figure 3.6. Utest Mechanical Testing Equipment with custom made heating system a) heaters attached to grips b) during experiment

3.2.5. Experiments on Functional Fatigue Test Setup

3.2.5.1. Functional Fatigue Test Setup

Functional Fatigue Testing Setup is an in house made setup specifically designed to test functional properties and total thermo-mechanical cycling capacity of shape memory alloys [7,8]. Functional fatigue test setup that is presented schematically in Figure 3.7 consists a data acquisition and control system, DC power supply, position and temperature sensors. Control algorithm was written in NI Labview® for controlling a programmable DC power supply. Power cables from the power supply was directly connected to the grips, enabling DC current to pass through the material which is called as Joule Heating, so that heat was generated by the internal resistance of the material itself.

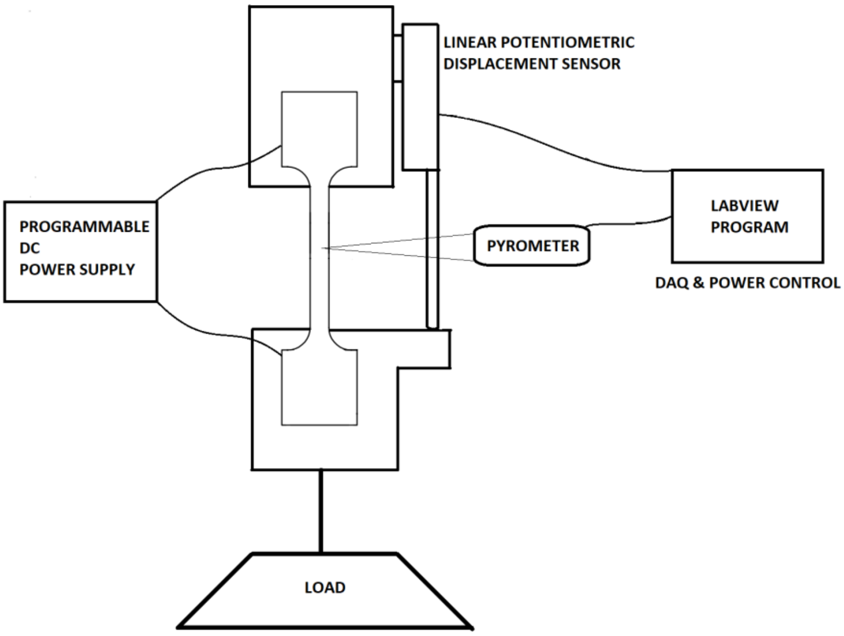

Figure 3.7. Schematic of Functional Fatigue Testing Setup [68].

Temperature of the sample was measured by a high temperature pyrometer from which the data was transferred to NI Labview® via data acquisition hardware. Pyrometers measure infrared thermal radiation of the sample surface which is only possible if the black body emissivity of the surface is known [94]. On the other hand, NiTiHf alloys interacts with oxygen above 500°C and surface emissivity changes with the coloration (color turns blackish blue) due to oxidation [91]. As a result, emissivity of the surface must be fixed in order to achieve consistent surface temperature measurement. A high temperature resistant black paint with an emissivity value of 0.98 was sprayed to the surface of the samples for all tests that were done in Functional Fatigue Testing Setup. However, applied black paints were not able to show endurance to both high temperatures and high strains. As a result, peeling off of black paint was observed during functional fatigue experiments due to high strain formation. Peeling off instantly decreases measured temperature, which leads the control system to increase sample temperature. Thus the real UCT value of the experiment increases while control system tries to reach the set UCT value. In order to prevent black paint failure, functional fatigue experiments were stopped at every 50 to 100 cycle for repainting. Results that were obtained from samples, which were failed due to black paint failure were also included in result and discussion chapter to reveal the peeling off effect of black paint.

Functional fatigue test setup has a capacity of applying up to 60A DC current that can pass through the sample which is enough to melt NiTiHf tensile samples with gauge dimensions that were presented in Figure 3.3. Control algorithm was designed using PID control methodology which controls the direct electric current to heat the sample so that both heating and cooling rate can be controlled with in 2°C error of the set temperature [95]. With this capacity, samples could be cycled between set temperatures at a given rate and held at a certain temperature. Hence, functional fatigue experiments and creep experiments were performed via utilizing the same test setup.

3.2.5.2. Functional Fatigue Experiments

Functional fatigue experiments are the simulations of actuator applications of the shape memory alloys. Main aim of the experiments is to determine the functional behavior of the material up to either a predetermined cycle number or loss of functional properties and failure which reveals the ultimate cycle limit of a shape memory alloy. Determining functional behavior up to a certain limit shows the actuation capacity of the alloy for a certain application procedure. On the other hand, finding the ultimate cycle limit of a shape memory alloy reveals the total life cycle of a shape memory actuator under testing loads.

Functional fatigue testing systems were designed in order to perform heating and cooling cycles with certain heating and cooling rates. Testing methods for shape memory alloys were standardized in the recent years [96], however standard testing systems have not been utilized for the functional fatigue experiments yet. Functional fatigue testing systems were designed in house as explained in the previous section, thus data acquisition and evaluation may vary according to the approaches of the researchers. For this reason, data evaluation will be explained in this section.

Functional fatigue experiments were conducted under constant force, as it was shown in Figure 3.7. Force was applied to the sample using dead weight. Infrared pyrometer was used in order to accurately measure the temperature of the sample during testing and the displacement of the sample at different temperatures was measured using displacement sensor. As a result, a functional fatigue experimentation data set is consisting the displacement of the sample at all temperatures between the predetermined temperature limits of the heating and cooling cycles.

Heating and cooling, upper and lower temperature limits were determined considering to the chemical composition of the shape memory alloy. Additionally, differential scanning calorimetry results were used as a starting point however; transformation temperatures tend to change with increased loading conditions as explained in the literature survey section. The highest temperature in a cycle was named as Upper Cycle Temperature (UCT) and lowest temperature in a cycle was named as Lower Cycle Temperature (LCT). UCT and LCT limits were calibrated during the first cycles of the experiment via determining the completion of the cycle with the observation of the horizontal curve which indicates completion of the phase transformation. Functional fatigue experiments consist of multiple consecutive cycles, a simplified version of strain vs temperature curves and the procedure to determine the specific strain magnitudes were presented schematically in Figure 3.8.

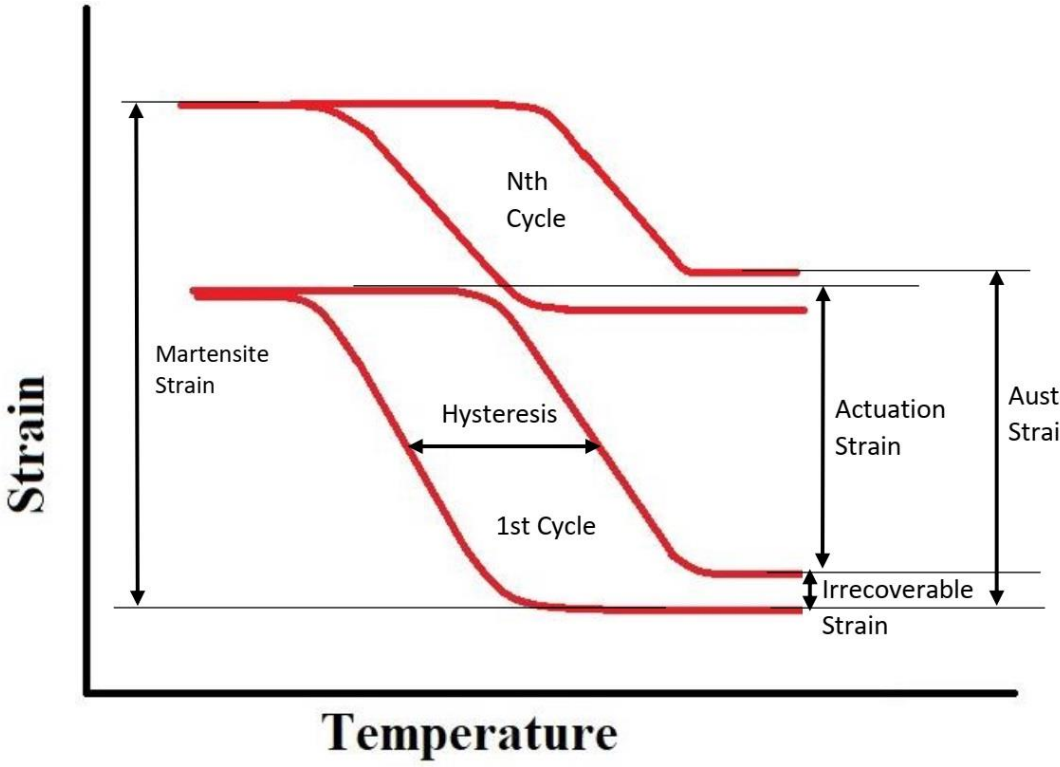

Figure 3.8. Schematic of functional fatigue experimental results

Dead weight was loaded in the austenitic phase so that the starting point of the experiment is UCT. Upon loading, sample is cooled down to LCT with a certain rate causing martensitic transformation. Martensitic transformation under constant loading causes martensite detwining which was expressed in experimental results as an increase in strain value. When sample reaches LCT, microstructure is assumed to be fully martensitic. After reaching LCT, samples are heated up to UCT, austenitic phase transformation occurs and recovers the strain formation.

Difference between the starting strain of the cycle in austenite phase and the strain that is achieved at UCT at the end of the cycle is called Irrecoverable Strain as shown in Figure 3.8. Irrecoverable strain occurs due to the dislocation generation either in the form of plastic strain or remnant martensite via martensite pinning. In either case, functional properties of the shape memory alloy decreases with each cycle with the increase in irrecoverable strain. Strain difference between LCT and final strain at UCT is called Actuation Strain. Actuation strain is the indication of functional property of the shape memory alloys, which is actually related to the work done against the applied load. Actuation strain values show how shape memory alloy maintain work output for the duration of the experiment. In some cases work output decreases with increasing cycle while in others work output may increase [7,9]

Austenite strain is defined as the last strain value of any cycle which indicates accumulated irrecoverable strain up to the given cycle. Austenite strain values show how damage accumulation progresses with thermal cycling. Martensite strain is defined as the strain value of any cycle while the sample is cooled down to LCT. Hysteresis is the thermal difference between the strain formation due to martensitic transformation and the recovery of strain formation due to austenitic transformation as shown in Figure 3.8.

In this thesis, functional fatigue experiments were conducted on Extruded, An550-3 and GG800-10 samples up to failure. Loading stress was selected as 200 MPa which was the optimum loading condition determined in previous works [7,8]. UCT and LCT values were determined to be 600°C and 200° respectively. Austenite strain values were compared with creep experimental results in order to show the evolution of irrecoverable strain accumulation with the deformation during creep experiments.

3.2.5.3. Creep Experiments

Creep experiments were conducted using functional fatigue testing setup. Functional fatigue experiment conditions were used as a basis for creep experiments in terms of loading conditions and selected temperature. Since UCT was used as 600°C, creep experiment temperatures were selected as 600°, 550° and 450°C for An550-3. Creep temperatures for GG800-10 samples were selected as 600°, 550° and 500°C due to very low strain formation at 450°C.

In order to start creep experiments, samples were heated up to test temperature without loading the deadweight. When sample was heated to the testing temperatures, DC current output values became slightly higher than the testing currents. This elevation in energy output was due to the heat transfer from the middle section of the sample to grips until the thermal equilibrium was reached. In order to prevent position sensor from collecting the thermal expansion of the grips, loading was delayed for 15 minutes. Experiments were commenced with loading the dead weight.

Creep experiments were ended with unloading and afterwards samples were cooled down to room temperature. True strain values were calculated from position data that were collected starting from the last data point before loading up to the last data point before unloading. Thermal expansion of the sample between room temperature and test temperature was ignored and initial gauge length was accepted as 16.6 mm since the thermal expansion magnitudes should be the same for all samples. True strain was calculated using position data and gauge length and results were plotted with time versus true strain plots. Strain rates in seconds were calculated by fitting line to minimum strain rate formation of the creep plot. Creep model parameters for NiTiHf material which are stress exponent (Na) and activation energy (Q), were calculated using the power law equation as explained in the previous chapter.

$$\dot{\varepsilon} = A\,\sigma^{Na}\,e^{-Q/RT} \tag{2}$$

Creep experiments, temperatures, loading and experiment durations were tabulated in Table 3.1 and Table 3.2 below in order to clarify the experiment procedures. Melting temperature was taken from the literature as 1450°C and creep temperatures were calculated in terms of Tm as shown in table [97].

Table 3.1. Creep experiments conducted on An550-3 samples [68].

Temperature	**Initial Stress and Duration**
450 °C 723 °K = 0,42 Tm	300 MPa for 48 hours 400 MPa for 48 hours 500 MPa for 48 hours
550 °C 823 °K = 0,48 Tm	200 MPa for 24 hours 300 MPa for 24 hours 400 MPa for 24 hours
600 °C 873 °K = 0,5 Tm	200 MPa for 5 hours 300 MPa for 5 hours 400 MPa for 5 hours 500 MPa up to failure

Since larger grains were more resistant to creep at the same temperatures, GG800-10 samples were tested up to failure or at least 48 hours.

Table 3.2. Creep experiments conducted on GG800-10 samples

Temperature	**Initial Stress and Duration**
500 °C 773 °K = 0,45 Tm	300 MPa for 65 hours 400 MPa for 65 hours 500 MPa for 48 hours
550 °C 823 °K = 0,48 Tm	300 MPa for 48 hours 400 MPa for 37 hours 500 MPa up to failure
600 °C 873 °K = 0,5 Tm	300 MPa up to failure 400 MPa up to failure 500 MPa up to failure

3.2.5.4. Thermal Cycling Under Stress with Subsequent Creep Experiment

Functional fatigue experimental setup was utilized to run thermal cycling under stress with subsequent creep experiments. Functional fatigue experiments reveal functional properties of the material; however functional cycles do not reveal the effect of high temperature on the creep behavior of the material. On the other hand, functional fatigue cycling also creates dislocations and damages which are the main reasons of irrecoverable strain. Creep experiment results do not contain the effect of cycling on high temperature behavior of the material. In order to understand the combined effect of creep and functional fatigue experiments, thermal cycling under stress with subsequent creep experiment was designed and applied.

Thermal cycling under stress with subsequent creep experiment was designed as a combination of alternating experiments. Each experiment was consisting 50 functional fatigue cycle between 600°C UCT and 200°C LCT and 3 hours of creep at 600°C. All experiments were conducted under constant load initially equivalent to 200 MPa. Sample was heated up to 600°C UCT and held for 15 minutes for thermal equilibrium of the grips. After 15 minutes, dead weight equivalent to 200 MPa was loaded. In the beginning of the first experiment, sample was subjected to creep deformation for 1 hour at 600°C in order to reveal the initial creep behavior of the sample. After 1 hour of creep deformation, 50 cycle of functional fatigue experiment was performed. Upon finishing 50th cycle, creep experiment was resumed for 2 hours. After 2 hours of creep at 600°C, sample was unloaded, cooled down to room temperature and re-sprayed with black paint. All experiments other than the first one were started with 50 cycle of functional fatigue experiment which was driven with 3 hours creep experiment at 600°C.

All experimental results were combined on a single strain-time plot. Creep deformations were compared in order to define how creep deformation was affected from functional fatigue cycles. All functional fatigue cycles were also compared using actuation strain and austenite strain values measured from every 10th cycle.

Optical Micrographs were presented to track surface damage between experiments. For comparison, micrographs of surface crack formation of functional fatigue experiments were also presented.

4. RESULTS AND DISCUSSION

This study was presented in four main parts: i) Thermal properties and optical microscopy of the heat treatments that was preformed ii) functional fatigue experiments and high temperature functional behavior of the NiTiHf alloy, iii) creep deformation of NiTiHf material at 600°C, 550°C, 500°C and 450°C, iiii) combined effects of functional fatigue and creep behavior.

4.1. Differential Scanning Calorimetry Results

Differential Scanning Calorimetry (DSC) plots in Figure 4.1 and 4.2 showed the transformation behavior of extruded and An550-3 50at%Ni-25at%Ti-25at%Hf samples under no load condition. The transformation temperatures (TTs) were drawn from DSC curves using tangent intersection method and were presented in Table 4.1 and Table 4.2. It can be realized from Table 4.1 and Table 4.2 that the TTs did not change noticeably. However, annealing led to observe sharp peaks in DSC curves.

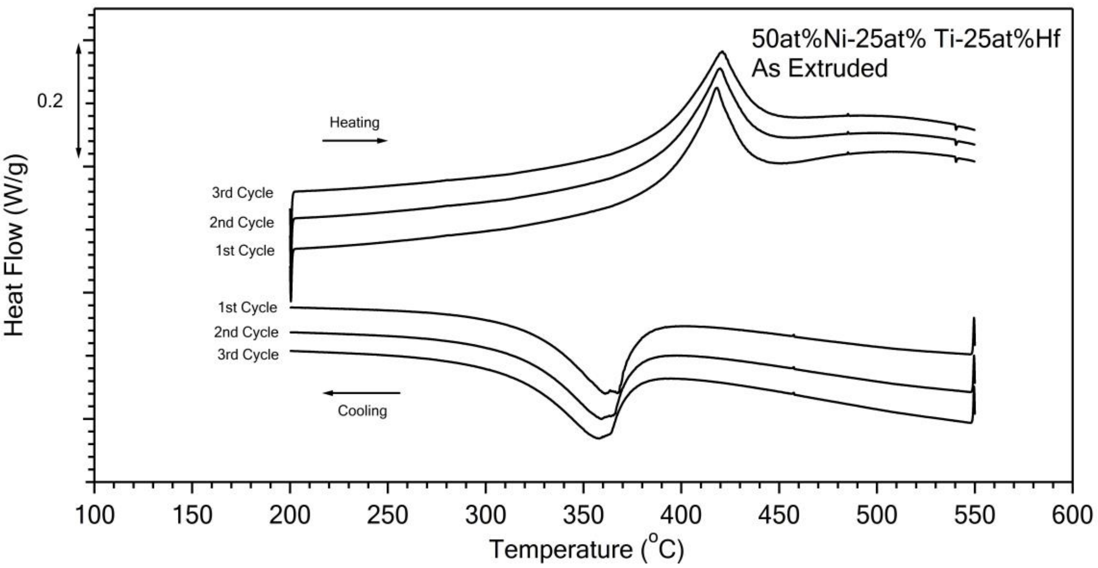

Figure 4.1. DSC results of Extruded sample [68].

Table 4.1. Summary of the transformation temperatures of Extruded sample which were drawn from DSC curves [68].

Temperatures (°C)	**1^{st} Cycle**	**2^{nd} Cycle**	**3^{rd} Cycle**
A_f	435	435	438
A_s	388	386	386
M_s	379	376	374
M_f	320	316	314

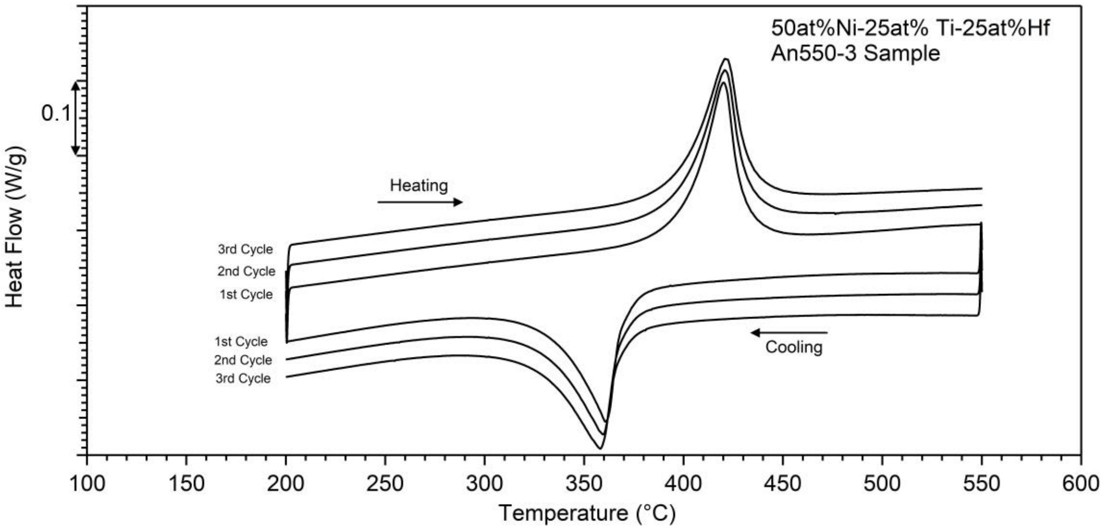

Figure 4.2. DSC results of An550-3 sample [68].

Table 4.2. Summary of the transformation temperatures of An550-3 sample which were drawn from DSC curves [68].

Temperatures (°C)	**1^{st} Cycle**	**2^{nd} Cycle**	**3^{rd} Cycle**
A_f	432	433	434
A_s	399	398	398
M_s	371	369	368
M_f	330	327	324

DSC results of GG800-10 sample was plotted in Figure 4.3. While annealing heat treatment did not change TTs with respect to the extruded condition, M_s temperatures as high as 20°C increased after the grain growth heat treatment of GG800-10 samples, as it was presented in Table 4.3. M_s temperatures were observed to be decreasing with increased dislocation density in the matrix [98,99]. Thus increase in M_s temperatures proved that heat treatment for grain growth led to the annihilation of more dislocation than of annealing at 550°C for 3 hours.

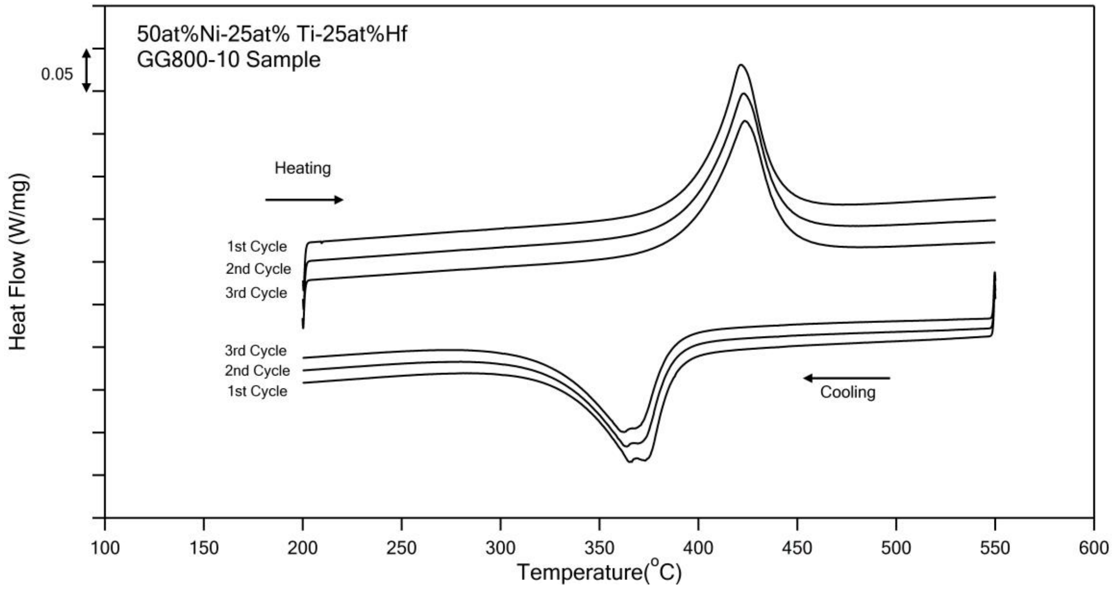

Figure 4.3. DSC results of GG800-10 samples

Furthermore, GG800-10 sample also presented high thermal stability between DSC cycles with increased TTs. Since thermal stability was known to increase with increasing strength and usually achieved in NiTi alloys with grain refinement [100], it was assumed to be the result of high strength that was provided with Hafnium addition to NiTi.

Table 4.3. Summary of the transformation temperatures of GG800-10 sample which were drawn from DSC curves

Temperatures (°C)	**1st Cycle**	**2nd Cycle**	**3rd Cycle**
A_f	441	444	445
A_s	398	394	394
M_s	389	388	387
M_f	330	329	321

4.2. Optical Microscopy Micrographs of An550-3 and GG800-10 Heat Treatments

Optical microscopy micrographs were taken immediately after 1 minute etching with H_2O:HNO_3:NF acid solution with a ratio of 85:12:3. All micrographs were taken from the cross section of rod shaped with 12 mm diameter materials that were annealed at 550°C for 3 hours (An550-3) and grain growth heat treated at 800°C for 10 hours (GG800-10).

4.2.1. Optical Microscopy Micrographs of An550-3 Samples

Flow lines from the extrusion were visible for 50x and 100x magnifications as it can be seen in Figure 4.4 and Figure 4.5.

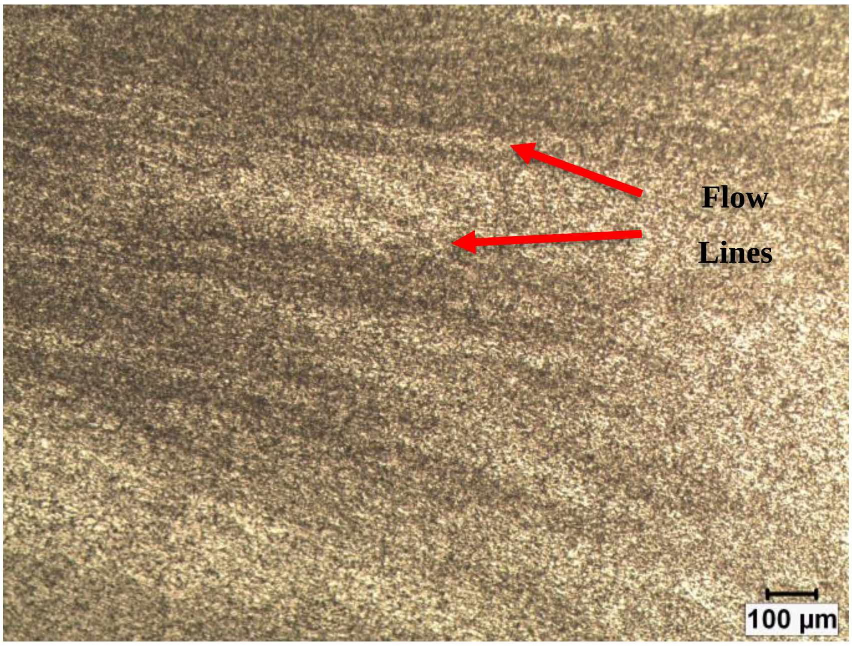

Figure 4.4. An550-3 sample under 50x magnification

Extrusion process at 900°C with an area reduction of 4:1 led to the formation of flow lines which were indicated with red arrows in Figure 4.4 and Figure 4.5. If the image shown in Figure 4.5 was magnified, bubble like secondary particles that are decorating the grain boundaries were revealed that can be seen clearly in Figure 4.6 with a magnification of 500x.

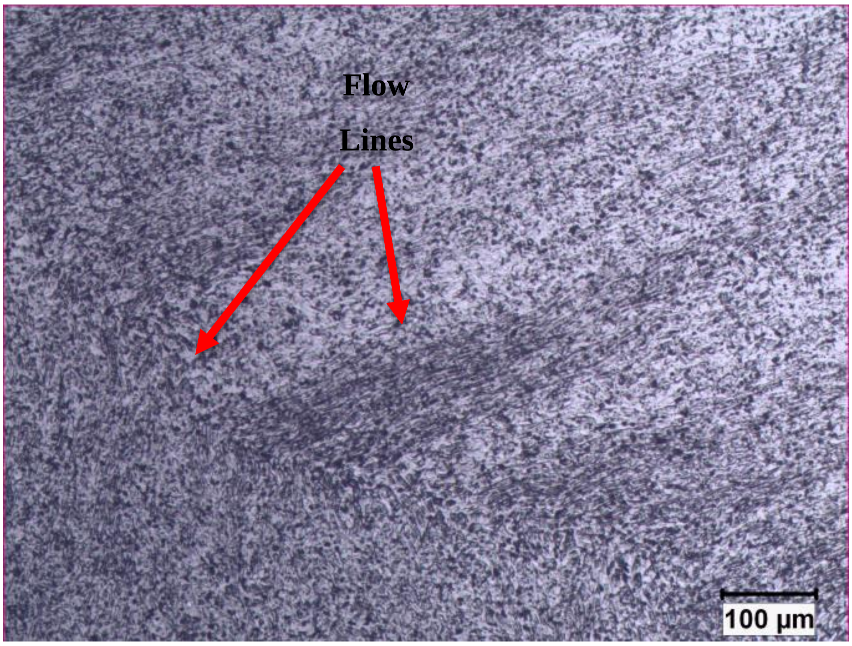

Figure 4.5. An550-3 sample under 100x magnification

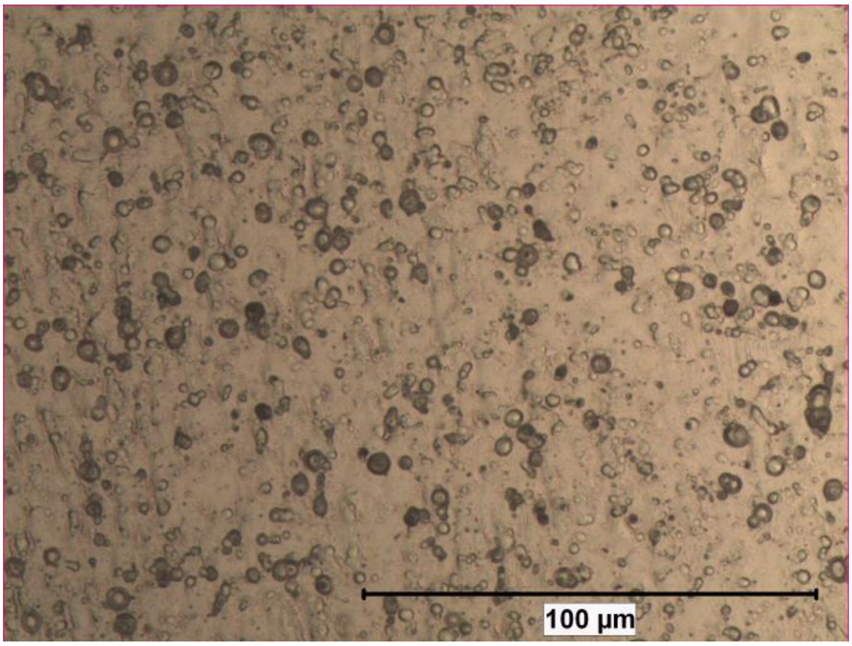

Figure 4.6. An550-3 sample under 500x magnification

Although bubble like secondary particles were more distinct with 500x magnification, it was not possible to pinpoint the type of the particles with optical microscopy. In order to identify the formations, sample was investigated with SEM. It was found and shown in Figure 4.7 that, every distinct bubble like formation had white particles which were emphasized with red arrows.

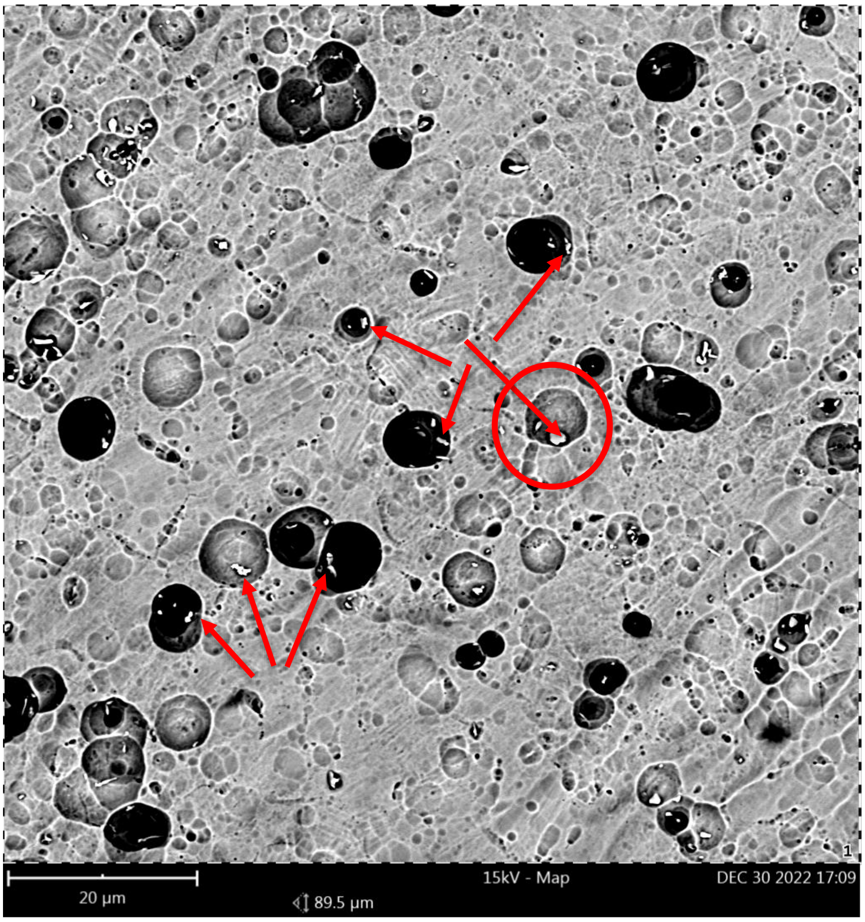

Figure 4.7. SEM image of microstructure

EDS analysis revealed that white particles are hafnium oxides. EDS mapping of red circle in Figure 4.7 was presented in Figure 4.8. However, around oxide particles, every element has lower concentrations than that of the surrounding areas. As a result, bubble like formations were concluded to be etching pits around hafnium oxides.

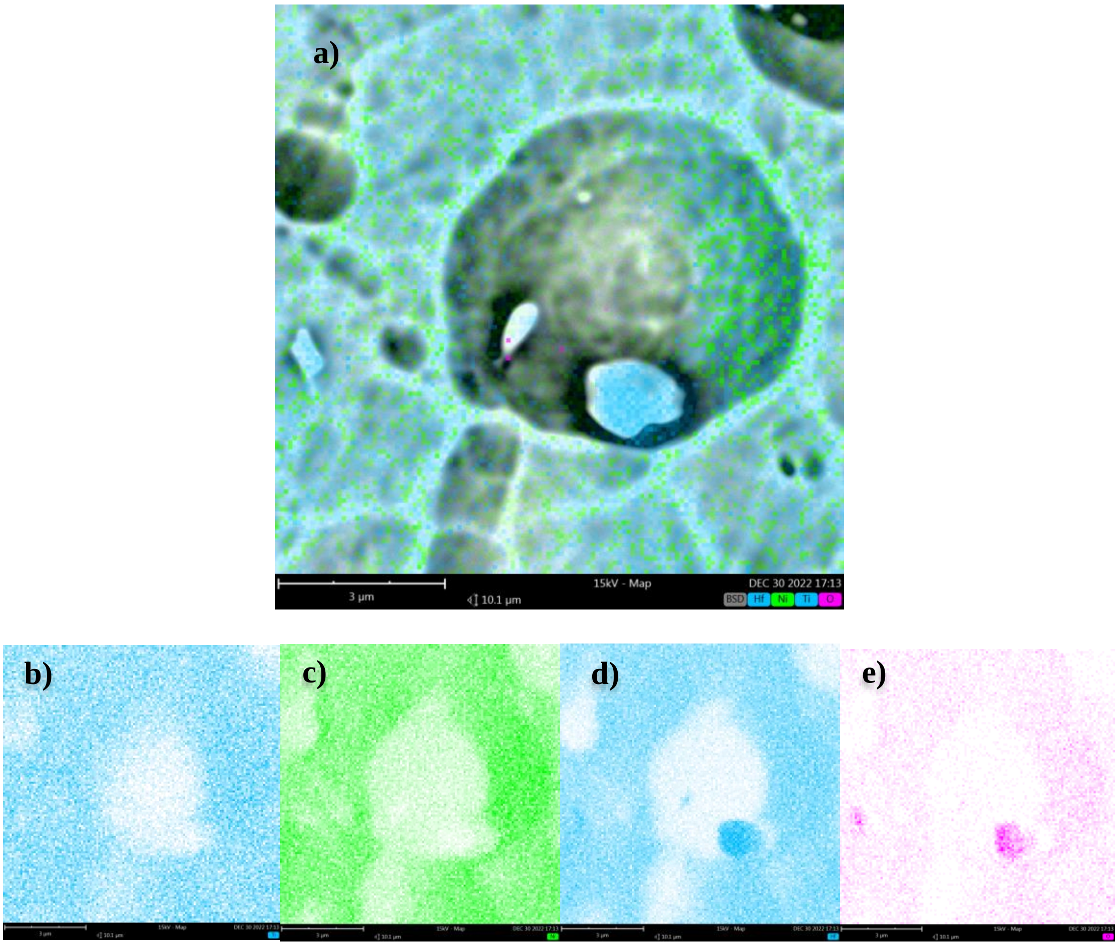

Figure 4.8. EDS Mapping analysis of formations a) Presence of all selected elements b) Titanium presence c) Nickel presence d) Hafnium presence e) Oxygen presence

Oxides that formed during casting of the alloy, decorate the grain boundaries. Hence grain structure could be identified following etch pits at higher magnifications. Elliptical shapes between the etch pits in Figure 4.9 (with 1000x magnification) were found and the diameter of the elliptical forms were measured as 15-17 micron. Smaller forms which were about 10 microns wide, were also shown and they were considered to be similar to recrystallized subgrain structures that were shown for different metal alloys in the literature [101].

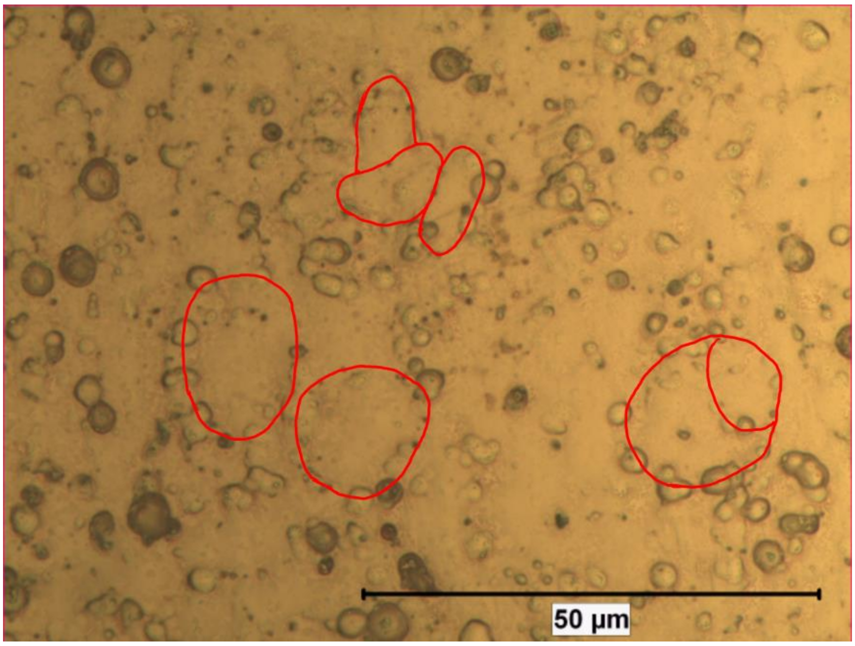

Figure 4.9. An550-3 sample under 1000x magnification

4.2.2. Optical Microscopy Micrographs of GG800-10 Samples

Figure 4.10. GG800-10 sample under 50x magnification

GG800-10 sample also showed flow line structures from the extrusion process as it can be observed in Figure 4.10. However, higher temperature and longer annealing time created less dense formations of flow lines as it can be seen in Figure 4.11.

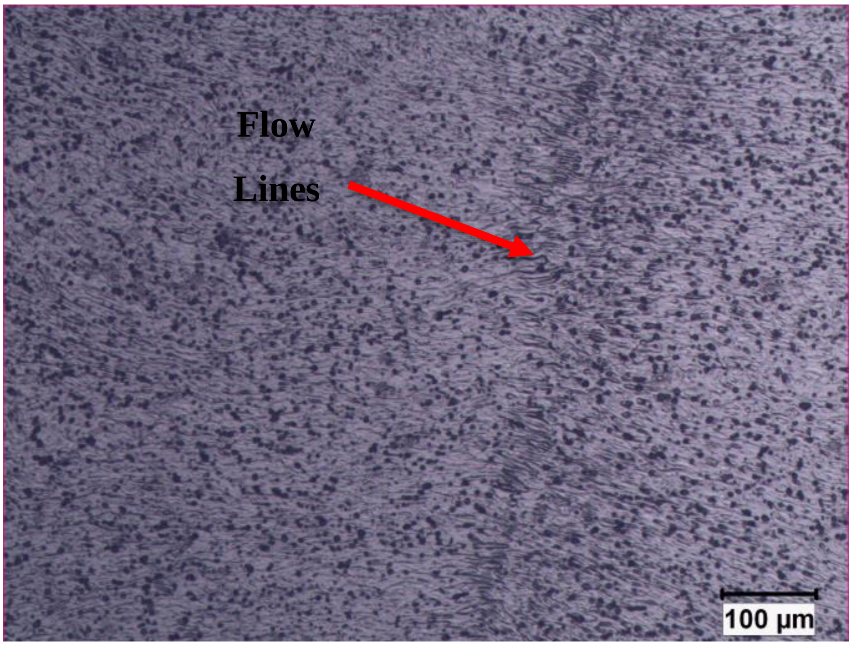

Figure 4.11. GG800-10 sample under 100x magnification

With the 500x magnification, hollow space around etch pits became more visible and grains can be identified using patterns of etch pits. In Figure 4.12, the red circles were drawn using the traces of the etch pits and size of the circles were measured as 25 and 40 microns. Also block like structures were noticed between etch pits, which were martensitic plates. Martensitic structure appeared since the grain growth heat treatment at relatively high temperature for a long period of time led a high stress relief.

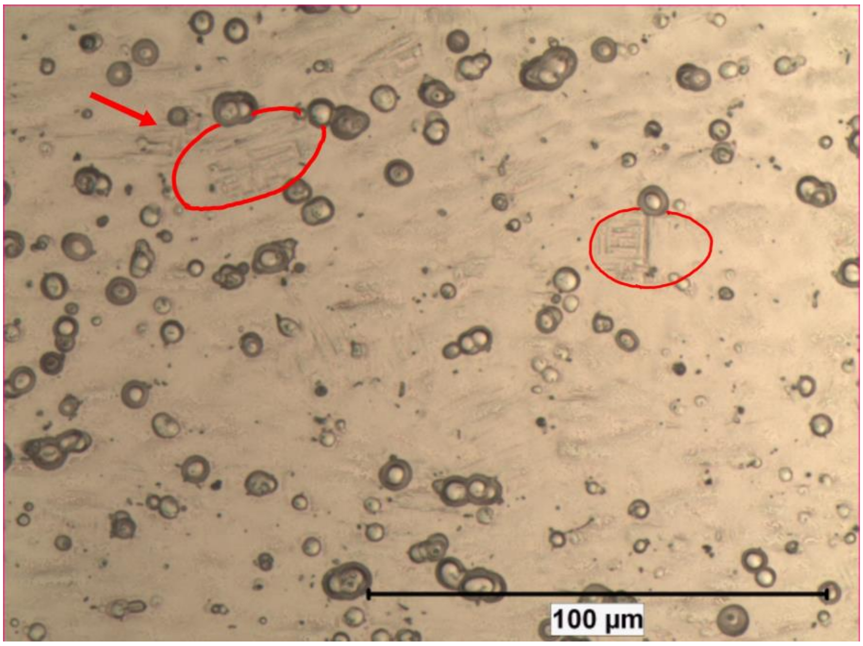

Figure 4.12. GG800-10 sample under 500x magnification

It should be noticed that block structure which was pointed with red arrow in Figure 4.12, had a fish bone like formation. Grain size measurements in Figure 4.13 was 30-40 microns so it was concluded that, assuming that the etch pits due to Hafnium Oxides were located at grain boundaries, average grain size of GG800-10 samples should not be less than 30 microns. However, grain size measurement was not accurate since the optical microscopy did not reveal exact results. It was predicted that GG800-10 samples had larger grains. Additionally, it is worth to mention that the exact values of grain sizes can be found via in-situ Transmission Electron Microscope (TEM) with hot stage attachment. However, the hot stage should heat the sample above A_f temperature of the alloy which was used in this study and A_f temperatures of the alloy in any heat treatment condition is above 400°C and there is no hot stage that can heat the sample to this temperature.

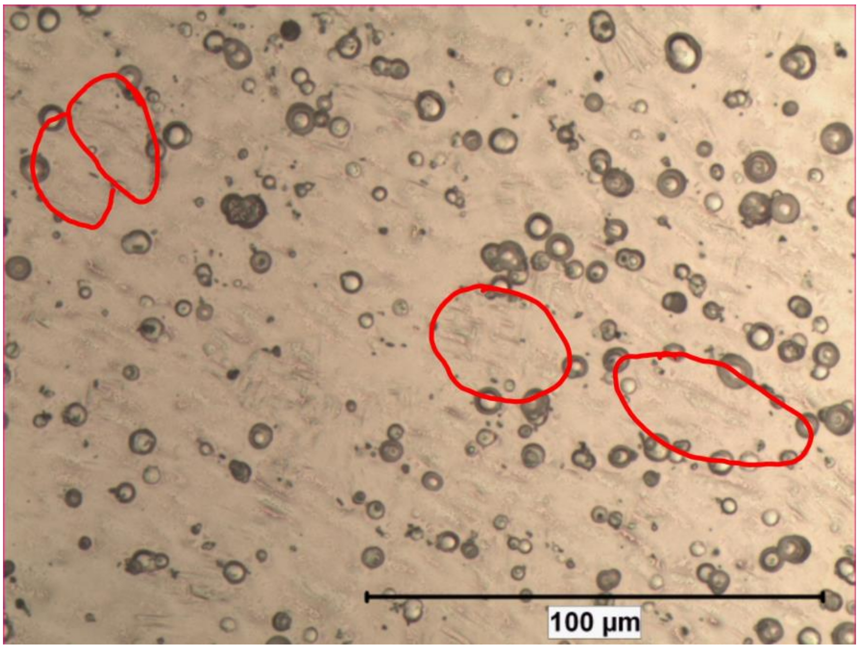

Figure 4.13. GG800-10 sample under 500x magnification

4.3. Functional Fatigue Behavior of 50at%Ni- 25at%Ti – 25at%Hf Material

Functional fatigue experiments were conducted on as extruded, annealed and grain growth heat treated samples. Results of the functional behavior of the alloy and the discussion of the results will be given in three different section below. Firstly, functional fatigue experimental results will be presented with the plots of all strain vs temperature data. Then the austenite strain, actuation strain, irrecoverable strain, thermal hysteresis and transformation temperatures that were drawn from full plots, as it was explained in the experimental procedures, will be presented in the following sections.

4.3.1. Functional Fatigue Experimental Results

Functional fatigue results were plotted in a way to show the all thermal hysteresis cycles that were gathered from the experiments conducted under 200 MPa. 1st, 150th and the last cycles were highlighted to present the evolution of cyclic performance of the samples. In later sections starting from 4.3.2 to 4.3.5 strain formations that were derived from the cycle plots as it was explained in experimental section also presented in order to further investigate the functional fatigue performance of the NiTiHf functional fatigue samples.

Functional fatigue experiments on as extruded samples were plotted in Figures 4.14 and 4.15.

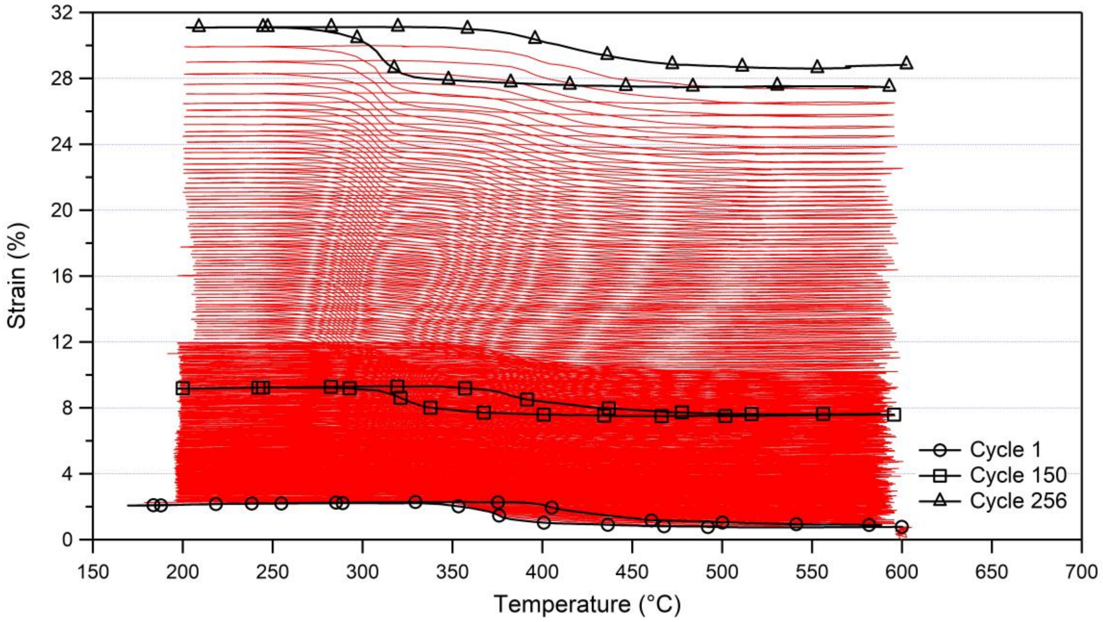

Figure 4.14. Functional fatigue experiment results of Extruded Sample 1

Extruded sample 1 had failed due to black paint as it was explained in the experimental procedure section. It is worth to recall that the black paint is necessary to measure the temperature of the sample instantly by infrared thermometer and if the black paint is peeled off from the surface the temperature cannot be measured accurately and the heating cannot be controlled. Therefore, the sample was heated to a temperature much higher than 600°C UCT. Transformation temperatures (TTs) decreased with the number of cycles starting from the first cycle to 150th cycle as it is seen in Figure 4.14. Decreasing TTs with visible increase in irrecoverable strain indicates that temperature sensor was not measuring correct temperature so that UCT was set to higher temperatures. Figure 4.15 demonstrated the functional fatigue results of Extruded Sample 2, which was cycled for

100 cycles by setting 550°C UCT and the UCT was increased to 600°C UCT. Extruded sample 2 performed more number of cycles than that of Extruded Sample 1.

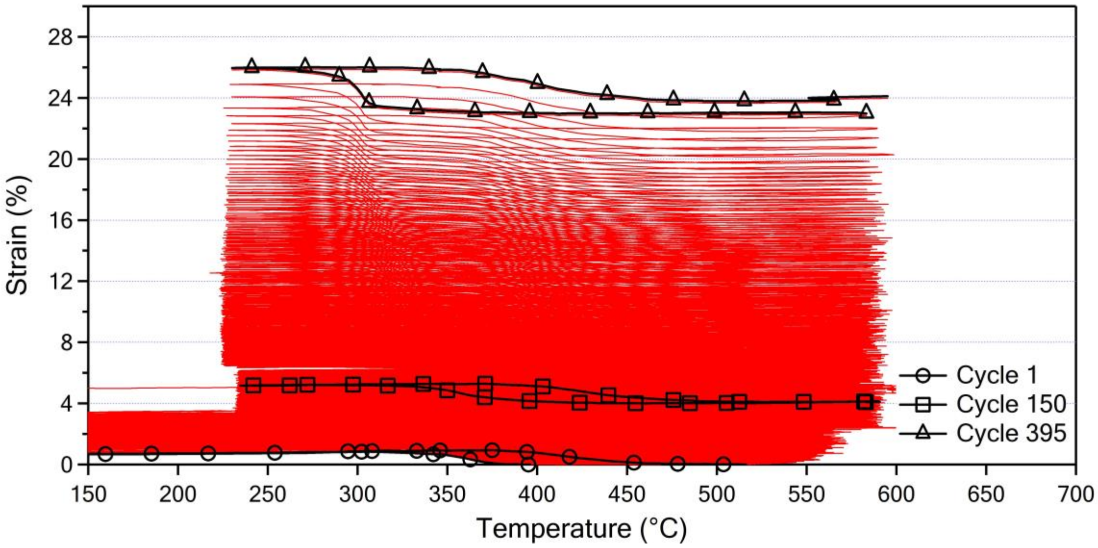

Figure 4.15. Functional fatigue experiment results of Extruded Sample 2

Extruded sample 2 performed 395 cycles before failure. Gradual increase in irrecoverable strain was also noticeable when Figure 4.15 was compared with Figure 4.14. As explained in Heat Treatments section, samples were subjected to annealing heat treatment at 550°C temperature for 3 hours. An550-3 sample 1 cycled up to 252 cycle and full experiment data were presented in Figure 4.16.

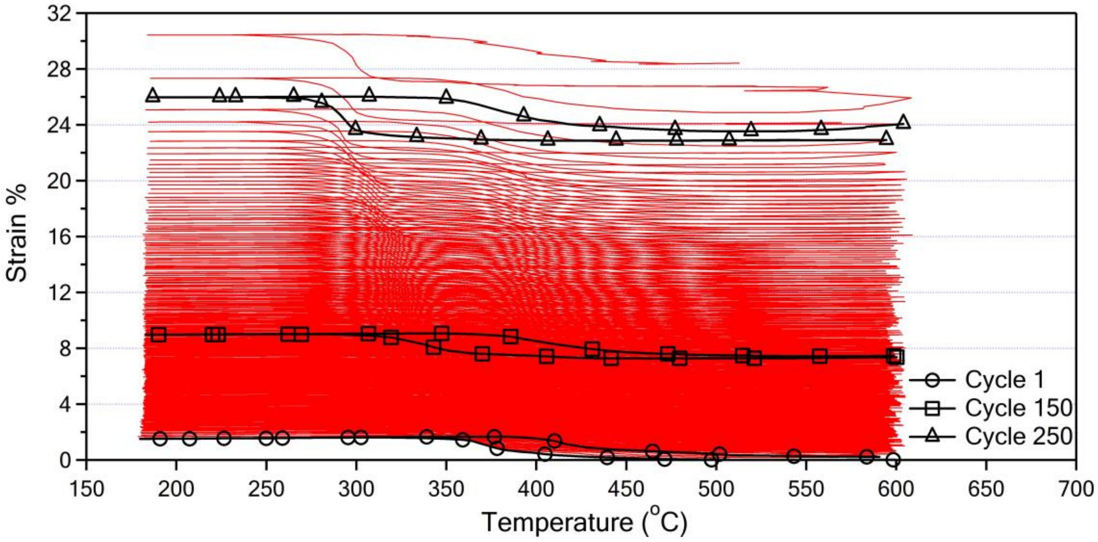

Figure 4.16. Functional fatigue experiment results of An550-3 Sample 1

Gradual increase in irrecoverable strain and decrease in transformation can be easily noticed from the experimental data. Black paint failure was also the main factor in the failure of An550-3 Sample 2. Functional fatigue life was only 136 cycles and irrecoverable strains started to increase tremendously before the 100th cycle as can be seen in Figure 4.17.

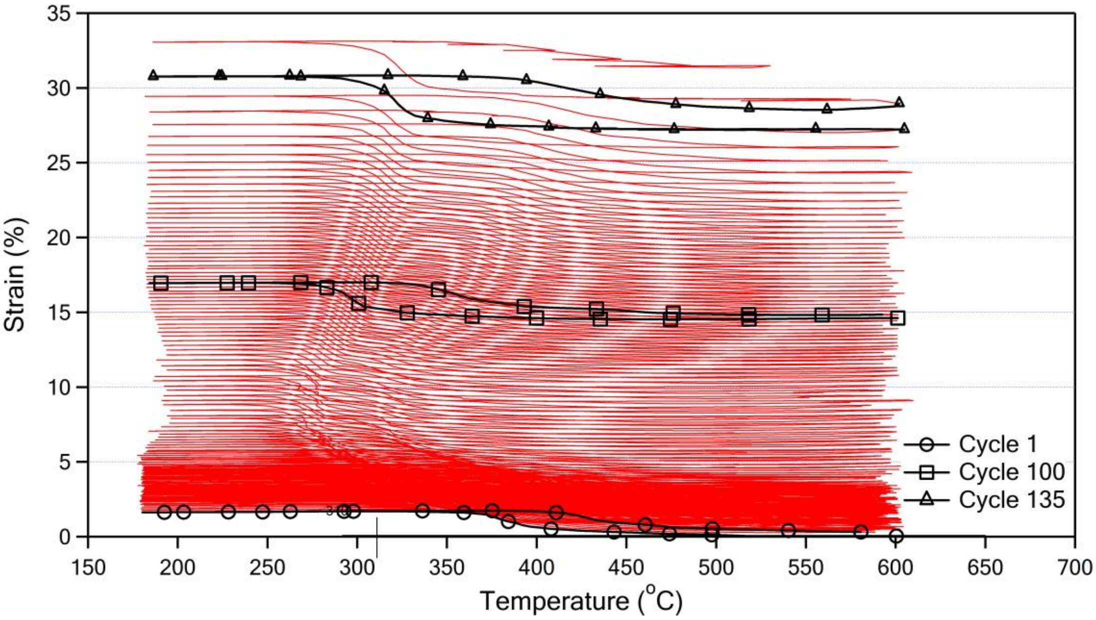

Figure 4.17. Functional fatigue experiment results of An550-3 Sample 2

Experimental results of An550-3 Sample 3 were presented in Figure 4.18 and the 3rd annealed sample performed 436 cycles which was achieved as the highest functional fatigue life from all samples. Transformation temperatures were slightly changed throughout the number of cycles.

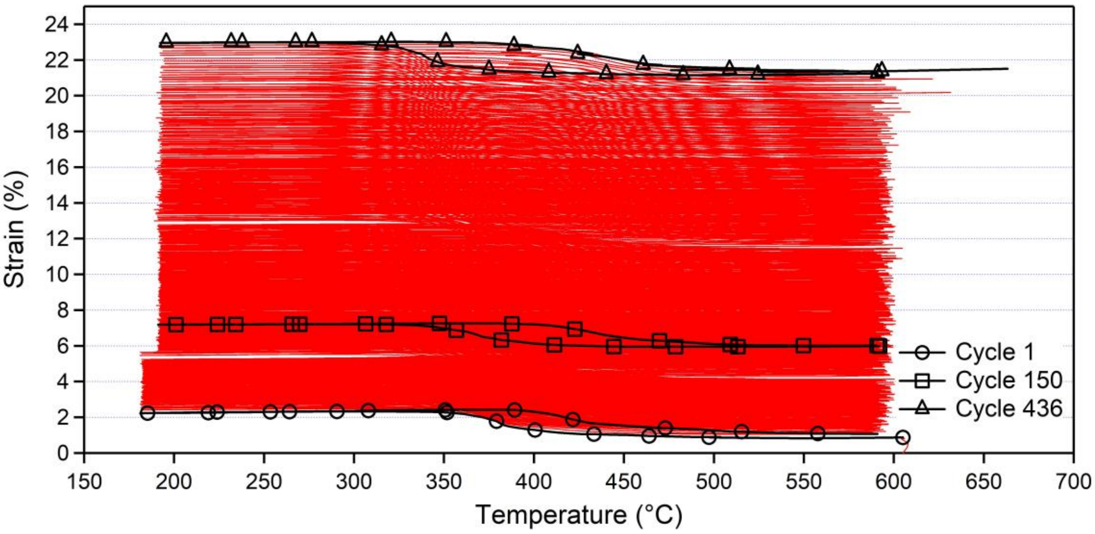

Figure 4.18. Functional fatigue experiment results of An550-3 Sample 3

Functional fatigue experiment of An550-3 Sample 3 did not terminate via failure. At the end of cycle 436, sample became too thin to maintain the temperature at 600°C. As a result, sample was heated above 650°C as it can be seen at the end of cycle 436 in Figure 4.8. 50°C of fluctuation in the temperature was the main reason for termination of the experiment.

Single functional fatigue experiment was performed on grain growth heat treated sample and results of the experiment data were presented in Figure 4.19. Grain growth heat treated sample coded as GG800-10 had a functional fatigue life of 335 cycles. Gradual increase in irrecoverable strain and minimal changes in TTs also indicated that functional fatigue experiment was conducted adequately.

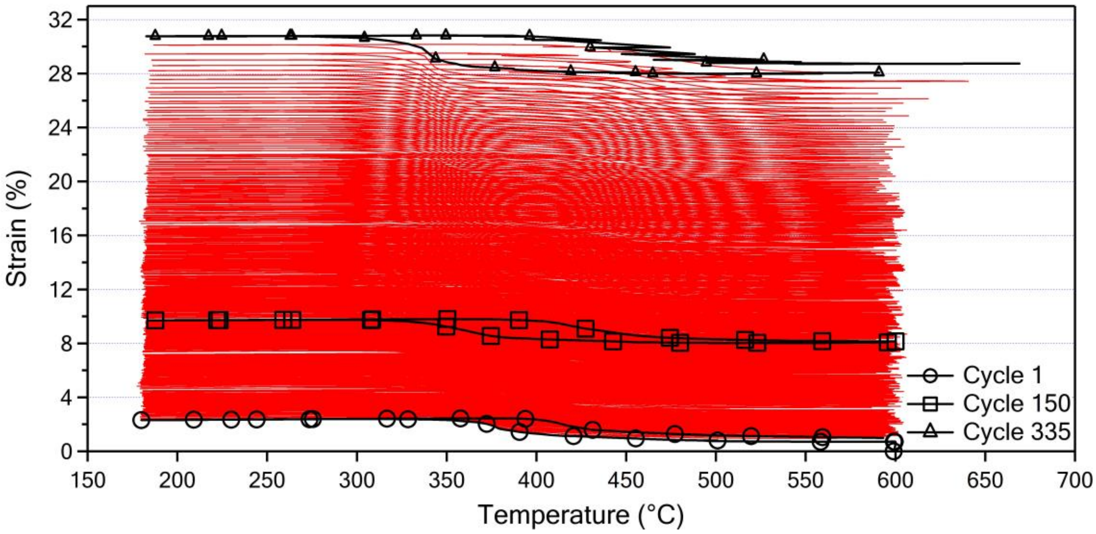

Figure 4.19. Functional fatigue experiment results of GG800-10 Sample

Up to now strain vs temperatures data of the functional fatigue experiments were presented, however these data did not reveal enough information about actuation and damage accumulation characteristics of the samples. In the next chapters through 4.3.2 to 4.3.5, actuation strain, austenite strain, irrecoverable strain, hysteresis and transformation temperature values of selected cycles from each experiment will be presented.

4.3.2. Comparison of Actuation Strain Values

Actuation strain in a specific cycle provides information on forward and reverse transformation and transforming volume of the material. Transforming volume decreases via damage accumulation with the increase in irrecoverable strain values. On the other hand, the load bearing area of the sample reduced with the crack formation and propagation which leads to an increase in stress on the transforming volume. Hence, detwinned martensite volume increases under higher stress. Increase in detwinned martensite volume would express itself as an increase in actuation strain.

Actuation strain data taken from every 25 cycle from the experiments plotted in Figure 4.20. Actuation strain values in the beginning of the experiments were the ones that the samples had not been damaged yet. Extruded_S1 started with the actuation strain values of 1.4% and Extruded_S2 started with the values of 0.9% actuation strain. As a result, the results of the extruded samples were not consistent in terms of actuation strain due to the inhomogeneous dislocation and internal stress formation during extrusion process. This behavior was widely explained by Akin et al. in a previous publication [90].

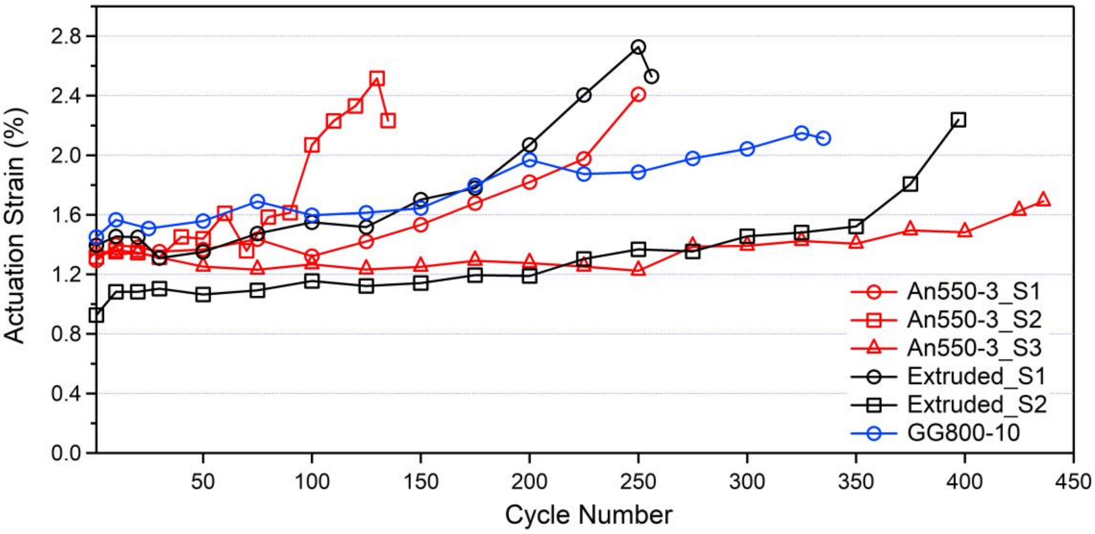

Figure 4.20. Actuation Strain of all samples which were thermally cycled throughout the functional fatigue experiments

Actuation strain data of all An550-3 samples were started between 1.3-1.4% values. However, An550-3_S2 displayed an increase in actuation strain up to 1.6% strain at around cycle 60. After cycle 70, actuation strain of An550-3_S2 steadily increased up to 2.4% and failure occurred. An550-3_S2 was a perfect example of black paint failure. On the other hand, An550-3_S1 and An550-3_S3 almost showed steady state increase in actuation strain values. Actuation strain of An550-3_S1 started to increase with the 125th cycle. Increase in actuation strain for An550-3_S1 was fairly linear up to 225th cycle to a value of 2%. An550-3_S3 performed the highest functional fatigue life of 436th cycle with a 1.6% actuation strain at the end of the experiment. It is also worth to mention that the actuation strain values of this sample was observed to be almost constant up to 250th cycle.

In Figure 4.21, best experiments for each condition were compared in terms of actuation strain. Data trends were shown with 2nd degree polynomial fit using the data points up to rapid increase in actuation strain. Root mean square error (RMSE) of the polynomials were also included in order to show how well the polynomials fit to the acquired data.

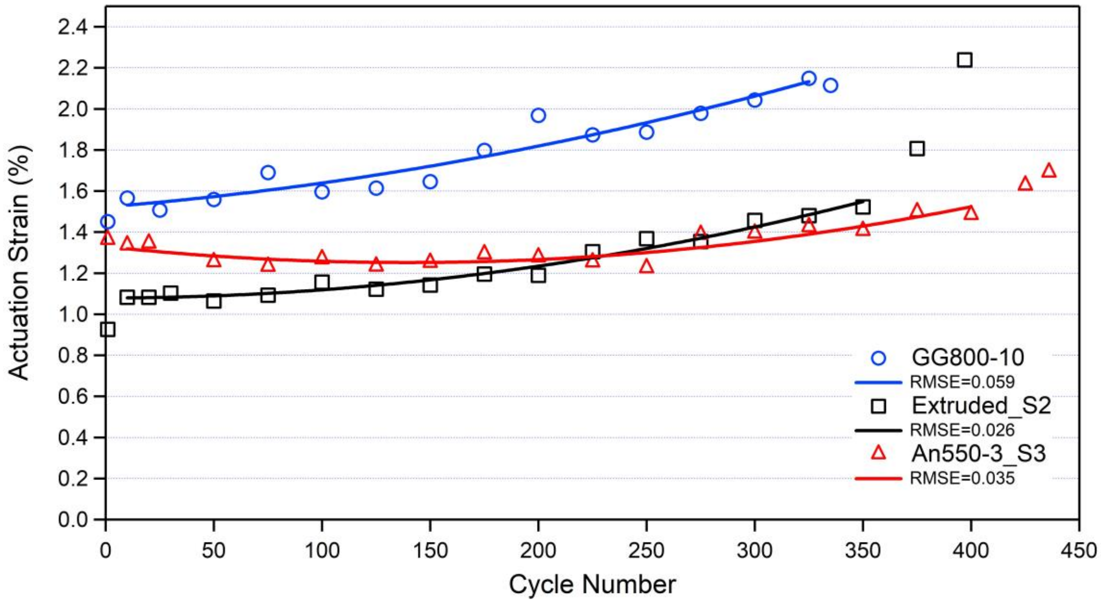

Figure 4.21. Actuation Strain of Extruded, An550-3 and GG800-10 specimens

GG800-10 yielded a higher actuation strain at the beginning of the experiment and actuation strains increased linearly throughout the experiment just opposite to An550-3_S3 which had a constant actuation strain up to 300th cycle. This behavior can be explained with lower dislocation density of the GG800-10 sample. Every cycle induced more dislocations to GG800-10 by phase transformation than that of An550-3_S3. Thus, damage formation was more rapid than that of the other 2 experiments.

Extruded_S2 sample showed a lower starting actuation strain and the actuation strain values were stable up to 150th cycle. After 150th cycle, actuation strain started to increase up to 2.2% before failure. An550-3_S3 showed constant actuation strain up to 275th cycle and afterwards gradually increasing actuation strain indicated the initiation of crack formation started to affect actuation performance. It is important to note that, cracks open and close with the phase transformation and this leads to observe an increase in actuation strain values [9,102].

4.3.3. Comparison of Austenite Strain Values

Austenite Strain is the measured as the total strain at the end of heating cycles. As explained in experimental methods chapter, strain difference between the end of heating and beginning of the cooling cycles is termed as irrecoverable strain. Since every cycle starts from the end of the previous cycle, austenite strain is the accumulation of irrecoverable strain throughout the experiment. Irrecoverable strain values include the effect of plastic deformation and decrease in transforming volume. Decrease in transformation volume also associated with dislocation formation. As a result, austenite strain can be defined as plastic deformation rate.

In Figure 4.22, austenite strain values that were gathered from all experiments were plotted. It is clear that An550-3_S2 definitely failed prematurely. An550-3_S3 and Extruded_S2 samples showed the lowest rate of deformation.

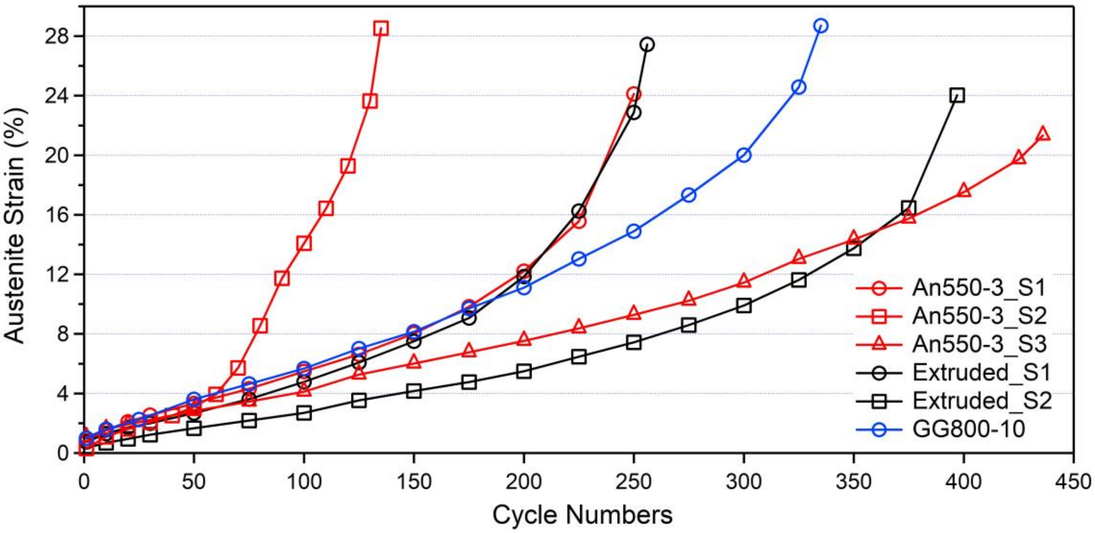

Figure 4.22. Austenite Strain values that were gathered from all functional fatigue experiments

However, it should be stated that austenite strains of GG800-10 and An550-3_S1 samples were nearly identical up to 175th cycle. This could be explained with the increased actuation strain of GG800-10 sample, which resulted increased damage accumulation due to higher transforming volume. In Figure 4.23 austenite strain values of the 3 samples were compared using data and polynomials that were fitted to the data were also presented and RMSE values were given.

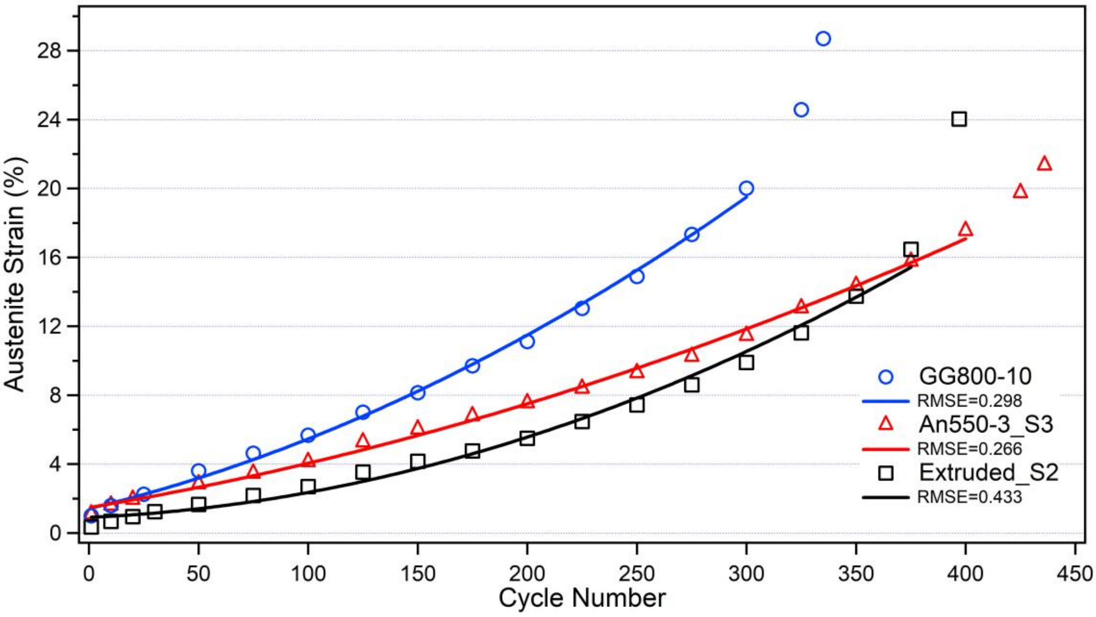

Figure 4.23. Austenite Strain comparison for selected samples

Polynomials showed that the highest slope belonged to GG800-10. Highest slope represents the higher damage accumulation rate. Higher actuation strain values of GG800-10 sample related with the higher damage accumulation per cycle is very much in correlation with literature. An550-3_S3 had higher actuation strain than that of Extruded_S2, however damage accumulation rate was lower. An550-3_S3 showed the longest linear increase in austenite strain up to 275th cycle.

Lower actuation strain of Extruded_S2 indicated lower damage formation, thus austenite strain was fairly linear up to 250th cycle. However, sample showed higher austenite strain increase rate after 250th cycle. Therefore, it should be stated that after a certain point, damage accumulated rapidly.

For the first 3-4 data points all samples showed a decreasing rate in the increase of the austenite strain which resembles the primary creep formation in the creep experiments. This behavior can be explained with the hardening of the sample due to dislocation generation during cycling. Overall formation of the austenite strain can also be compared with creep deformation strain rates which will be presented in section 4.6.

4.3.4. Comparison of Irrecoverable Strain Values

Irrecoverable strain values were plotted in Figure 4.24 in order to emphasis the damage formation of each cycle for different samples. It should be noticed that irrecoverable strain values of An550-3_S2 increased up to 0.2-0.3% after 50th cycle. Irrecoverable strain data of An550-3_S2 between cycles 50 to 100 showed an increase in the temperature exceeding the set UCT due to black paint failure which led to a decrease in strength of the alloy and increase in the accumulated damage.

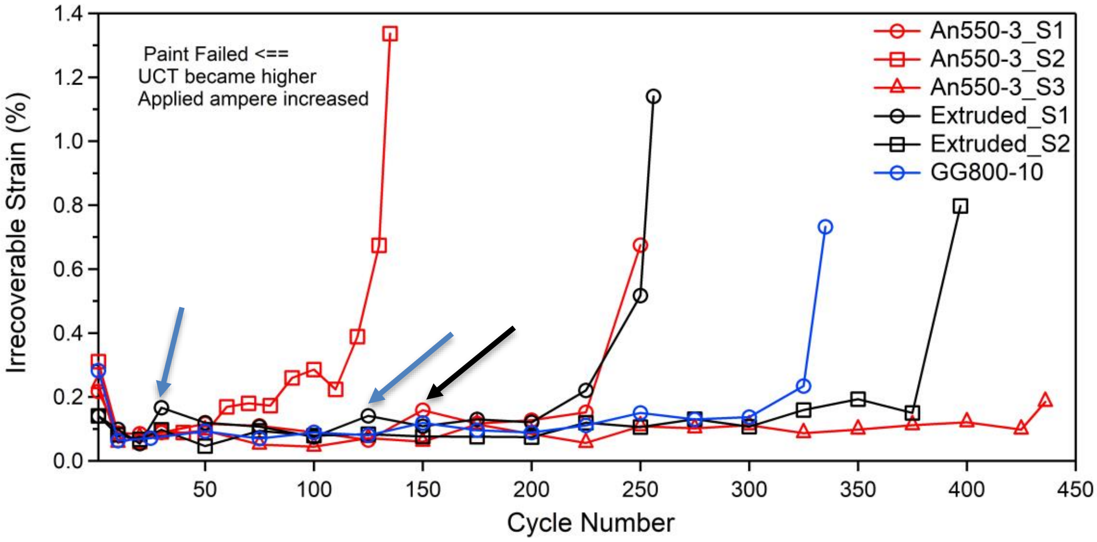

Figure 4.24. Irrecoverable Strain comparison for all functional fatigue experiments

Similar temporary increase in irrecoverable strain, was shown with blue arrows in Figure 4.24, was also noticed for Extruded_S1 in cycles 30 and 125. Extruded_S1 also showed a decrease in TTs and it can be seen in Figure 4.14. Additionally, irrecoverable strain value of An550-3_S1 increased in 150th cycle, which was pointed with black arrow in Figure 4.24, however it was not clear if the increased irrecoverable strain was due to paint failure.

Three selected samples did not demonstrate sudden increase in irrecoverable strain therefore, it was accepted that there was no encountered problem such as the peeling of the black paint from the surface during the experiment. For this reason, irrecoverable strain values that were gathered from three experiments were plotted in Figure 4.25. Second degree polynomials were also plotted in order to show the data trend and RMSE values were shown in plot.

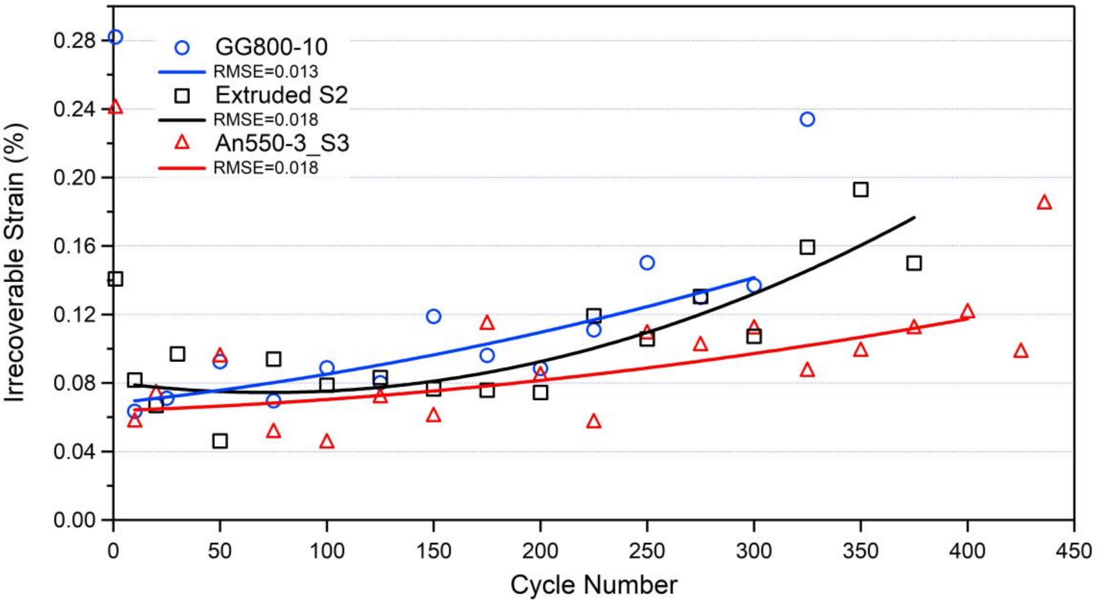

Figure 4.25. Irrecoverable Strain comparison for selected specimens

It should be noticed that irrecoverable strain values that were drawn from the first cycles for both heat treated samples were nearly twice the irrecoverable strain value of the first cycle of the Extruded_S2. Annealing and grain growth heat treatments which were performed for dislocation annihilation (stress relieving) and grain growth, decreased the strength of the alloy and thus dislocation generation became easier during thermal cycling with phase transformation. GG800-10 sample, which was containing larger grain structure and lower dislocation density, produced irrecoverable strains with a higher rate than that of other two samples.

Additionally, increasing rate of irrecoverable strains of An550-3_S3 was found to be lower since the increase in irrecoverable strain that was shown, had the lowest slope in Figure 4.25. On the other hand, Extruded_S2 showed irrecoverable strain values between 0.04% and 0.1% up to 200th cycle and values were found to be pretty stable. This behavior was explained with higher dislocation density of the extruded sample due to the extrusion process which inhibited new dislocation formation during thermal cycling that led to the formation of cracks.

4.3.5. Comparison of Hysteresis and Transformation Temperatures

Thermal hysteresis values with the number of cycles that were drawn from all functional fatigue experiments were presented in Figure 4.26.

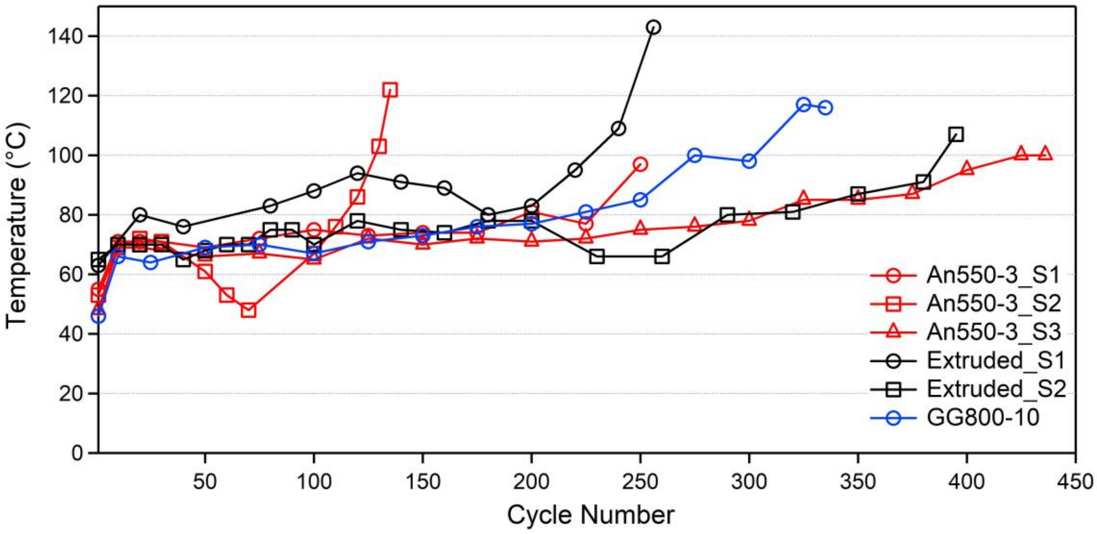

Figure 4.26. Hysteresis comparison for all functional fatigue experiments

An550-3_S2 showed a decrease and then a sharp increase in hysteresis between 30th and 130th cycles. Similar decrease and sharp increase can also be noticed for Extrude_S1 between 100th and 250th cycles. It has been already explained that both An550-3_S2 and Extruded_S1 exposed to very high temperatures due to black paint failure. Hence it should be concluded that abnormal decrease and increase in hysteresis indicates overheating hence increased damage formation occurred during experiments.

While extruded samples showed thermal hysteresis over than 60°C, all An550-3 samples and GG800-10 sample showed lower hysteresis which were around 45-55°C at the beginning of the functional fatigue experiments. As a result, it can be deduced that higher dislocation density of the extruded samples led to observe larger thermal hysteresis.

Hysteresis plots of selected three samples were presented in Figure 4.27. Second degree polynomials were also plotted and RMSE values were given in the Figure 4.27. In the first cycle, hysteresis of Extruded_S2 was around 65°C and the hysteresis values became stable at around 70°C to 80°C and the stable values were observed up to 200th cycle. Both An550-3_S3 and GG800-10 samples showed thermal hysteresis values lower than 50°C in the first cycle and then hysteresis values increased suddenly to 65°C during the first 25 cycles. All three samples had similar hysteresis values up to 200th cycle.

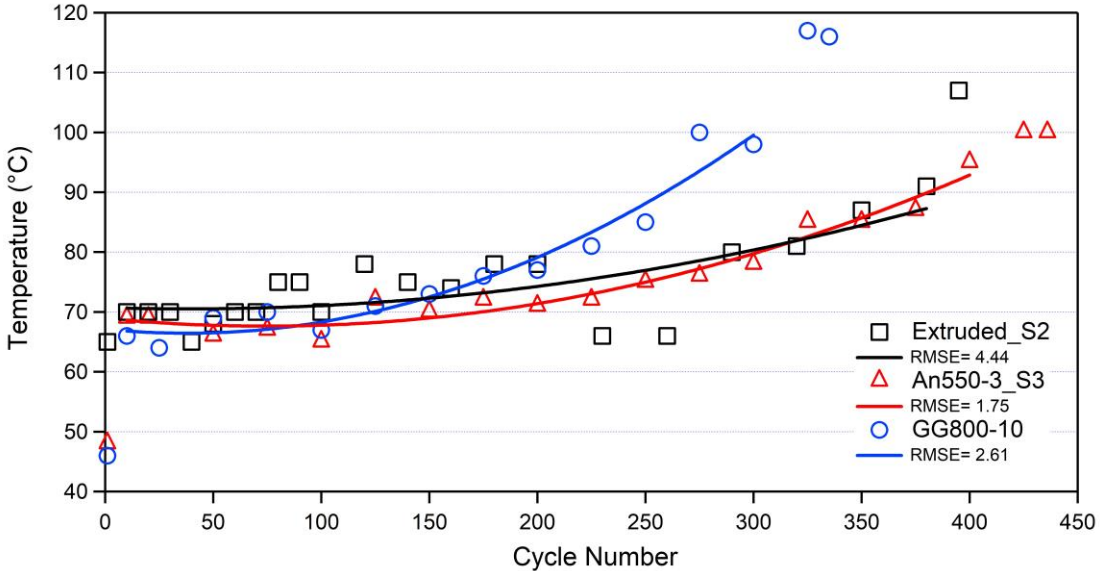

Figure 4.27. Hysteresis comparison for three selected experiments

Thermal hysteresis plots revealed that, both heat treatments decreased dislocation density of the samples and then thermal cycling enabled dislocation formation in about 10 cycles. GG800-10 specimen had higher rate of increase in thermal hysteresis than that of both An550-3_S3 and Extruded_S2 samples.

Furthermore, all samples either failed or came close to failure when the hysteresis value reaches 100°C. Increase in thermal hysteresis with functional fatigue cycles could be explained with the release of elastic energy. Elastic energy that is stored in martensite phase lowers the energy requirement for reverse transformation [26]. Dislocation generation and slip decreased the stored elastic energy and increased the energy requirement for reverse transformation which led to a gradual increase in thermal hysteresis up to failure. Since all samples failed when the thermal hysteresis values reached above 100°C, it can be claimed that grain size and heat treatment had limited effect on failure. The dislocation generation rate per cycle actually changed and this led to the failure of the samples.

Austenite Finish (A_f) and Martensite Start (M_s) temperatures of the selected experiments with the number of cycles were plotted in Figure 4.28. It can be stated that, M_s temperatures decreased and A_f temperatures increased with the accumulation of dislocations, thus, more overcooling and overheating became necessary for the phase transformation.

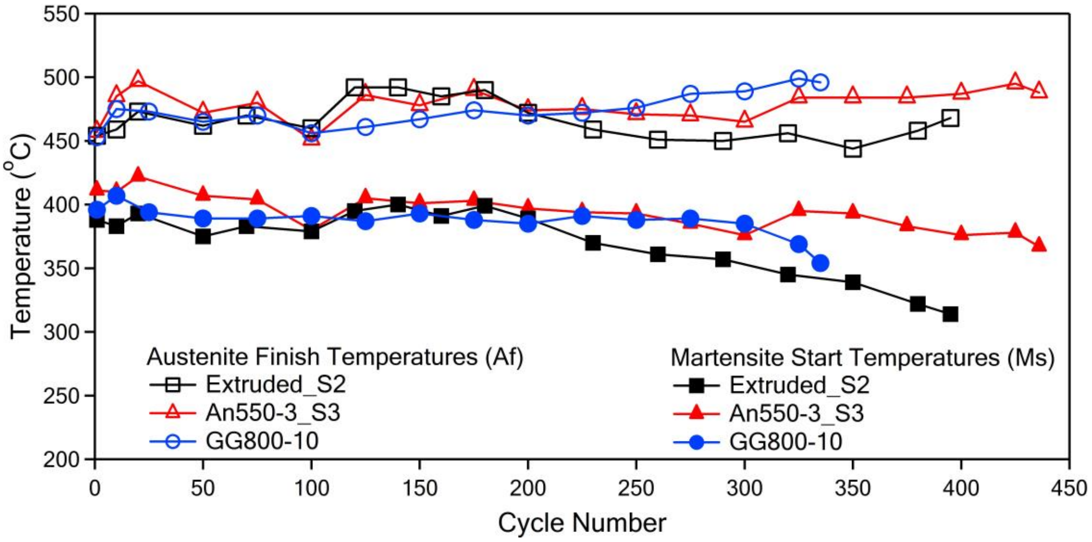

Figure 4.28. Transformation Temperatures for selected specimens

It was already known that, higher dislocation density causes to observe lower M_s temperatures. Extruded sample had lower M_s temperature at the start and decreased even further with the thermal cycling.

4.4. Tensile Experiment Results

Tensile experiments were performed in order to determine the load magnitude in creep experiments so that the loads applied in the creep experiments were kept below the yield strength of the material. The deformation mechanism of SMAs in tensile loading differs mainly depending on the test temperature and the strength of the alloy. If the test temperature is at least above M_s temperature then stress induced martensite (SIM) may form via austenite to martensite transformation with the application of the load. After SIM formation, the martensite starts to detwin which leads to observe high strain magnitudes. However, if the strength of the alloy is not high enough (yield strength of the material is lower than that of the stress necessary to induce martensite) then the alloy may yield instead of transforming to martensite. All the test temperatures that were used in this study were higher than the A_f of the alloy. Therefore, it was accepted that the alloys were kept in austenite before loading.

Tensile experiments were conducted at 390°C, 450°C, 520°C and resulting strain-stress graphs were plotted for An550-3 samples in Figure 4.29. GG800-10 sample was also tested at 500°C and results of this experiment together with the result of An550-3 sample were drawn in Figure 4.30 for comparison.

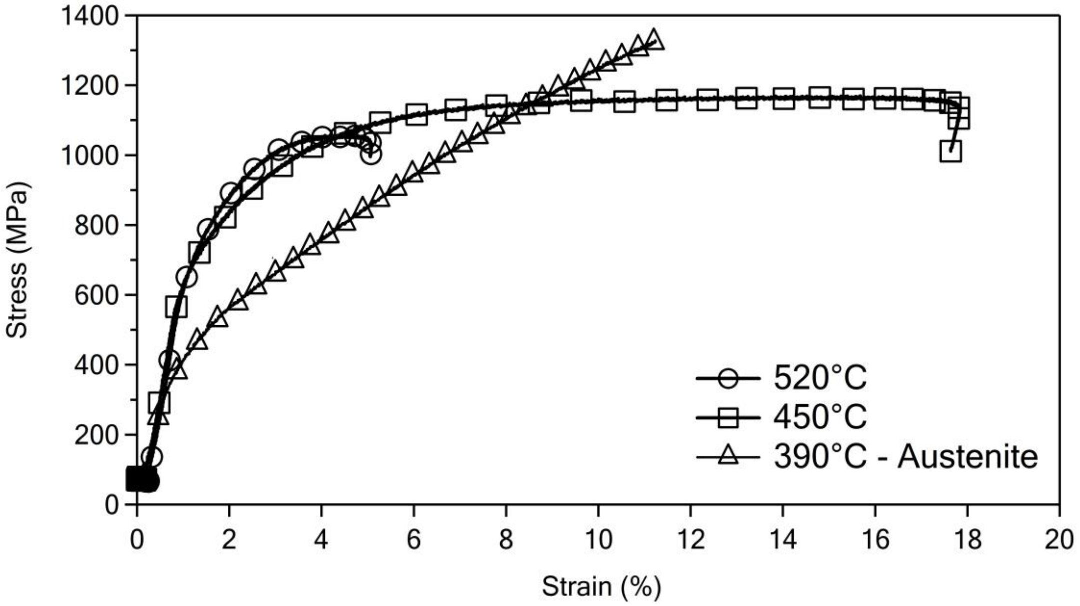

Figure 4.29. Tensile experiment results of An550-3 samples

Tensile experiments of An550-3 sample were conducted at 3 different temperatures. 520°C was the highest possible temperature that the heating equipment and grips can withstand and the tensile experiment was conducted at this temperature to determine loading conditions for 550°C creep experiments. Tensile experiment at 390°C was conducted after heating the sample to 450°C and cooling down to test temperature. Hence, experiment was run while the sample was still kept at austenite phase since the test temperature which was 390°C, was 20°C above the M_s temperature that was found from DSC experiments as shown in Table 4.2. Results of the tensile experiment that was performed at 450°C also confirmed the loading conditions of the 450°C creep experiments, since the yield stress of austenite phase was found to be over 600 MPa. On the other hand, the stress plateau in stress-strain diagram of 450°C experiment was much longer than 520°C experiment and corresponds to the detwinning of martensite.

At 390°C, sample showed stress magnitude that was enough to induce martensite at around 400 MPa loading. However, SIM formation did not finish before failure. Simultaneous SIM formation and yielding resulted with a linear increase in stress up to failure. It can be claimed that, SIM formation and subsequent detwinning of the martensite together with the strain hardening of martensite led to observe failure at very high stress magnitude of 1350 MPa.

Tensile experiment that was performed at 450°C temperature showed the highest strain in all three experiments. SIM and the detwinning of martensite at 450°C caused more strain formation at a constant stress value of 1100MPa and the samples failed after achieving 18% of deformation. The sample was that was tested at 520°C under tension showed strain hardening and failed at lower stress and strain values since the sample was still in austenite. Considering stress plateau at the stress-strain diagram of 450°C experiment, higher strain value at 450°C could be explained with the simultaneous SIM formation along with detwinning of martensite together with the plastic deformation of the austenite. In the literature higher elongation just above A_f temperature was attributed to transformation-induced plasticity (TRIP) [103]. TRIP was explained for austenitic steels as delayed necking and higher elongation due to SIM formation during plastic deformation of the sample [104].

In Figure 4.30 tensile experiment of An550-3 at 520°C was again plotted to compare the tensile experiment result of GG800-10 sample at 500°C. Both experiments showed similar strain hardening behavior up to 1000 MPa. GG800-10 sample had higher strength than An550-3 sample for the same strain values. Higher strength was also not expected due to possibly larger grains of GG800-10 samples. On the other hand, strength difference was not high enough since there was 20°C of difference between the testing temperatures. It is hard to draw a conclusion from the tensile test results of single samples for each condition; nevertheless, tensile experiments were already provided necessary information for the elastic region of the samples having different thermo-mechanical treatment conditions. Information that was gathered from tensile experiments were used to determine the load magnitude in the creep experiments.

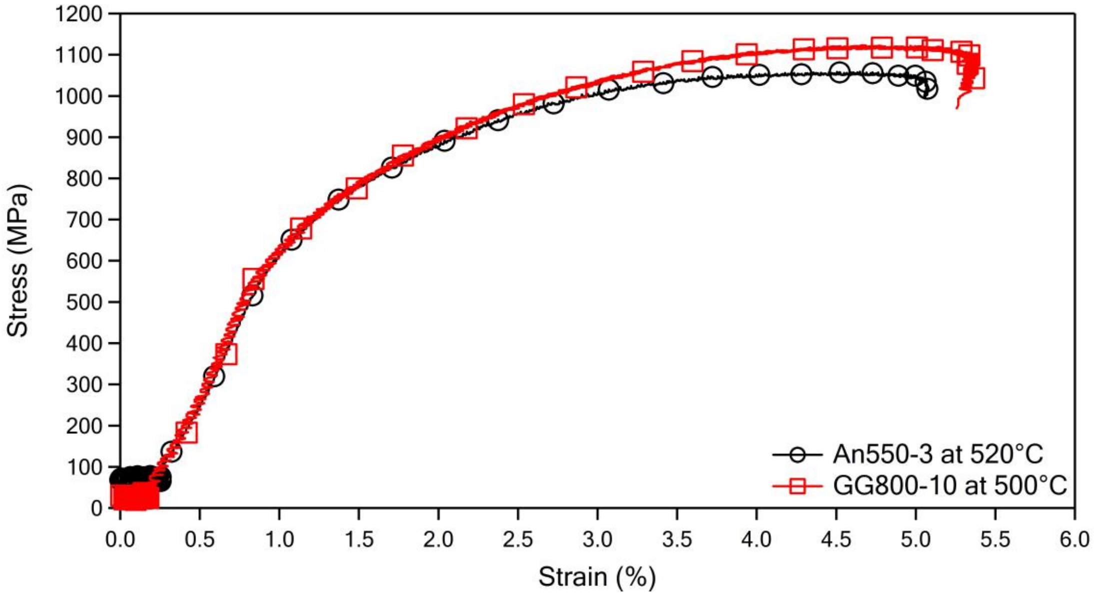

Figure 4.30. Tensile experiment of GG800-10 sample at 500°C, plotted with An550-3 sample at 520°C

Tensile experiments revealed that, at and above 450°C, creep loading conditions of 200 MPa to 500 MPa were lower than the yield strength of the material. Stress induced martensite was formed at 390°C under 400 MPa that indicates creep test temperatures were also above the temperature at which SIM formation takes place for the An550-3 samples.

4.5. Creep Experiment Results

Creep experimental results were presented in two parts; i) creep experiments of An550-3 samples and ii) creep experiments of GG800-10 samples. The samples, which were annealed and grain growth heat treated, might have different grain sizes and so revealed different creep deformation rates. Thus, creep parameters were calculated separately and compared with literature.

4.5.1. Creep Experiments of An550-3 Samples

Experimental results in this section was published in Materials Today Communications journal in December 2022 issue with article number 104827.

Creep experiments at 600°C were performed up to 5 hours under 200, 300, 400, 500 MPa equivalent constant loading conditions as listed in Table 3.1. Results of all creep experiments that were conducted on An550-3 samples at 600°C plotted together in Figure 4.31.

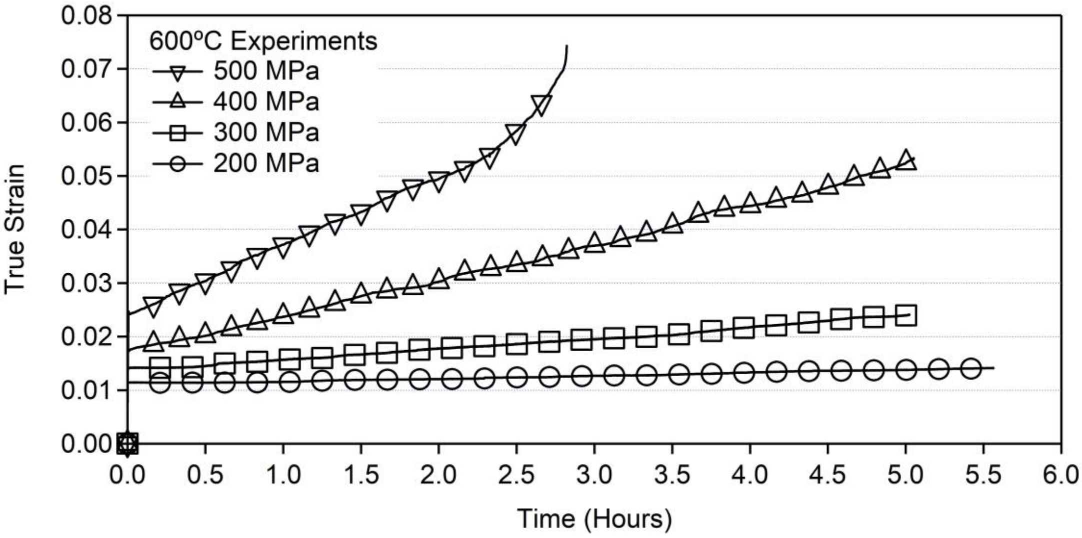

Figure 4.31. Creep experiment results of An550-3 samples at 600°C [68].

Y axis presented in True Strain and strain conversion was mentioned in experimental procedures chapter. X axis was converted from seconds to hours in order to easily compare the experimental results. Strain rate values were measured as strain per second. It was also clear that all experiments, including 500 MPa loading condition which showed tertiary creep formation and failure around 3 hours, did not show any primary creep formation. Secondary creep formation, which showed linear increase in strain, started immediately after the loading. This could be explained with the previous annealing heat treatment, where dislocation formation from extrusion was annihilated to a degree that creep deformation can not form strain hardening at this temperature. Strain rates that were measured from 600°C experiments were tabulated in Table 4.4.

Table 4.4. Steady state creep strain rates for An550-3 samples at 600°C [68]

Initial Stress (MPa)	Strain Rate (s^{-1})
200	1.55e-07
300	5.67e-07
400	1.91e-06
500	3.56e-06

Steady state creep strain rates at 600°C were all on the order of 10^{-6} and 10^{-7}. The creep rate that was drawn from the experiments conducted under 200 MPa loading condition was noticeably very low. For 400 MPa loading condition, creep deformation for a duration of 5 hours which was actually the time spent in functional fatigue experiments, resulted 0.03 true strain. As it can be seen from the Table 4.4, the strain rate that was obtained via 200 MPa loading was around 1/10th of the strain rate of 400 MPa loading. It can be deduced that creep deformation under 200 MPa at 600°C has about 0.003 strain formation during the duration of 5 hours.

Creep experimental results at 550°C testing temperature were conducted with 3 loading conditions for longer period of time as tabulated in Table 3.1, due to decrease in creep strain formation at lower temperatures. All experiments that were conducted at 550°C were plotted in Figure 4.32.

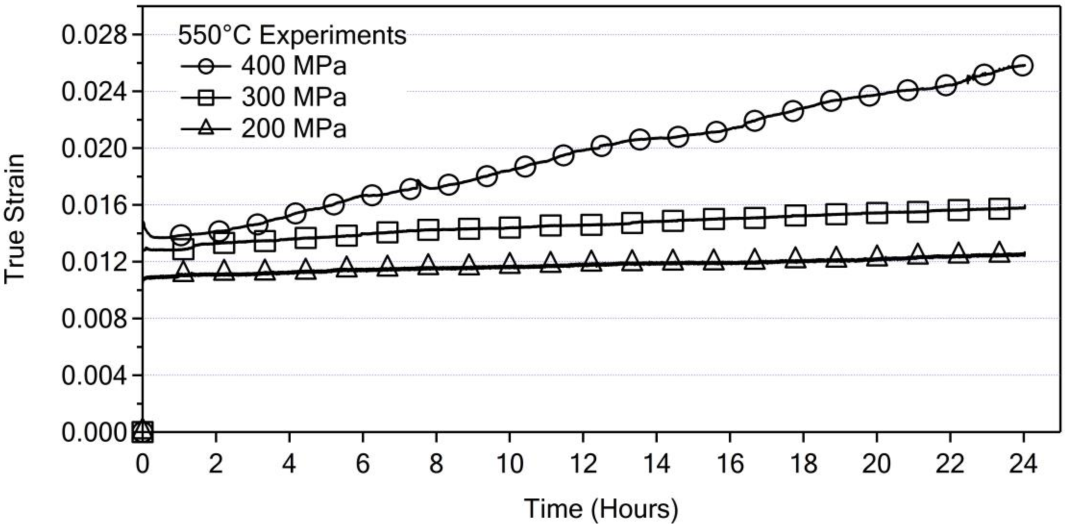

Figure 4.32. Creep experiment results of An550-3 samples at 550°C [68].

Sample that was loaded with 400 MPa equivalent dead weight at 550°C showed linear creep deformation starting from 0.014 to 0.025 true strain values, 0.011 true strain value change was achieved. Creep strain formation was much smaller under 300 MPa and 200 MPa loading conditions than the creep strain formation under 400 MPa loading condition. Strain rates were measured in seconds and tabulated in Table 4.5.

Table 4.5. Steady state creep strain rates for An550-3 samples at 550°C [68].

Initial Stress (MPa)	Strain Rate (s^{-1})
200	1.6512e-08
300	3.5543e-08
400	8.44e-08

Steady state creep strain rates in the Table 4.5 are on the order of 10^{-8}. At 450°C, three loading conditions which were 300, 400 and 500 MPa equivalent of dead weight were utilized. Creep experiment results were plotted in Figure 4.33.

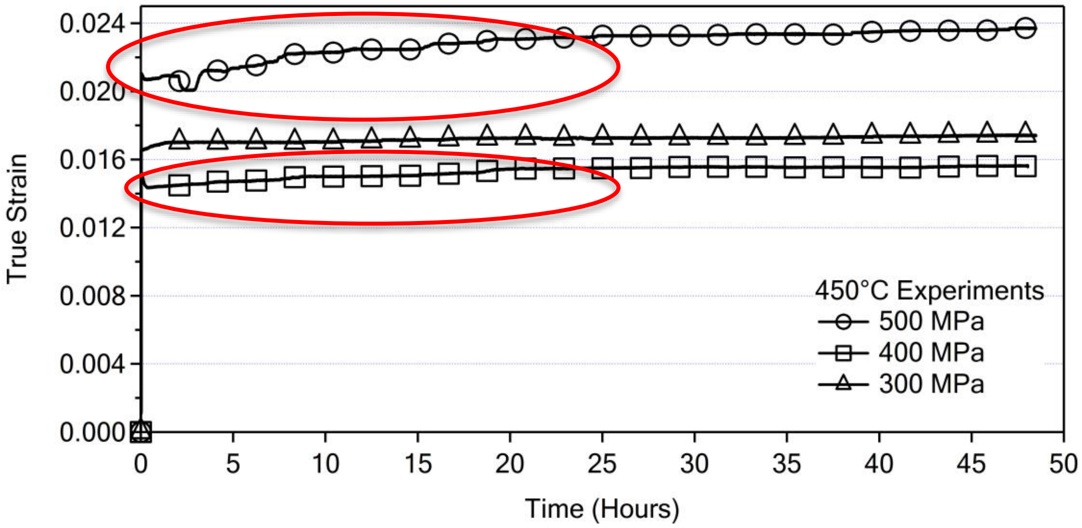

Figure 4.33. Creep experiment results of An550-3 samples at 450°C [68].

A clear primary creep formation was visible for all 450°C experiments, for 400 MPa and 500 MPa loading conditions. Primary creep regions were shown with red circles in Figure 4.33. Lowest strain rates were measured after 24 hours of creep deformation. Strain rates for 450°C experiments were tabulated in Table 4.6.

Table 4.6. Steady state creep strain rates for An550-3 samples at 450°C [68]

Initial Stress (MPa)	Strain Rate (s^{-1})
300	3.69e-10
400	8.48e-10
500	2.08e-09

Steady state creep strain rates at 450°C were on the order of 10^{-10}, thus it was hard to measure the strain values with the potentiometric displacement sensor. Occasional jumps were present in the data and strain rates were measured between these jumps. In the next sections, creep model parameters that were found from the experimental results were presented.

4.5.1.1. Stress Exponent Na Creep Model Parameters for An550-3 Samples

Creep experimental results were used in order to calculate Na stress exponent to reveal creep behavior of the alloy. As explained in the literature survey chapter, stress exponent denotes the creep deformation behavior of the sample in relation with stress. For this purpose, stress exponent part of the equation (2) was rewritten as in the form of linear expression.

$$\dot{\varepsilon} = \sigma^{Na} \tag{3}$$

$$\log(\dot{\varepsilon}) = \mathrm{Na}\log(\sigma) \tag{4}$$

Log scale strain rates were plotted in order to show the slope of the data points in Figure 4.34.

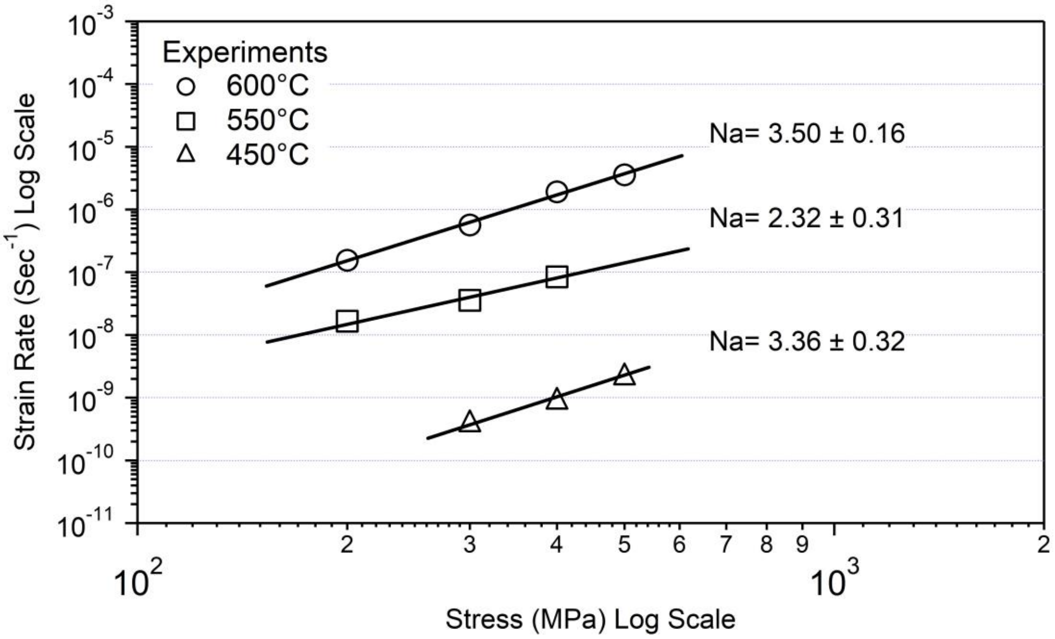

Figure 4.34. Strain rate vs Stress plot for stress exponent calculations of An550-3 samples.

Stress exponent of An550-3 samples were found to be 3.50, 2.32 and 3.36 for the creep experiments that were run at 600°C, 550°C and 450°C, respectively. As it was stated in literature survey chapter, stress exponents between 1 and 2 were an indication of diffusional creep for the loading conditions. Stress exponents between 4 and 5 were defined as Dislocation Climb behavior. Stress exponents equal to 3, corresponded to “Viscous Glide Creep” in which dislocation motion was controlled with a limiting factor [73]. Viscous glide creep was also found by Mukherjee [79], Kato et al. [81], Lexcellent et. al. [82] and Oppenheimer et al. [85] for NiTi alloys. Discussion on differences between 600°C and 550°C stress exponent and how it might be related with the grain structure will be made in section 4.5.3, after all experimental results on creep were presented.

4.5.1.2. Activation Energy Q Creep Model Parameters for An550-3 Samples

It has been stated by Mukherjee and Eggeler et. al. that activation energy was not related with stress in NiTi alloys [79,84]. Hence the exponential part of the power law equation can be used to find the activation energy (Q) of the alloys from the creep experiments. As it was done for the stress exponent, activation energy part could be rewritten in linear form to plot the experimental data.

$$\dot{\varepsilon} = e^{-Q/RT} \qquad (5)$$

$$\frac{\ln(\dot{\varepsilon})}{1/\mathrm{T}} = -Q * \frac{1}{R} \qquad (6)$$

Using this linear form of the activation energy equation, natural logarithm of strain rate can be plotted with respect to 1/T. Slope of the plots were multiplied with ideal gas constant R to find the activation energy term (Q). Activation energy values in the literature was in kJ in SI units, so that X-axis was presented as 1000/T in Figure 4.35 for convenience.

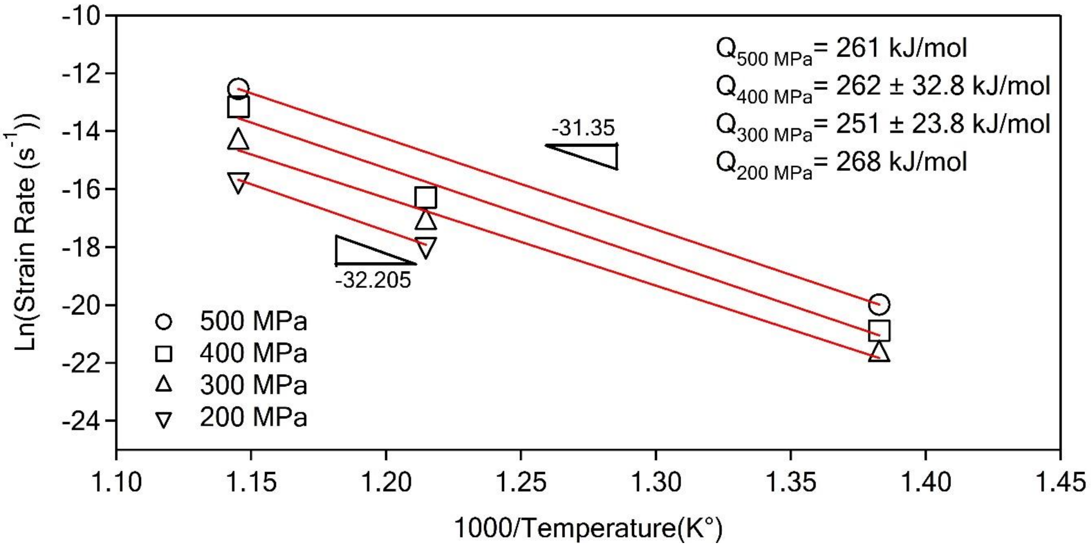

Figure 4.35. Natural logarithm of Strain Rate vs 1000/Temperature plot for An550-3 samples.

Activation energy values were calculated as around 260 kJ/mol for An550-3 samples. Results were also tabulated in Table 4.7.

Table 4.7. Calculated activation energies of An550-3 samples

Initial Stress (MPa)	Q (kJ/mol) Activation Energy
200	268
300	251 ± 23.8
400	262 ± 32.8
500	261

4.5.2. Creep Experiments of GG800-10 Samples

Creep experiments on GG800-10 samples were conducted at 600°C, 550°C and 500°C temperatures but were not conducted at 450°C. Since An550-3 samples yielded strain rates on the order of 10^{-10} and was expected to acquire lower strain rates for GG800-10 samples that may have larger grain sizes. Therefore, lowest temperature for creep experiments on GG800-10 was selected as 500°C. For the same reason, 200 MPa equivalent loading condition was not preferred for GG800-10 samples and experiments were conducted under 300, 400, 500 MPa loading conditions.

Experiments that were done at 600°C were not stopped and tertiary creep was observed. In addition, experiments were finished with the failure of GG800-10 samples. True strain vs time graph that was gathered from the creep experiments of GG800-10 samples were presented in Figure 4.36.

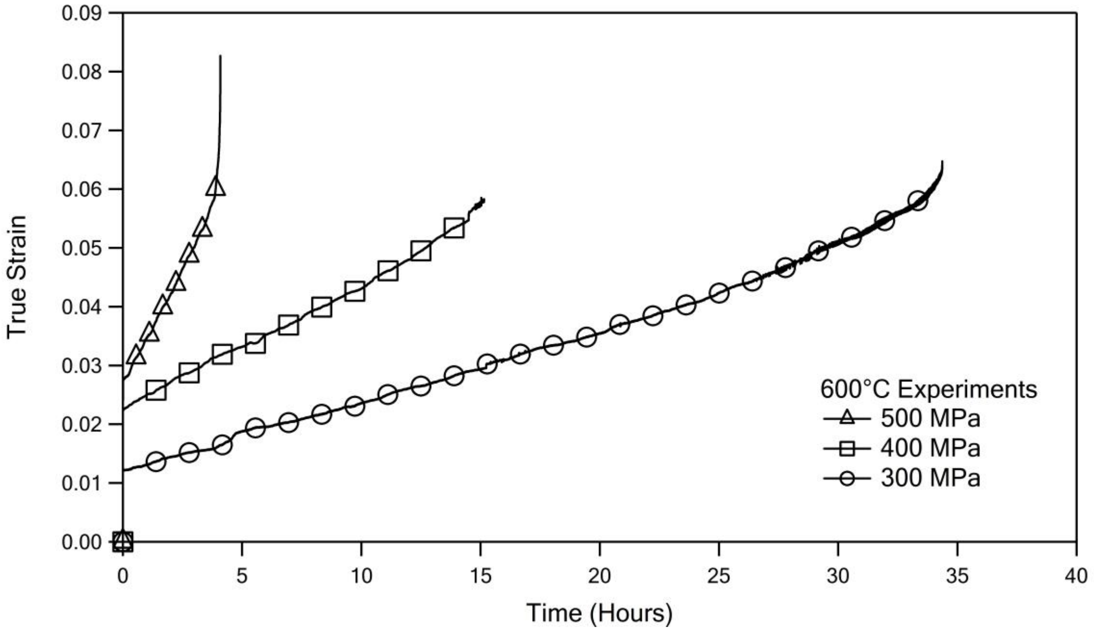

Figure 4.36. Creep experiment results of GG800-10 samples at 600°C

GG800-10 samples did not also show any primary creep stage at 600°C experiments. All experiments started with linear deformation up to failure. Specimen that was creep tested under 400 MPa loading condition did not fail. Experiment was stopped due to excessive decrease in cross section of the specimen. Steady state creep strain rates that were calculated from the linear region of the True Strain vs Time graphics were tabulated in Table 4.8.

Table 4.8. Steady state creep strain rates for GG800-10 samples at 600°C

Initial Stress (MPa)	Strain Rate (s^{-1})
300	3.36e-07
400	5.67e-07
500	2.21e-06

Steady state strain rate values of GG800-10 samples were drawn from 600°C creep experiments and it was found that the values were less than half of the strain rate values of An550-3 samples which were presented previously in Table 4.4. Lower strain rates were expected due to larger grain size of GG800-10 samples. It can be concluded that grain growth heat treatment increased the resistance to creep deformation.

The true strain vs time graphics of creep experiments which were conducted at 550°C were plotted in Figure 4.37. As it can be seen from the figure, experiment that was conducted under 500 MPa was carried out up to failure. On the other hand, experiment that was conducted under 400 MPa loading condition was stopped due to data acquisition error. Nevertheless, creep experiment had been already run up to 36th hour without the formation of the primary creep stage and therefore, enough data were collected for measuring the strain rate.

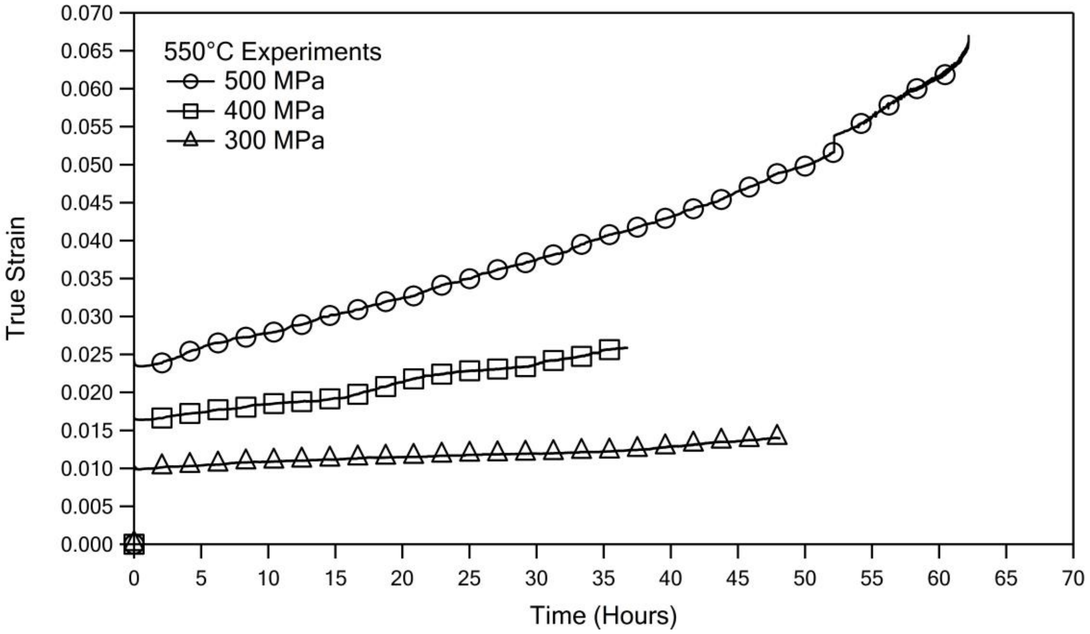

Figure 4.37. Creep experiment results of GG800-10 samples at 550°C

Creep experiment at 550°C under 300 MPa load was performed up to 48 hours as it was stated in Table 3.2. Strain rate values which were acquired from the creep experiments were presented in Table 4.9.

Table 4.9. Steady state creep strain rates for GG800-10 samples at 550°C

Initial Stress (MPa)	Strain Rate (s^{-1})
300	1.98e-08
400	7.48e-08
500	1.4e-07

True strain vs time graphics of the creep experiments that were conducted at 500°C were plotted in Figure 4.38. Primary creep deformation stage was noticeable for 500 MPa loading condition and a non-linear increase of true strain values were observed for the creep experiments that were conducted under lower stress conditions for the first 24 hours period of the experiments.

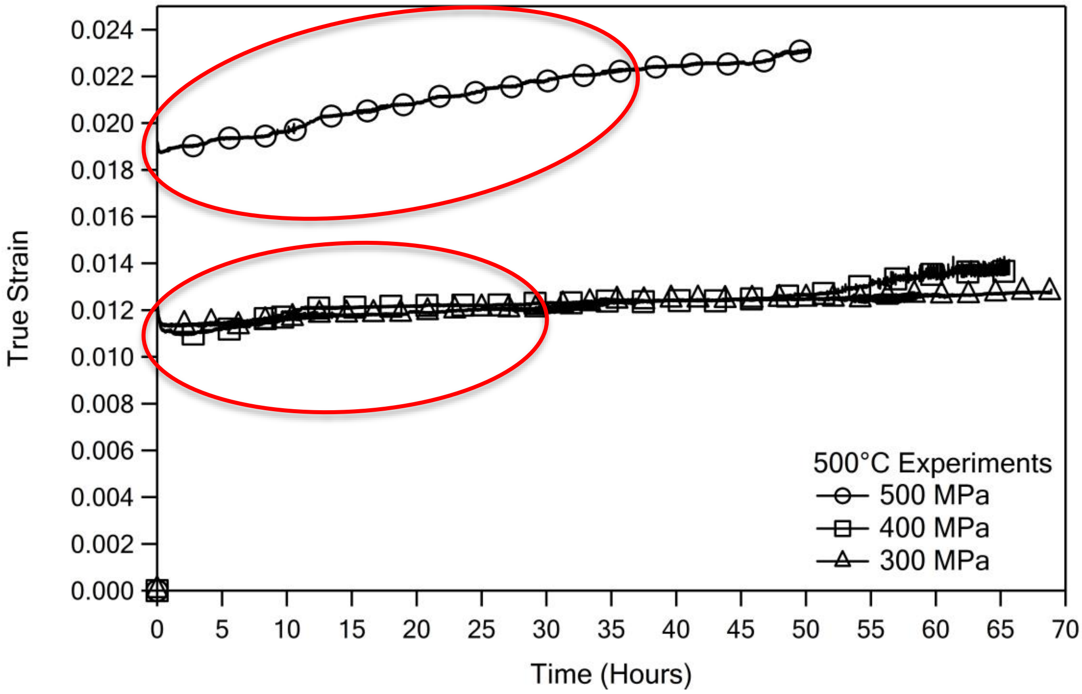

Figure 4.38. Creep experiment results of GG800-10 samples at 500°C

Steady state strain rate values were calculated from the experimental data that were acquired between 35 hours to 50 hours. Occasional jumps were also formed as observed during creep experiments that were conducted on An550-3 samples at 450°C. Calculated steady state strain rate values were tabulated in Table 4.10. Creep experiments at 500°C were yielded steady state creep strain rates on the order of 10^{-9}.

Table 4.10. Steady state creep strain rates for GG800-10 samples at 500°C

Initial Stress (MPa)	Strain Rate (s^{-1})
300	1.69e-09
400	3.26e-09
500	1.36e-08

4.5.2.1. Stress Exponent Na Creep Model Parameters for GG800-10 Samples

Stress exponent calculations were done via using the best line fits to the data that were shown in Figure 4.39. Steady state strain rates and corresponding stresses were also shown in logarithmic scale in the same figure.

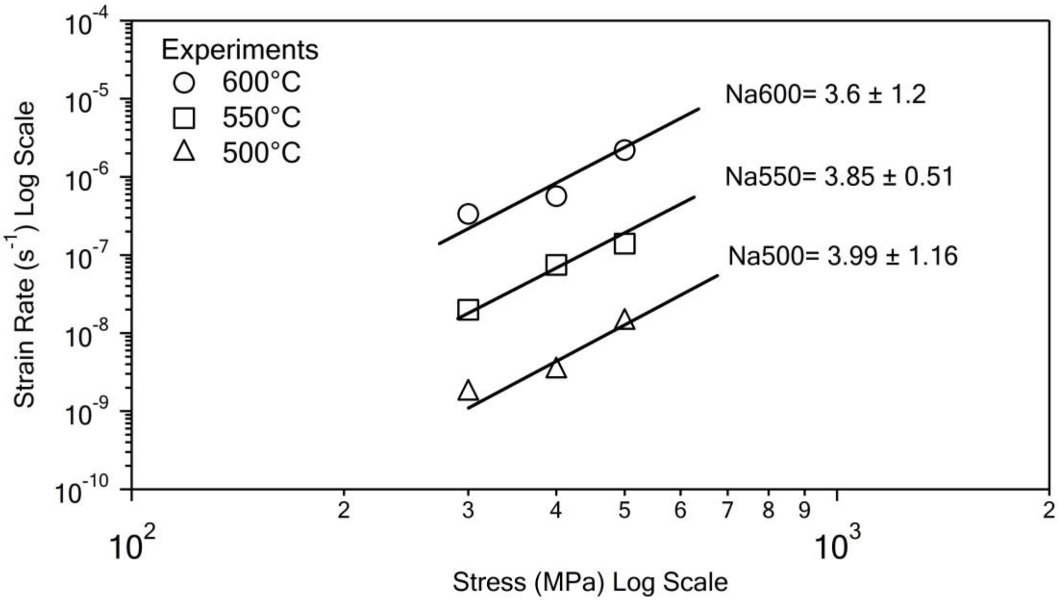

Figure 4.39. Strain Rate vs Stress plot for stress exponent calculations of GG800-10 samples.

Slopes of the linear fits to data points were calculated as 3.6, 3.85 and 3.99 for 600°C, 550°C and 500°C experiments, respectively. It can be noticed that stress exponent Na was higher than that of An550-3 samples, which were creep tested at temperatures lower than 600°C. At 600°C, An550-3 and GG800-10 samples resulted similar stress exponents which are 3.5 and 3.6, respectively. Increase in Na values at the same creep temperature indicated that the effect of stress on creep behavior of the material was increased with grain growth heat treatment.

4.5.2.2. Activation Energy Q Creep Model Parameters for GG800-10 Samples

Activation energy values for GG800-10 samples were also calculated using equation (6) derived from the linearization procedure applied to the equation (5) exponential part of the power law equation (2) and by finding the slopes of the best line fit. Natural logarithm of strain rate values vs 1000/Temperature (in Kelvin) were plotted with in Figure 4.40.

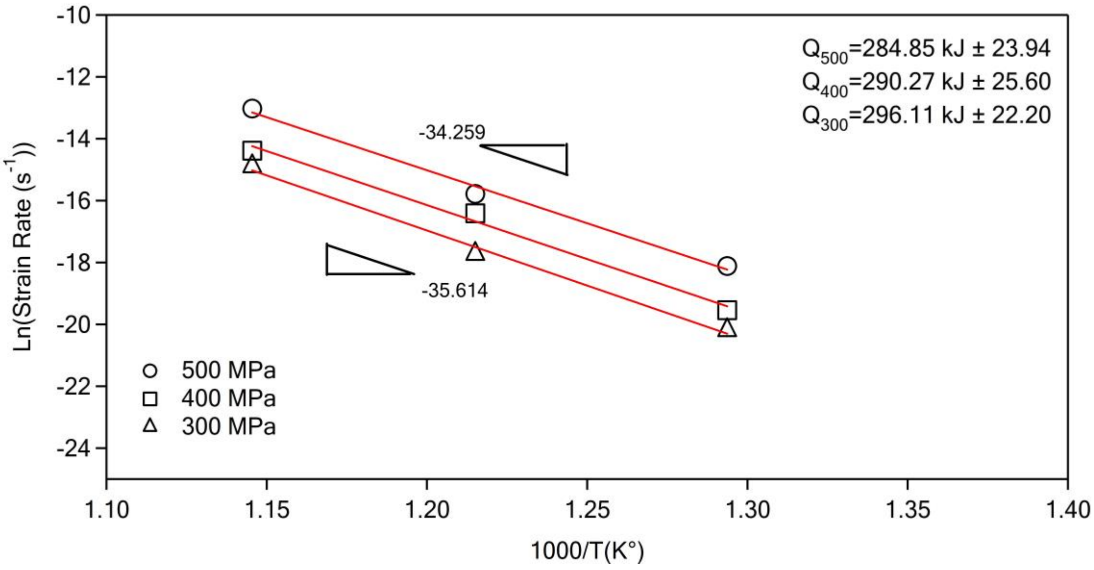

Figure 4.40. Natural logarithm of Strain Rate vs 1000/Temperature plot for GG800-10 samples.

Activation energy Q for GG800-10 samples were calculated as around 290 kJ/mol. Temperature dependence of steady state creep strain rate were decreased as activation energy values increased. Results were tabulated in Table 4.11.

Table 4.11. Calculated Activation Energies of GG800-10 samples

Initial Stress (MPa)	Q (kJ/mol) Activation Energy
300	296.11 ± 22.20
400	290.27 ± 25.60
500	284.85 ± 23.94

4.5.3. Discussion on Creep Parameters

The creep parameters stated in the power law equation were found for An550-3 and GG800-10 50at%Ni-25at%Ti-25at%Hf samples. Stress exponent (Na) and activation energy (Q) values for An550-3 samples were found to be similar to the previous findings of Mukherjee [79], Kato et al. [81] and Lexcellent et. al. [82] for NiTi binary alloys in the literature. On the other hand, creep parameters for GG800-10 samples were found to be closer to Eggeler et. al.'s findings [84]. Activation energy calculation results that were found by Mukherjee and Kato et. al. was round 250kJ/mol. Lexcellent et. al. founded a lower activation energy of 226 kJ/mol [79,81,82]. Creep experiments that were conducted on An550-3 samples in this study yielded 260kJ/mol activation energy with the uncertainty of ±23.8 kJ/mol and ±32.8 kJ/mol for 450 ^{o}C to 600 ^{o}C experiments, respectively. On the other hand, experiments that were conducted on GG800-10 samples showed higher activation energy values of 290 kJ/mol with an average uncertainity of ±23,5kJ/mol. Activation energy calculations that were made by Eggeler et al. was around 304 kJ/mol and stress exponent was calculated as 4.7 for the creep deformation higher than 10% strain [84].

Stress exponent Na signifies the effect of stress on creep deformation. An550-3 samples showed 3.5 Na value at 600 ^{o}C testing conditions which was nearly same as the Na value of (3.6) of GG800-10 samples at the same conditions. However, when testing temperature was set to 550 ^{o}C, An550-3 and GG800-10 yielded Na values of 2.32 and 3.85, respectively. The decrease in stress exponent that was observed from the experiments conducted at 550 ^{o}C, could be explained with the fact that the experiment temperature was also the annealing temperature of the sample. The grains are likely to grow at this temperature. Depending on the location of tensile sample considering the cross section of the extruded rod, samples might have different subgrain formations and dislocation density. Annealing at 550 ^{o}C was proven to be effective in eliminating the variations in functional fatigue experiments [90]. However, creep experiments had generated lower strains at these temperatures, thus grain and dislocation structure of extrusion could still affect the creep behavior. Additionally, it should be also noted that, similar Na values of An550-3 and GG800-10 samples that were creep tested at 600 ^{o}C would mean that grain growth rate at 600 ^{o}C was much higher than that of 550 ^{o}C. Increasing in Na values with decreasing creep temperature of GG800-10 samples showed that applied stress has higher effect on samples with larger grain structure at lower temperatures.

In literature only Kato et. al and Eggeler et. al. reported the grain sizes of virgin sample. Kato et. al. stated that, as received NiTi materials were in wire form and annealed at 900°C for 72 minutes. After annealing, Kato et. al. reported the average grain size as 15 microns [81]. Eggeler et al. represented that, as received material was in rod shape and solution annealing heat treatment was applied for 15 minutes at 850°C and the resulting grain size was reported as 35 microns [84]. The variations in creep parameters in literature was found to be the result of grain size differences, as it was found in this thesis.

In Figures 4.35 and 4.40, activation energy calculations were done using temperature versus natural logarithm of strain rates plots. Slopes of the lines for all loading conditions were similar, thus it was concluded that activation energies of 50at% Ni – 25at%Ti – 25at%Hf were insensitive to applied load. This result was also reported in literature that activation energy was found to be only dependent on creep test temperature for NiTi alloys [79]. Stress dependence of activation energy was reported to be found in creep experiments which were conducted at lower temperatures and under higher stress conditions [105].

Lexcellent's group had also studied diffusion characteristics and vacancy formation of NiTi alloys. Bernardini et. al. reported that, the activation energy of Ni tracer atom diffusion in NiTi was 155kJ/mol [83]. Erdelyi et. al. conducted experiments on NiTi alloy at 1285°K temperature and found similar vacancy concentrations under increasing load magnitudes up to 900 MPa. Considering Ni tracer diffusion results, Erdelyi et. al. claimed that Ni diffusion in NiTi was not vacancy-mediated, instead Ni tracer atoms were using interstitial positions [106]. Lexcellent et. al. reported creep activation energy of NiTi as 226 kJ/mol which was higher than the activation energy of Ni tracer atom diffusion. Lexcellent et. al. argued that, creep deformation activation energy was related with the activation energy of Titanium diffusion in NiTi alloys [82]. Similar activation energy values for NiTiHf alloys that were found in this thesis also suggested that creep deformation of NiTiHf was also controlled by titanium diffusion. Although titanium atomic percentage in NiTiHf alloy is 25%, titanium atoms in equiatomic NiTi was replaced with Hafnium atoms due to similar atomic sizes of Ti and Hf.

Lagoudas and his coworkers published the creep deformation characteristics of TiPdNi alloy in which the loading conditions vary between 100 to 500 MPa and temperatures were around 0.5Tm [12]. It was reported that TiPdNi alloys exhibit higher stress exponent that is around 4-5. These values indicated dislocation climb behavior and stress exponent value of 8.5 represented power law breakdown. While NiTiHf and NiTi alloys present viscous glide creep behavior due to having similar stress exponent values, higher stress exponents of TiPdNi could be explained with the substitution of Nickel with Palladium. It was claimed in Erdelyi et. al. that Ni atoms use interstitial sites [106]. Thus activation energy of Titanium diffusion might be in relation with the amount of Nickel in the matrix. As a result lower Ni content of the TiPdNi alloys, changes the creep behavior of the alloy via changing the activation energy of Titanium diffusion. Kato et al.'s findings on NiTi alloy with 49.5at% Ni content, in which stress exponents were converging to viscous glide creep (2.5) from dislocation climb (4) with increasing temperature (Figure 2.17) [81], may also be related with the effect of Ni content on the creep behavior of NiTi and NiTiHf alloys.

It was found that, samples that were creep tested at 550°C and 600°C did not reveal any strain hardening, in other words primary creep deformation stage did not exist. This might be the result of easier dislocation movement in annealed and grain growth heat treated samples. Grain growth and annihilation of dislocations may be promoted at high temperatures as well and also, it was proven that, the samples that were creep tested at 450°C showed primary creep deformation behavior throughout 24 hours of creep testing period.

4.6. Comparison of Functional Fatigue Austenite Strain Rate and Creep Strain Rate

Austenite Strain data from functional fatigue experiments were previously defined as the accumulated irrecoverable strain. Since austenite strain plots were in terms of strain versus cycle number, it can be transformed into strain versus time plot, simply replacing cycle number with time. Plotting strain rate using s^{-1} in functional fatigue experiments would present a comparison opportunity with the creep curves that were obtained from the creep experiments.

All functional fatigue experiments were conducted under 200 MPa loading condition between 200°-600°C with a heating/cooling rate of 15°C per second. Using the heating cooling rate, one heating-cooling cycle takes place in 53.33 seconds to complete the cycle. Cycle number was multiplied with 53.33 seconds to reveal total time of the functional fatigue experiments. Strain data were presented in Figures 4.22 and 4.23 in percentage, thus all strain data also must be divided with 100.

In following sections, conversion of the austenite strain versus number of cycle plots from Figure 4.22 to strain versus time plots was presented and linear deformation strain rates were compared to the creep deformation.

4.6.1. Comparison of Austenite Strain and Creep Strain for An550-3 Samples

Strain rate was calculated from the linear regions of the strain vs time curve of An550-3 between 20th cycle and 275th cycle. It was noticeable from Figure 4.23 that strain hardening was observed during the first 20 cycles and strain increased non-linearly after 275th cycle. Strain rate in austenite strain was calculated as $6.1058e^{-06}s^{-1}$ and shown in figure 4.41.

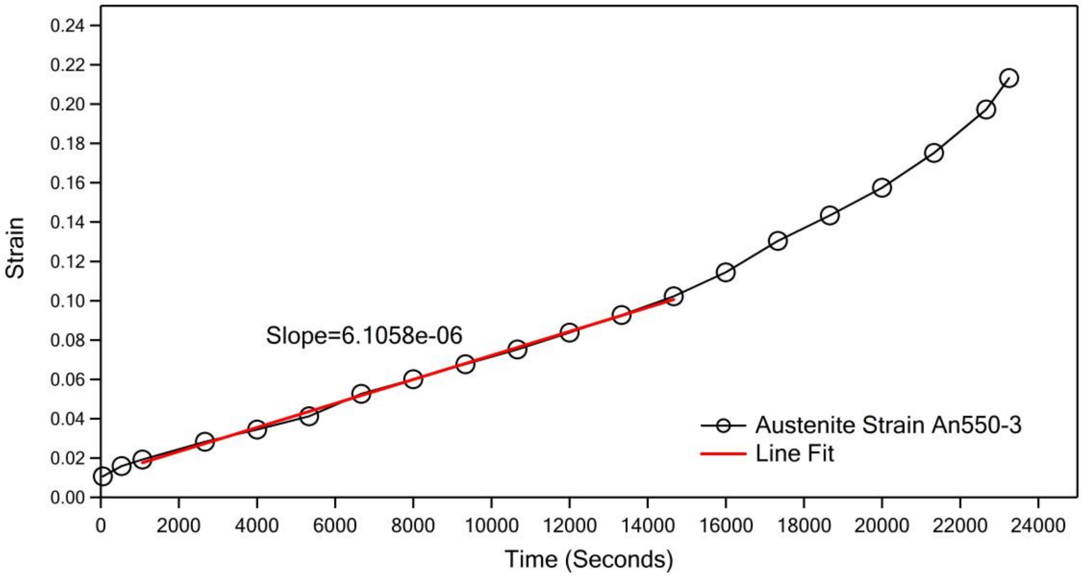

Figure 4.41. Austenite Strain data from An550-3 Sample 3 Functional Fatigue Experiments

Austenite strain rate was found to be as 40 times more than that of the creep strain rate that was calculated from the curve that was obtained from the creep test conducted under 200 MPa constant loading at 600°C. It was also 2 times more than the strain rate of creep experiments that were run under 500 MPa loading at 600°C. It can be concluded that creep has little to no effect on the plasticity which was occurred during functional fatigue experiments.

4.6.2. Comparison of Austenite Strain and Creep Strain for GG800-10 Samples

Strain rate was calculated from the linear region of the strain vs time graphic of GG800-10 sample which was occurred between 25th cycle and 225th cycle. Austenite strain increased between first and 25th cycle and rapid increase in austenite strain started after 225th cycle. Strain rate from strain vs time graphic was calculated as $9.245e^{-06}s^{-1}$ and shown in figure 4.42.

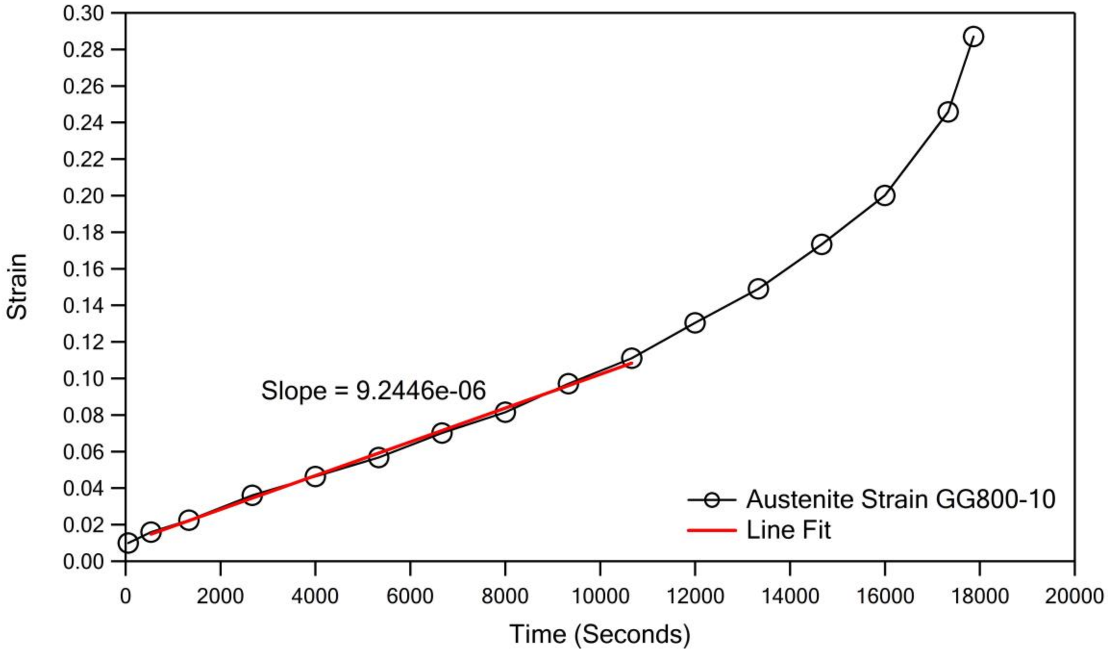

Figure 4.42. Austenite Strain data from GG800-10 functional fatigue experiments

GG800-10 sample with strain rate of 9.245e-6 which was calculated from functional fatigue experiment, showed higher than 4 times the creep rate of GG800-10 sample under 500 MPa loading condition at 600°C, which was calculated from Figure 4.36 and showed in Table 4.8 as 2.21e-6.

Strain rate of austenite strain formation (irrecoverable strain accumulation) from GG800-10 sample functional fatigue experiment was higher than that of strain rate of austenite strain formation for An550-3 sample that was drawn from functional fatigue experiment. Increased rate of accumulated deformation was expected along with the higher actuation strains as shown in Figures 4.20 and 4.21, due to the plastic deformation in functional fatigue experiments. However, GG800-10 samples with larger grains, showed lower creep deformation than that of An550-3 samples in all creep experiments which were conducted at 600°C and 550°C. As a result, it can be concluded that, damage formation in functional fatigue experiments had different mechanisms than the damage formation in creep.

Up to this point, creep and functional fatigue experiments were compared considering different experimental conditions. Comparison of creep and functional fatigue experiments were done with a sense of difference in damage formation. However, creep experiments and functional fatigue experiments were run separately, thus, the combination of the plastic deformation due to creep and function fatigue were not revealed considering the interaction of these two experimental approach. Thermal cycling under stress and creep experiments were conducted consecutively, which will be presented in section 4.7, were designed in order to reveal such interaction.

4.7. Thermal Cycling Under Stress with Subsequent Creep Experiments

The strain vs time graph of thermal cycling under stress and creep experiments that were consecutively conducted on An550-3 sample was plotted in Figure 4.43, since it was easier to explain the experimental procedure with a time scale. As it was explained in chapter 3, every experiment consisted 50 thermal cycles functional fatigue experiment and 3 hours of creep experiment. An550-3 virgin sample was subjected to creep deformation in the beginning of the experiments for 1 hour to reveal the initial creep behavior.

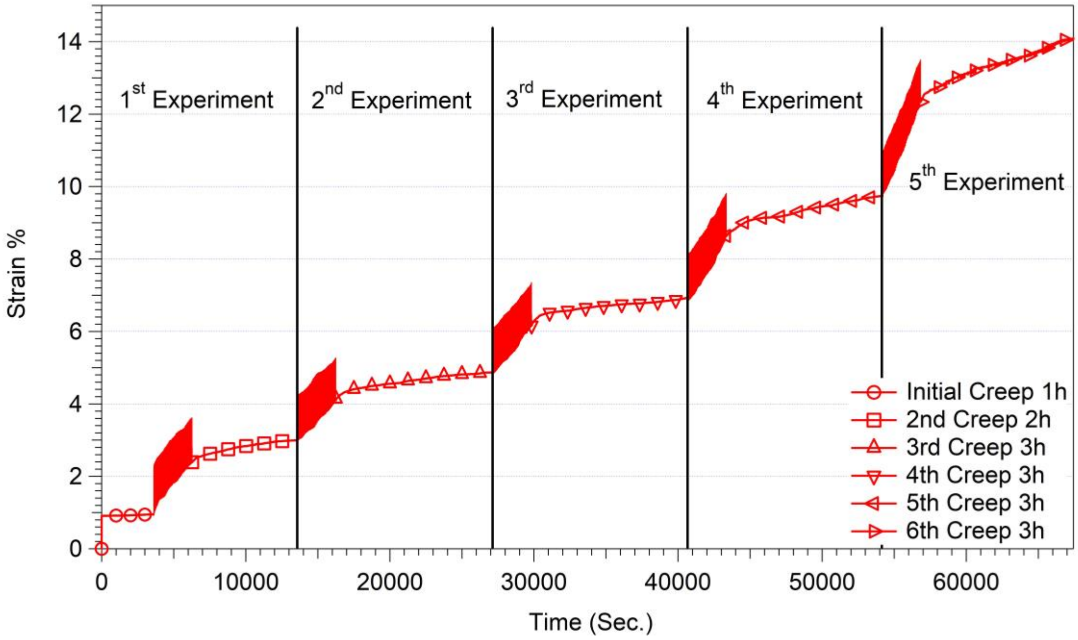

Figure 4.43. Thermal Cycling Under Stress with Subsequent Creep Experiments for An550-3 sample

As it was shown in Figure 4.43, 1st experiment has 2 different creep tests. Initial creep test was run for 1 hour at the beginning and 2nd creep test was run for 2 hours after the first 50 functional fatigue cycles as it was denoted in the legend. Other experiments up to failure were started with 50 thermal cycles functional fatigue experiment and followed with 3 hours long creep experiments.

In the following two sections creep deformation and functional fatigue cycles were presented. Afterwards, micrographs of damage formation of the surface were presented in order to reveal the crack evolution.

4.7.1. Comparison of Creep Deformations in Experiments

Creep experiments were plotted in Figure 4.44 without using numeric values of the strain. The strain axis was given a scale. Data of the creep experiments, which were conducted subsequently to functional fatigue cycles, also included the thermal equilibrium of the grips, therefore first 500 seconds of each creep experiment was shifted to -500 seconds on the x-axis. Initial creep deformation started from the 0 of the x-axis.

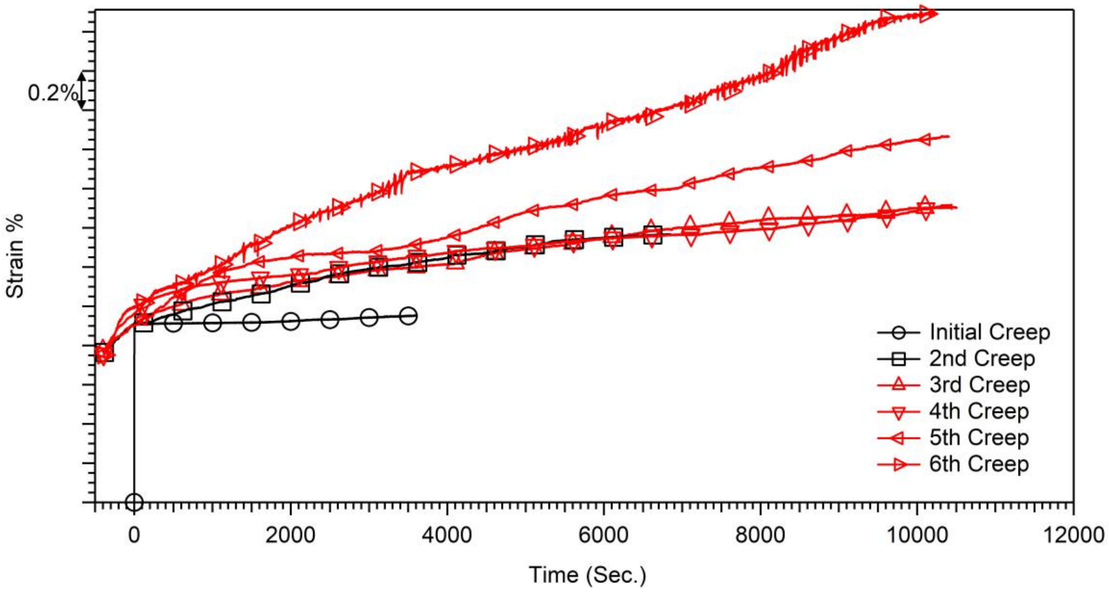

Figure 4.44. All Creep Experiments in Thermal Cycling Under Stress with Subsequent Creep Experiments

In the previous sections, it was showed that creep experiments at 600°C had no primary creep deformation. Initial creep experiment that was plotted in Figure 4.44 also showed a secondary creep stage at the beginning of the experiment. However, other creep experiments that were done after thermal cycling under stress showed decreasing strain rate as it was expected from a primary creep formation. It should be noticed that 2nd, 3rd and 4th creep strains were all on top of each other. With the 5th and 6th creep experiments, due to damage accumulation strain rates were increased. Thermal cycling with subsequent creep experiment cycles were stopped after 6th creep experiment since the sample became too thin to keep the sample at 600°C. All creep strain rates, which were calculated from the last 1 hour of the creep data, were tabulated in Table 4.12.

Table 4.12. Creep strain rates that were measured from Thermal Cycling Under Stress with Subsequent Creep Experiments

Creep Number	Strain Rate (s^{-1})
Initial Creep	1.20e-07
2nd Creep	4.73e-07
3rd Creep	3.16e-07
4th Creep	3.98e-07
5th Creep	7.72e-07
6th Creep	1.60e-06

Initial creep strain rate was calculated as 1.20e-7 as can be seen in Table 4.12, while the creep strain was calculated from the creep experiment that was conducted under 200 MPa at 600°C as 1.55e-7 as it was shown in Table 4.4. However, all creep experiments other than the initial creep experiment showed higher creep strain rates. Although 2nd, 3rd and 4th creep experiments demonstrated similar plots in Figure 4.44, strain rate calculations revealed slight differences. It was due to the 2nd creep experiment that was conducted only 2 hours long so it should be assumed that 2nd, 3rd and 4th creep experiments had nearly the same deformation strain rates.

Thermal cycling with subsequent creep experiment cycles showed that creep deformations after functional fatigue cycles led to observe strain hardening behavior and this indicates that primary creep stage existed. The lack of strain hardening during initial creep experiment suggests that annealing heat treatment at 550°C annihilated dislocations in the matrix and creep experiments at 600°C could not create enough dislocation to initiate the strain hardening mechanism. However, functional fatigue cycling created dislocations that promotes strain hardening during the subsequent creep experiments. As a result, it can be concluded that functional fatigue experiments led to create more dislocations than that of creep experiments at 600°C.

4.7.2. Comparison of Cycles in Experiments

Functional fatigue experiments in the thermal cycling with subsequent creep test alternating experiment were compared using actuation strain and austenite strain data from every 10 cycles. Actuation strain values, presented in Figure 4.45, were in the range of 1% and 1.3% strain until the end of the experiment. However, it can be seen that actuation strain values decreased in each experiment since actuation strains in the 1st experiment was in the range of 1.2% to 1.3% and actuation strains of the 5th experiment was in the range of 1.1% to 1%. Decrease in actuation strain could be explained with oxidation of the sample during creep experiments which may lead to a decrease in transforming volume.

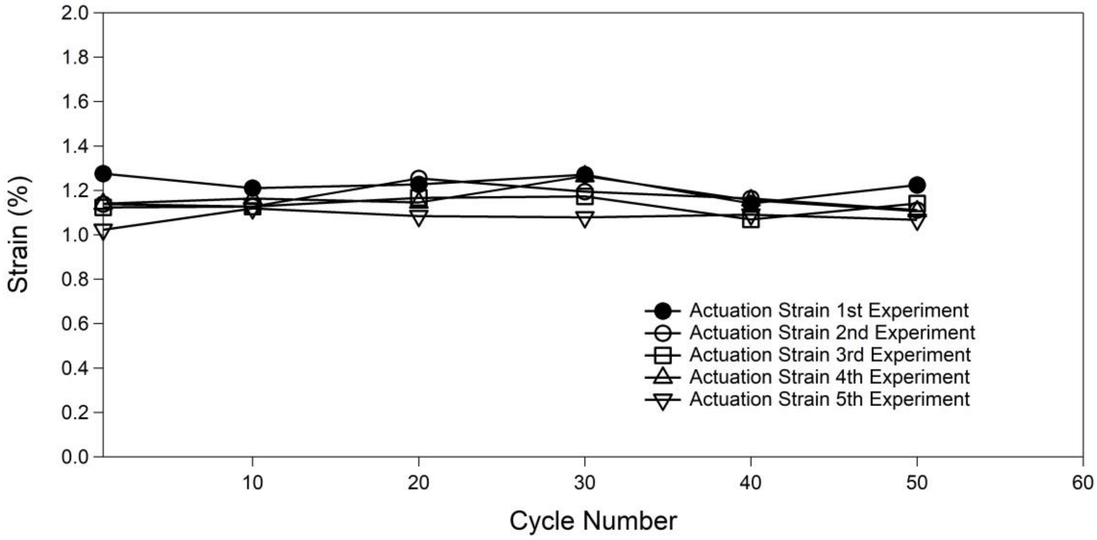

Figure 4.45. Comparison of Actuation Strain values in Thermal Cycling Under Stress with Subsequent Creep Experiments

Damage accumulation was noticeable considering the increase in austenite strain plot in Figure 4.46. Austenite strain values that were gathered from the first experiment was higher than the austenite strain values that were obtained from the second and third experiments. The decrease in the increasing rate of the austenite strain may be the indication of the strain hardening with the number of cycles.

Austenite strain plots of second and third experiments were linear with the same rate. Damage formation led to an increase in austenite strain starting with the fourth experiment which coincided with the creep strain formation that was presented in Figure 4.44.

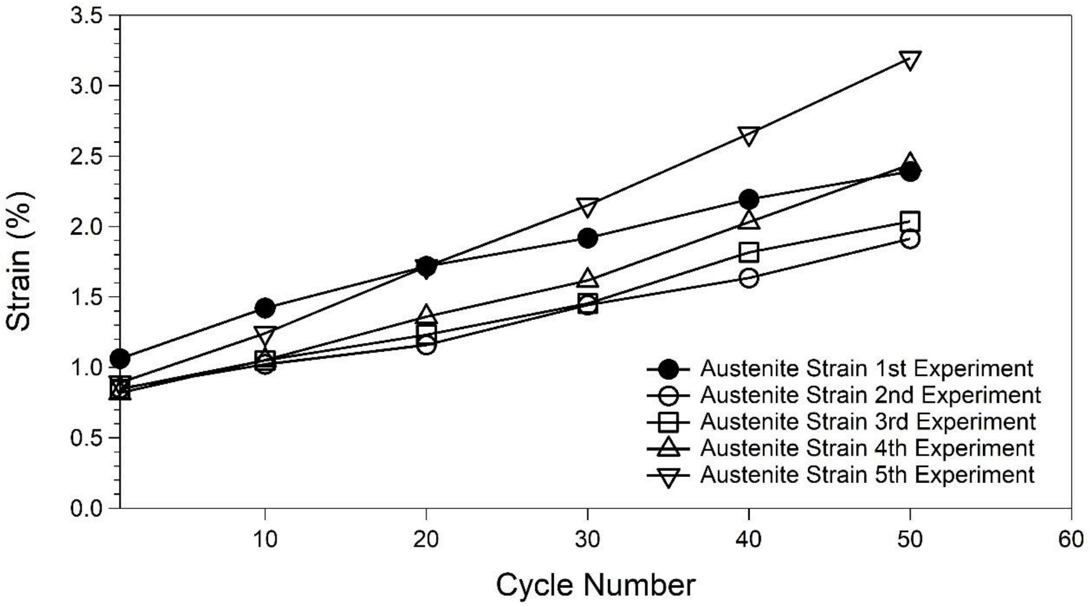

Figure 4.46. Comparison of Austenite Strain values in Thermal Cycling Under Stress with Subsequent Creep Experiments

4.7.3. Micrographs of Damage Between Experiments

Micrographs were taken using optical microscope with a magnification of 50x to reveal the damage formation and evolution during the thermal cycling-subsequent creep experiments. Figure 4.47 was taken after the first experiment which included initial creep experiment, 50 functional fatigue cycles and second creep experiment and shown in Figure 4.42. Cracks were already formed linearly in a parallel formation perpendicular to the loading direction, which was denoted on the figures with a red double sided arrow.

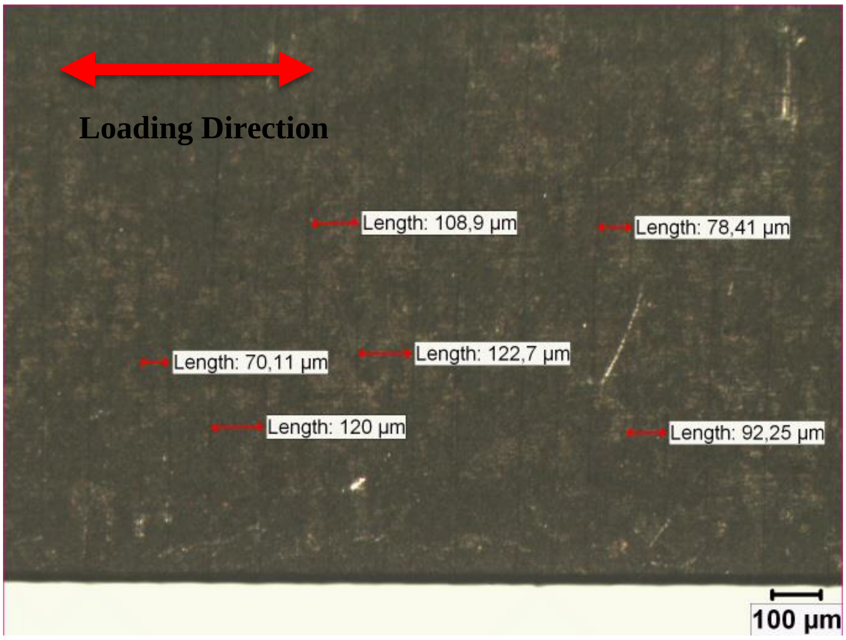

Figure 4.47. Crack formation after the 1st experiment, in the middle section, magnification 50x

Average distance between cracks was measured as 98 micron in the middle section of the tensile specimen from where the temperature data was measured.

After the second experiment (including 50 functional fatigue cycles and the third creep experiment), the surface cracks that were formed earlier became larger, as it can be seen in Figure 4.48 and additionally cracking through the longitudinal direction started between the cracks that were formed perpendicular to the load application direction.

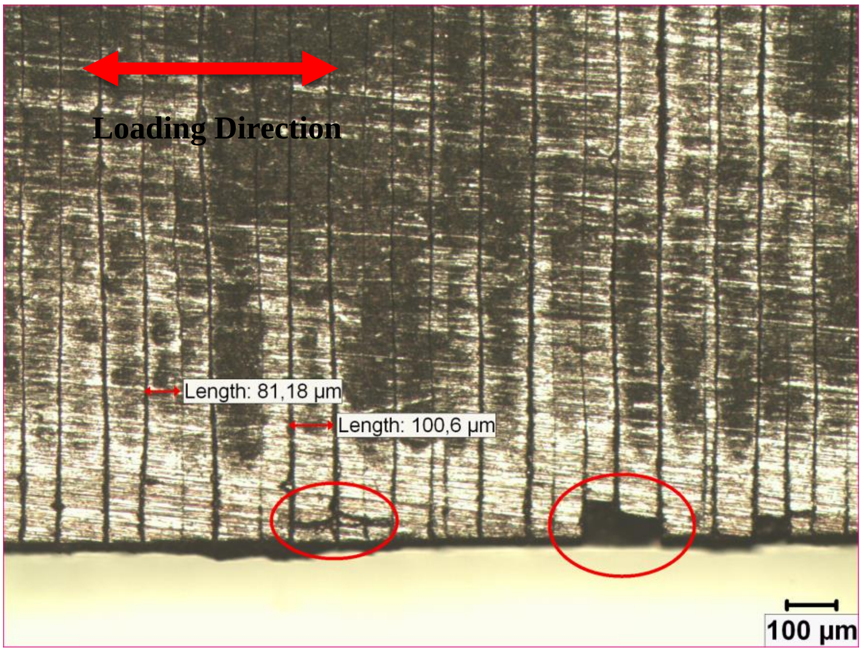

Figure 4.48. Crack formation after the 2nd experiment in the middle section, magnification 50x

Damage micrographs after the third experiment (including another 50 functional fatigue cycles and the fourth creep experiment) was taken from the same location and presented in Figure 4.49. As it can be seen from the Figure, the cracks formed through the longitudinal direction were the same. After the third experiment, horizontal cracks started to form along the loading direction which led to observe more chipping on the sample. It was also noticed that, new crack formations were inhibited by the former crack structure started in Figure 4.47.

.

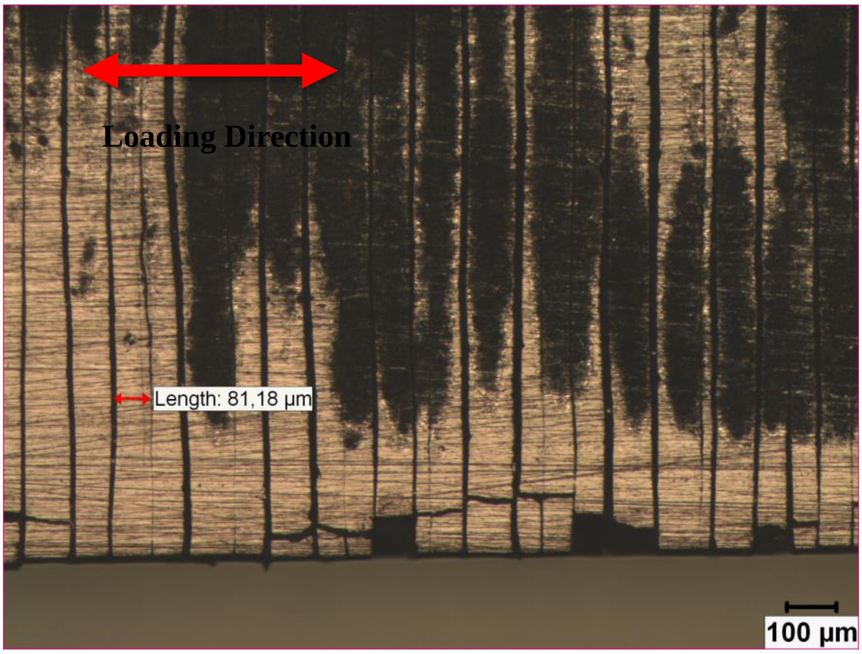

Figure 4.49. Crack formation after the 3rd creep experiment, in the middle section, magnification 50x

It should be noticed from Figure 4.48 that, the distance between the two cracks on the left was exactly the same with the distance that was shown in Figure 4.49. It can be deduced that, cracks on the surface after the first experiment were the cracks due to the surface oxidation and the cracks expanded not sideways but inwards. The surface crack formations after the 4th experiment were shown in Figure 4.50.

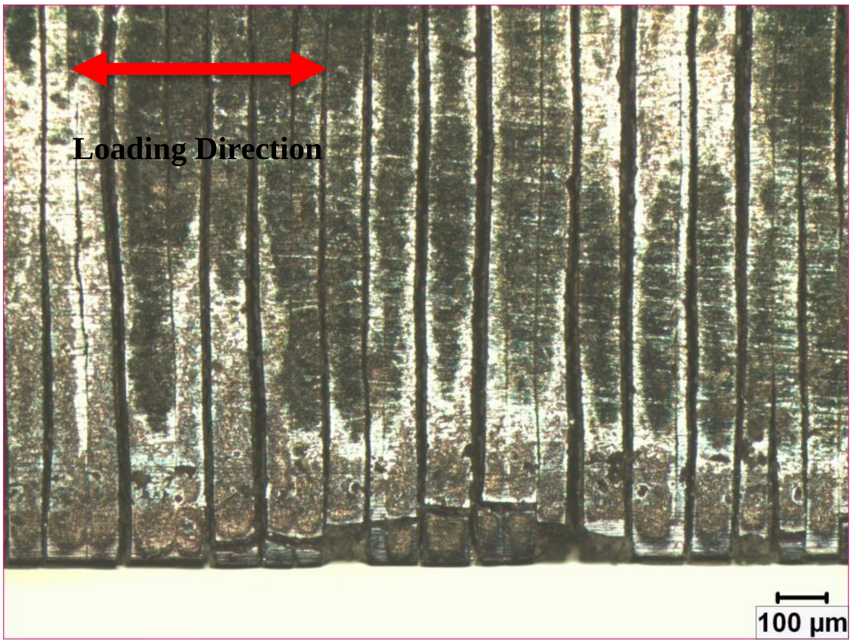

Figure 4.50. Crack formation after the 4th experiment in the middle section, magnification 50x

The crack formation after 100 cycles of a Functional Fatigue experiment that was conducted on An550-3 sample was presented in Figure 4.51 for comparing the differentiation of the damage formation in a functional fatigue experiment and the functional fatigue with subsequent creep experiment.

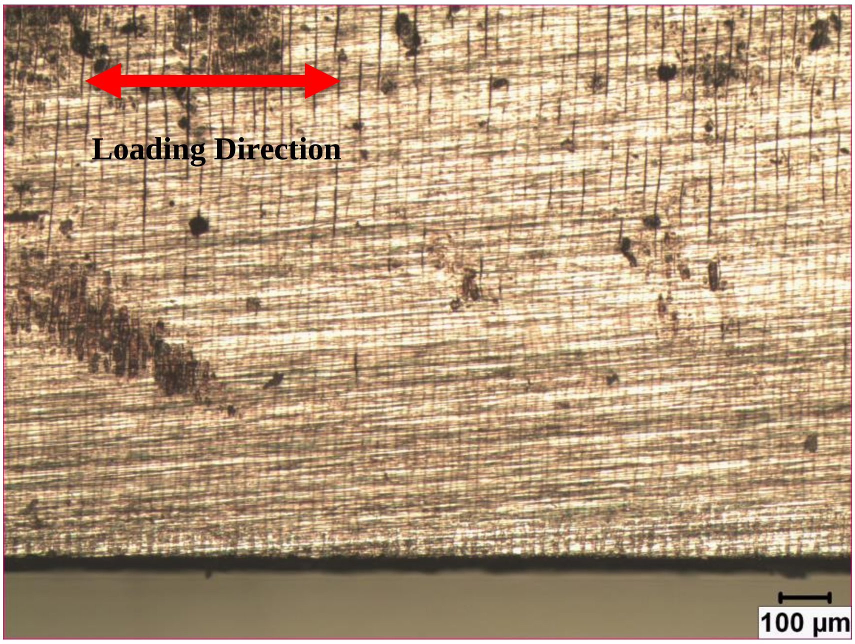

Figure 4.51. Crack formation after 100 cycle of functional fatigue experiment that was conducted on An550-3_S3, magnification 50x

Crack formation after 100 cycles of functional fatigue experiment in Figure 4.51 showed much finer crack formation than that of the crack formations which were formed after 3 hours of creep and 50 cycles of functional fatigue.

After 300 functional fatigue cycles, cracks formed into a wave form due to the accommodation of the shape change with the martensitic transformation. Linearity of the crack formations in Figures 4.47 to 4.50 was not present in Figures 4.51 and 4.52.

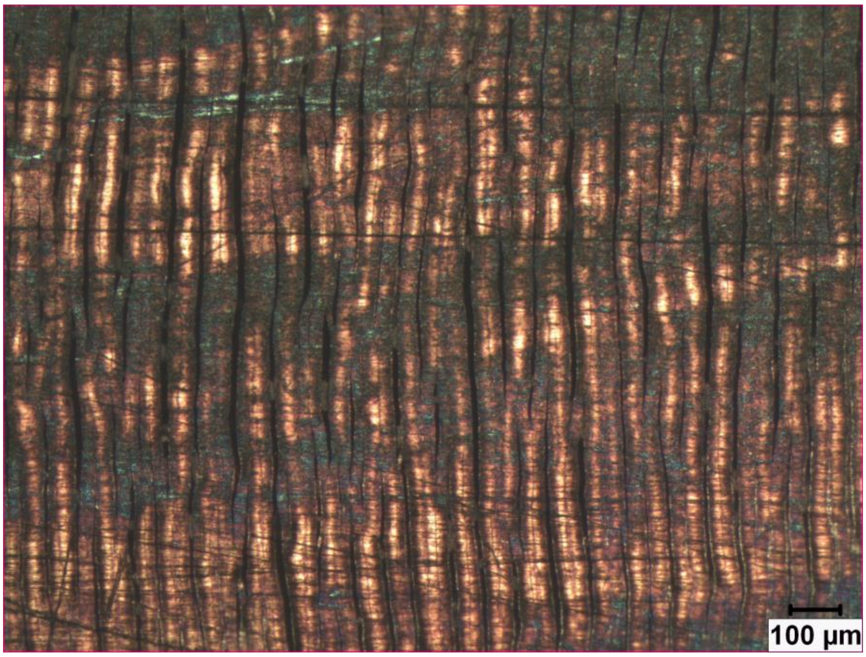

Figure 4.52. Crack formations after 300 cycles of functional fatigue experiment that was conducted on An550-3_S3, magnification 50x

5. CONCLUSION

In this thesis, functional fatigue experiments, creep experiments and functional fatigue experiment with subsequent creep experiments were conducted on annealed and grain growth heat treated 50at%Ni 25at%Ti 25at%Hf HTSMA. Annealing heat treatment was performed at 550°C for 3 hours and grain growth heat treatment was conducted at 800°C for 10 hours. Creep experiments were conducted under constant loads equivalent to 200, 300, 400, 500 MPa stress magnitudes, at 450°C, 500°C, 550°C, 600°C temperatures. Functional fatigue experiments and functional fatigue experiments with subsequent creep experiments were conducted under constant load corresponding to 200 MPa and between 200°C -600°C thermal cycling temperatures. Functional fatigue test setup was used for all experiments and the sample was heated using joule heating method in which direct current passes through the sample and heating occurred due to the internal resistivity of the sample. All experiments were conducted under open air conditions. The following conclusions were drawn from experiments:

1) Stress exponents (Na) for An550-3 samples were calculated using classical Power–Law Creep Equation. Stress exponents were calculated as 3.36 ± 0.32, 2.32 ± 0.31, 3.5 ± 0.16 from the creep experiments which were conducted at 450°C, 550°C and 600°C, respectively. Stress exponent for 550°C experiment was lower than 450°C and 600°C experiments, possibly because annealing temperature was the same with creep experiment temperature. Samples might resume dislocation annihilation in accordance with their initial dislocation density. However, stress exponents that were calculated from creep experiment results indicated viscous glide creep formation. Viscous glide creep is a creep formation that is mostly observed in solid solutions with a limiting factor that inhibits dislocation motion [73]. Stress exponent values of An550-3 samples that were found in this thesis were in accordance with Mukherjee’s, Kato et. al’s and Lexcellent et. al.’s findings in the literature [79,81,82].

2) Activation energy values of An550-10 samples for all stress conditions were calculated around 260 kJ/mol. When activation energy values were compared with literature, it was found that Q values in this thesis were close to the findings of Mukherjee’s constant strain rate experiments and constant load experiment studies of Kato and his coworkers and constant load experiments of Lexcellent and his coworkers [79,81,82]. When vacancy concentration and diffusion studies which were made by Lexcellent’s group were taken

into account; viscous creep behavior of NiTiHf might be a result of the same limiting factor as NiTi where creep deformation is bounded by the diffusion of Titanium [83,106].

3) Stress exponents that were calculated for GG800-10 samples were 3.99, 3.85 and 3.6 for creep experiments that were conducted at 500°C, 550°C and 600°C respectively. Activation energy calculations were provided the value of around 290kJ/mol for loading conditions of 300, 400, 500 MPa. Stress exponents and activation energy results of GG800-10 samples were higher than that of the findings of Mukherjee, Kato et. al, Lexcellent et al. [79,81,82]. However, Eggeler et. al provided stress exponents of 2 and 4.7 and activation energy values were calculated as 334 kJ/mol and 305 kJ/mol for different strain rates which were measured from minimum strain rate and stabilized strain rate after 10% strain formation [84]. Stress exponents and activation energy calculations for GG800-10 samples in this thesis were closer to the findings of Eggeler et. al.

4) Kato et al. and Eggeler et. al. were provided the grain size measurements of the samples before experiments, which were 15 microns and 35 microns, respectively [81,84]. Creep experiment results that were gathered from An550-3 samples were similar to the findings of Kato et al. and creep experiment results that were obtained from GG800-10 samples were similar to the results of Eggeler et. al.. It can be stated that grain size was found to be the main difference between the results in the literature. Comparing creep experiments that were conducted at 550°C and 600°C, it can be concluded that effect of stress on creep strain rate of the samples that have larger grain size was higher. Increase in activation energy proved that, even though creep strains were lower when the grain size was large, effect of temperature on the creep strains increased as well.

5) Functional fatigue experiments of the 50at%Ni 25at%Ti 25at%Hf HTSMA which were conducted under 200 MPa loading conditions, resulted austenite strain values up to 23% for An550-3 sample and 29% total strain for GG800-10 sample. On the other hand, creep experiment that was done on An550-3 sample under 200MPa loading condition at 600°C showed 0.003 true strain in 5 hours, therefore, strain formation was almost negligible when compared with functional fatigue experiment results. Additionally, creep experiment that was conducted on GG800-10 samples at 600°C under 300 MPa loading condition, resulted 0.006 true strain in 5 hours. Therefore, it can be deduced that the functional fatigue austenite strain values, which actually represented the accumulated irrecoverable strains, were because of the plastic deformation due to austenite-martensite phase transformation under stress.

6) Functional fatigue with subsequent creep experiments were conducted in order to reveal the creep behavior in the presence of thermal cycling so that damage formation in both experimental procedures, would be combined and compared with creep experiments. It was provided that creep behavior of the 50at%Ni 25at%Ti 25at%Hf HTSMA was highly affected by the dislocation generation during thermal cycling. Thermal cycles created more dislocation than that of the dislocation formation during creep deformation that lead to observe primary creep formation in the subsequent creep experiments at 600°C. Creep strain rates that were calculated from the results of 2nd, 3rd and 4th creep experiments were higher than the strain rate that was calculated from the 1st creep experiment and the strain rates of 5 hours of creep experiment conducted on An550-3. Crack formation on the other hand was started with the oxidation of the surface. Linear and parallel cracks appeared after the first experiment. New cracks were not formed during the 2nd, 3rd and 4th experiments; instead failure was occurred with the deepening of the existing crack formation.

6. REFERENCES

[1] O. Benafan, R.D. Noebe, T.J. Halsmer, Acta Astronaut. 118 (2016) 137–157.

[2] J. Ma, I. Karaman, R.D. Noebe, Int. Mater. Rev. 55 (2010) 257–315.

[3] O. Karakoc, K.C. Atli, O. Benafan, R.D. Noebe, I. Karaman, Mater. Sci. Eng. A 829 (2022) 142154.

[4] O. Karakoc, K.C. Atli, A. Evirgen, J. Pons, R. Santamarta, O. Benafan, R.D. Noebe, I. Karaman, Mater. Sci. Eng. A 794 (2020) 139857.

[5] A. Evirgen, I. Karaman, R. Santamarta, J. Pons, R.D. Noebe, Acta Mater. 83 (2015) 48–60.

[6] S.M.M. Saghaian, H.E.E. Karaca, M. Souri, A.S.S. Turabi, R.D.D. Noebe, Mater. Des. 101 (2016) 340–345.

[7] H.H. Saygili, H.O. Tugrul, B. Kockar, Shape Mem. Superelasticity 5 (2019) 32–41.

[8] H.O. Tugrul, H.H. Saygili, B. Kockar, J. Intell. Mater. Syst. Struct. 32 (2021) 219–227.

[9] O. Karakoc, C. Hayrettin, M. Bass, S.J. Wang, D. Canadinc, J.H. Mabe, D.C. Lagoudas, I. Karaman, Acta Mater. 138 (2017) 185–197.

[10] O. Karakoc, C. Hayrettin, D. Canadinc, I. Karaman, Acta Mater. 153 (2018) 156–168.

[11] P.K. Kumar, D.C. Lagoudas, Acta Mater. 58 (2010) 1618–1628.

[12] P.K. Kumar, U. Desai, J.A. Monroe, D.C. Lagoudas, I. Karaman, G. Bigelow, R.D. Noebe, Mater. Sci. Eng. A 530 (2011) 117–127.

[13] M.E. Kassner, Fundamentals of Creep in Metals and Alloys, 2nd. Ed., Elsevier, 2008.

[14] G. V. Kurdjumov, Jom 11 (1959) 449–453.

[15] E. Hornbogen, Phys. Status Solidi 172 (1992) 161–172.

[16] H. Funakubo, Shape Memory Alloys, Gordon & Breach Publishing Group, Amsterdam, 1987.

[17] K. Otsuka, C.M. Wayman, eds., Shape Memory Materials, 1998.

[18] B. Kockar, Shape Memory Behavior of Ultrafine Grained NiTi and TiNiPd Shape Memory Alloys, Texas A&M University, 2007.

[19] T.W. Duerig, K.N. Melton, D. Stöckel, C.M. Wayman, Engineering Aspects of Shape Memory Alloys, Butterworth-Heinemann Ltd., 1990.

[20] S. Miyazaki, K. Otsuka, Y. Suzuki, Scr. Metall. 15 (1981) 287–292.

[21] K. Otsuka, K. Shimizu, Int. Met. Rev. 31 (1986) 93–114.

[22] Y. Liu, P.G. McCormick, Mater. Sci. Forum 56–58 (1991) 585–590.

[23] P.Y. Manach, D. Favier, Scr. Metall. Mater. 28 (1993) 1417–1421.

[24] J.L. McNichols, P.C. Brookes, J.S. Cory, J. Appl. Phys. 52 (1981) 7442–7444.

[25] G. Eggeler, E. Hornbogen, A. Yawny, A. Heckmann, M. Wagner, Mater. Sci. Eng. A 378 (2004) 24–33.

[26] H. Sehitoglu, R. Hamilton, H.J. Maier, Y. Chumlyakov, J. Phys. IV 115 (2004) 1–5.

[27] H. Sehitoglu, Y. Wu, L. Patriarca, Scr. Mater. 129 (2017) 11–15.

[28] A.S.K. Mohammed, H. Sehitoglu, Acta Mater. 208 (2021) 116716.

[29] P. Chowdhury, H. Sehitoglu, R. Rateick, Curr. Opin. Solid State Mater. Sci. 20 (2016) 140–150.

[30] S. Alkan, H. Sehitoglu, Int. J. Fatigue 104 (2017) 309–321.

[31] E. Sgambitterra, C. Maletta, F. Furgiuele, H. Sehitoglu, Int. J. Fatigue 112 (2018) 9–20.

[32] D.C. Lagoudas, P.B. Entchev, P. Popov, E. Patoor, L.C. Brinson, X. Gao, Mech. Mater. 38 (2006) 430–462.

[33] Y. Chemisky, A. Duval, E. Patoor, T. Ben Zineb, Mech. Mater. 43 (2011) 361–376.

[34] E. Patoor, D.C. Lagoudas, P.B. Entchev, L.C. Brinson, X. Gao, Mech. Mater. 38 (2006) 391–429.

[35] A. Demblon, O. Karakoc, J. Sam, D. Zhao, K.C. Atli, J.H. Mabe, I. Karaman,

Mater. Sci. Eng. A 838 (2022) 142786.

[36] T.W. Duerig, A.R. Pelton, in: Mater. Prop. Handb. Titan. Alloy., ASM International, 1994, pp. 1035–1048.

[37] D.P. Dautovich, G.R. Purdy, Can. Metall. Quaterly 4 (1965) 129–143.

[38] M. Nishida, C.M. Wayman, T. Honma, Metall. Trans. A 17 (1986) 1505–1515.

[39] A. Ishida, M. Sato, A. Takei, S. Miyazaki, Mater. Trans. JIM 36 (1995) 1349–1355.

[40] S. Miyazaki, K. Otsuka, Metall. Trans. A, Phys. Metall. Mater. Sci. 17 A (1986) 53–63.

[41] P. Franke, D. Neuschütz, in: Thermodyn. Prop. Inorg. Mater., Landolt-Börnstein, 2006, p. 313.

[42] S. Miyazaki, A. Ishida, Mater. Sci. Eng. A 273–275 (1999) 106–133.

[43] P.G. Lindquist, C.M. Wayman, in: T.W. Duerig, K.N. Melton, D. Stöckel, C.M. Wayman (Eds.), Eng. Asp. Shape Mem. Alloy., Butterworth-Heinemann Ltd., 1990, pp. 58–68.

[44] J.W. Moberly, K.N. Melton, in: T.W. Duerig, K.N. Melton, D. Stöckel, C.M. Wayman (Eds.), Eng. Asp. Shape Mem. Alloy., Butterworth-Heinemann Ltd., 1990, pp. 46–58.

[45] H.C. Donkersloot, J.H.N. Van Vucht, J. Less-Common Met. 20 (1970) 83–91.

[46] J. Ma, I. Karaman, R.D. Noebe, Int. Mater. Rev. 55 (2010) 257–315.

[47] D.R. Angst, P.E. Thoma, M.Y. Kao, J. Phys. IV 05 (1995) 747–752.

[48] X.. Meng, W. Cai, Y.. Zheng, Y.. Tong, L.. Zhao, L.. Zhou, Mater. Lett. 55 (2002) 111–115.

[49] X.L. Meng, Y.F. Zheng, W. Cai, L.C. Zhao, J. Alloys Compd. 372 (2004) 180–186.

[50] P.L.L. Potapov, a. V. V. Shelyakov, a. a. A. Gulyaev, E.L. Svistunov, N.M.M. Matveeva, D. Hodgson, E.L. Svistunova, N.M.M. Matveeva, D. Hodgson, Mater. Lett. 32 (1997) 247–250.

[51] F. Dalle, E. Perrin, P. Vermaut, M. Masse, R. Portier, Acta Mater. 50 (2002) 3557–

3565.

[52] G.S. Firstov, J. Van Humbeeck, Y.N. Koval, G.S. Fristov, J. Van Humbeeck, Y.N. Koval, Mater. Sci. Eng. A 378 (2004) 2–10.

[53] B. Kockar, I. Karaman, J.I.I. Kim, Y. Chumlyakov, Scr. Mater. 54 (2006) 2203–2208.

[54] X.L. Meng, W. Cai, Y.F. Zheng, L.C. Zhao, Mater. Sci. Eng. A 438–440 (2006) 666–670.

[55] G.S. Bigelow, A. Garg, S.A. Padula II, D.J. Gaydosh, R.D. Noebe, Scr. Mater. 64 (2011) 725–728.

[56] H.E. Karaca, S.M. Saghaian, B. Basaran, G.S. Bigelow, R.D. Noebe, Y.I. Chumlyakov, Scr. Mater. 65 (2011) 577–580.

[57] R. Santamarta, R. Arróyave, J. Pons, A. Evirgen, I. Karaman, H.E. Karaca, R.D. Noebe, Acta Mater. 61 (2013) 6191–6206.

[58] S.M. Saghaian, H.E. Karaca, H. Tobe, M. Souri, R. Noebe, Y.I. Chumlyakov, Acta Mater. 87 (2015) 128–141.

[59] H.E. Karaca, E. Acar, H. Tobe, S.M. Saghaian, Mater. Sci. Technol. 30 (2014) 1530–1544.

[60] H.E. Karaca, S.M. Saghaian, G. Ded, H. Tobe, B. Basaran, H.J. Maier, R.D. Noebe, Y.I. Chumlyakov, Acta Mater. 61 (2013) 7422–7431.

[61] A.P. Stebner, G.S. Bigelow, J. Yang, D.P. Shukla, S.M. Saghaian, R. Rogers, A. Garg, H.E. Karaca, Y. Chumlyakov, K. Bhattacharya, R.D. Noebe, Acta Mater. 76 (2014) 40–53.

[62] B. Amin-Ahmadi, R.D. Noebe, A.P. Stebner, Scr. Mater. 159 (2018) 85–88.

[63] C. Hayrettin, Actuation Fatigue and Fracture of Shape Memory Alloys, Texas A&M University, 2017.

[64] A. Demblon, J.H. Mabe, I. Karaman, in: SMST2022, ASM International, 2022.

[65] H. Sehitoglu, L. Patriarca, Y. Wu, Curr. Opin. Solid State Mater. Sci. 21 (2017) 113–120.

[66] L. Patriarca, H. Sehitoglu, E.Y. Panchenko, Y.I. Chumlyakov, Acta Mater. 106

(2016) 333–343.

[67] P.S. Chaugule, O. Benafan, J.-B. le Graverend, Acta Mater. 221 (2021) 117381.

[68] H.O. Tugrul, O. Akgul, B. Kockar, Mater. Today Commun. 33 (2022) 104827.

[69] M.E. Kassner, in: Fundam. Creep Met. Alloy., 2nd ed., Elsevier, 2008, pp. 1–6.

[70] F.H. Norton, The Creep of Steel at High Temperatures, McGraw-Hill Book Company, Incorporated, 1929.

[71] M.E. Kassner, in: Fundam. Creep Met. Alloy., 2nd ed., Elsevier, 2008, pp. 11–96.

[72] M.-T. Perez-Parado, Kassner, in: Fundam. Creep Met. Alloy., 2nd ed., Elsevier, 2008, pp. 97–101.

[73] M.E. Kassner, in: Fundam. Creep Met. Alloy., 2nd Ed., Elsevier, 2008, pp. 125–133.

[74] J.-S. Zhang, in: High Temp. Deform. Fract. Mater., Woodhead Publishing, 2010, pp. 28–38.

[75] J.-S. Zhang, in: High Temp. Deform. Fract. Mater., Woodhead Publishing, 2010, pp. 139–158.

[76] M.-T. Perez-Parado, M.E. Kassner, in: Fundam. Creep Met. Alloy., 2nd ed., Elsevier, 2008, pp. 97–101.

[77] A.H. Cottrell, M.A. Jaswon, in: Proc. R. Soc. London. Ser. A. Math. Phys. Sci., 1949, pp. 104–114.

[78] J.L. Snoek, Physica 9 (1942) 862–864.

[79] A.K. Mukherjee, J. Appl. Phys. 39 (1968) 2201–2204.

[80] M. Franz, E. Hornbogen, Mater. Sci. Eng. A 252 (1998) 157–165.

[81] H. Kato, T. Yamamoto, S. Hashimoto, S. Miura, Mater. Trans. JIM 40 (1999) 343–350.

[82] C. Lexcellent, P. Robinet, J. Bernardini, D.L. Beke, P. Olier, Materwiss. Werksttech. 36 (2005) 509–512.

[83] J. Bernardini, C. Lexcellent, L. Daróczi, D.L. Beke, Philos. Mag. 83 (2003) 329–338.

[84] G. Eggeler, J. Khalil-Allafi, K. Neuking, A. Dlouhý, Zeitschrift Fuer Met. Res. Adv. Tech. 93 (2002) 654–660.

[85] S.M. Oppenheimer, A.R. Yung, D.C. Dunand, Scr. Mater. 57 (2007) 377–380.

[86] V. Taillebot, S. Divinsky, C. Lexcellent, J. Bernardini, D.L. Beke, Defect Diffus. Forum 280–281 (2008) 97–104.

[87] S. V. Raj, R.D. Noebe, Mater. Sci. Eng. A 581 (2013) 145–153.

[88] G.W.H. Höhne, W.F. Hemminger, H.-J. Flammersheim, in: Differ. Scanning Calorim. an Introd. Pract., Springer, 2003.

[89] ASTM International, ASTM E8M: Standard Test Methods for Tension Testing of Metallic Materials, 2004.

[90] E. Akin, O. Akgul, H.O. Tugrul, G. Dugan, B. Kockar, Smart Mater. Struct. 30 (2021) 105017.

[91] K.M. Kim, J.T. Yeom, H.S. Lee, S.Y. Yoon, J.H. Kim, Thermochim. Acta 583 (2014) 1–7.

[92] H. Dabbaghi, K. Safaei, M. Nematollahi, P. Bayati, M. Elahinia, Materials (Basel). 13 (2020).

[93] O. Benafan, A. Garg, R.D. Noebe, G.S. Bigelow, S.A. Padula, D.J. Gaydosh, N. Schell, J.H. Mabe, R. Vaidyanathan, Intermetallics 50 (2014) 94–107.

[94] M. Susa, R.K. Endo, in: H. Fukuyama, Y. Waseda (Eds.), High Temp. Meas. Mater., Springer Berlin Heidelberg, 2009, pp. 111–297.

[95] H.H. Saygili, The Development of a Fatigue Test Machine To Investigate the Functional Fatigue Life of High Temperature Shape Memory Alloys and the Determination of the Functional Fatigue Life of These Alloys, Hacettepe University Graduate School of Science and Engineering, 2018.

[96] ASTM International, ASTM E3097-17: Standard Test Method for Mechanical Uniaxial Constant Force Thermal Cycling of Shape Memory Alloys, 2018.

[97] M. Moshref-Javadi, M. Belbasi, S.H. Seyedein, M.T. Salehi, J. Mater. Sci. Technol. 30 (2014) 280–284.

[98] B. Kockar, I. Karaman, a. Kulkarni, Y. Chumlyakov, I. V. Kireeva, J. Nucl. Mater. 361 (2007) 298–305.

[99] D.A. Miller, D.C. Lagoudas, Mater. Sci. Eng. A 308 (2001) 161–175.

[100] B. Kockar, I. Karaman, J.I. Kim, Y.I. Chumlyakov, J. Sharp, C.J. Yu, Acta Mater. 56 (2008) 3630–3646.

[101] J. Humphreys, G.S. Rohrer, A. Rollett, in: Recryst. Relat. Annealing Phenom., Elsevier, 2017, pp. 13–79.

[102] M. Ekiciler, B. Kockar, Smart Mater. Struct. 31 (2022) 095002.

[103] Y.Q. Wang, Y.F. Zheng, W. Cai, L.C. Zhao, Acta Metall. 40 (1999) 1327–1331.

[104] B.C. De Cooman, Curr. Opin. Solid State Mater. Sci. 8 (2004) 285–303.

[105] A.D. Freed, S. V. Raj, K.P. Walker, J. Eng. Mater. Technol. Trans. ASME 114 (1992) 46–50.

[106] G. Erdélyi, Z. Erdélyi, D.L. Beke, J. Bernardini, C. Lexcellent, Phys. Rev. B - Condens. Matter Mater. Phys. 62 (2000) 11284–11287.

APPENDIX

Appendix 1 – Articles Derived From Thesis

H.O. Tugrul, O. Akgul, B. Kockar, Mater. Today Commun. 33 (2022) 104827.

Appendix 2 – Conference Proceedings Derived From Thesis

H. Onat Tugrul, Benat Koçkar, Creep Properties of Ni50Ti25Hf25 High Temperature Shape Memory Alloys, 12th European Symposium on Martensitic Transformations, 2022, Ankara, Turkey.

Appendix 3 – Thesis Originality Report